

## Hydrodynamics of electromagnetically controlled jet oscillations

Righolt, Bernhard

**DOI**

[10.4233/uuid:3c676ede-2ddb-41f7-ad29-eec9eab29526](https://doi.org/10.4233/uuid:3c676ede-2ddb-41f7-ad29-eec9eab29526)

**Publication date**

2016

**Document Version**

Final published version

**Citation (APA)**

Righolt, B. (2016). *Hydrodynamics of electromagnetically controlled jet oscillations*. [Dissertation (TU Delft), Delft University of Technology]. <https://doi.org/10.4233/uuid:3c676ede-2ddb-41f7-ad29-eec9eab29526>

**Important note**

To cite this publication, please use the final published version (if applicable). Please check the document version above.

**Copyright**

Other than for strictly personal use, it is not permitted to download, forward or distribute the text or part of it, without the consent of the author(s) and/or copyright holder(s), unless the work is under an open content license such as Creative Commons.

**Takedown policy**

Please contact us and provide details if you believe this document breaches copyrights. We will remove access to the work immediately and investigate your claim.

# **Hydrodynamics of electromagnetically controlled jet oscillations**

PROEFSCHRIFT

ter verkrijging van de graad van doctor  
aan de Technische Universiteit Delft,  
op gezag van de Rector Magnificus prof. ir. K.C.A.M. Luyben,  
voorzitter van het College van Promoties,  
in het openbaar te verdedigen op donderdag 7 juli 2016 om 10:00 uur  
door

**Bernhard Willem RIGHOLT**

natuurkundig ingenieur  
geboren te Leidschendam

Dit proefschrift is goedgekeurd door de  
promotor: Prof. dr. ir. C.R. Kleijn  
copromotor: Dr. S. Kenjereš Dipl.-Ing.

Samenstelling van de promotiecommissie:

Rector Magnificus	voorzitter
Prof. dr. ir. C.R. Kleijn	Technische Universiteit Delft, promotor
Dr. S. Kenjereš Dipl.-Ing.	Technische Universiteit Delft, copromotor

Onafhankelijke leden:

Prof. dr. ir. C. Vuik	Technische Universiteit Delft
Prof. dr. D. J. E. M. Roekaerts	Technische Universiteit Delft
Prof. dr. ir. B. J. Geurts	Universiteit Twente
Prof. dr. K. Pericleous	University of Greenwich
Ir. D. van der Plas	Tata Steel Europe
Prof. dr. R.F. Mudde	Technische Universiteit Delft, reservelid

This work was supported by the Dutch Technology Foundation STW, Tata Steel and ABB.

Copyright © 2016 by B. W. Righolt

All rights reserved. No part of the material protected by this copyright notice may be reproduced or utilized in any form or by any means, electronic or mechanical, including photocopying, recording, or by any information storage and retrieval system, without written permission from the author.

ISBN: 978-94-6186-664-6





# Contents

<b>Summary</b>	<b>xi</b>
<b>Samenvatting</b>	<b>xv</b>
<b>1 Introduction</b>	<b>1</b>
1.1 Background . . . . .	1
1.2 Physical phenomena in steel casting . . . . .	2
1.3 Research objectives . . . . .	3
1.3.1 Mechanism for self-sustained flow oscillations in a thin cavity . . . . .	4
1.3.2 Prediction of large scale jet oscillations in a thin cavity . . . . .	4
1.3.3 Electromagnetic flow control of jet oscillations in a thin cavity . . . . .	4
1.3.4 Magnetohydrodynamic free surface flow in a shallow cavity . . . . .	5
1.4 Funding of this PhD thesis . . . . .	5
1.5 Outline . . . . .	5
Bibliography . . . . .	7
<b>2 Methods</b>	<b>9</b>
2.1 Introduction . . . . .	9
2.2 One-way coupled magnetohydrodynamics . . . . .	9
2.3 One-way coupled magnetohydrodynamics solver . . . . .	10
2.4 Volume of fluid and magnetohydrodynamics . . . . .	11
2.5 MMIT Magnetohydrodynamics . . . . .	12

---

2.6	Dynamic Smagorinsky model . . . . .	14
2.7	Spalding's Law . . . . .	16
	Bibliography . . . . .	19
<b>3</b>	<b>Analytical solutions of one-way coupled magnetohydrodynamic free surface flow</b>	<b>21</b>
3.1	Introduction . . . . .	22
3.2	Analytical derivation . . . . .	23
3.2.1	Conservation equations . . . . .	24
3.2.2	Boundary conditions . . . . .	24
3.2.3	Lubrication theory . . . . .	27
3.2.4	Core flow . . . . .	28
3.2.5	End wall flow . . . . .	31
3.2.6	Analytic solution for the end wall flow . . . . .	33
3.2.7	Increased magnetic interaction . . . . .	39
3.3	Numerical modeling . . . . .	40
3.3.1	Moving mesh interface tracking method . . . . .	40
3.3.2	Volume of fluid method . . . . .	41
3.4	Numerical results . . . . .	43
3.4.1	Base case . . . . .	43
3.4.2	Three-dimensionality of the flow . . . . .	45
3.4.3	Increased deformation . . . . .	45
3.4.4	Error . . . . .	49
3.5	Conclusions . . . . .	49
	Bibliography . . . . .	53
<b>4</b>	<b>Dynamics of a single, oscillating turbulent jet in a confined cavity</b>	<b>55</b>
4.1	Introduction . . . . .	55
4.2	Methods . . . . .	56
4.2.1	Description of setup . . . . .	56
4.2.2	Numerical fluid flow models . . . . .	58

---

4.3	Validation of the numerical method . . . . .	59
4.4	Model for self-sustained oscillations of a jet in a confined cavity . . . . .	62
4.4.1	Physical mechanisms . . . . .	62
4.4.2	Model description . . . . .	65
4.5	Determination of model parameters and its implications . . . . .	66
4.5.1	Reduced parameters . . . . .	67
4.5.2	Parameter estimation . . . . .	69
4.5.3	Model application . . . . .	70
4.6	Conclusion . . . . .	73
	Bibliography . . . . .	76
4.A	A posteriori determination of the model parameters . . . . .	76
4.A.1	Phase average . . . . .	76
4.A.2	Cost function . . . . .	77
4.A.3	Error estimation . . . . .	77
4.B	Derivation of the maximum jet angle . . . . .	77
<b>5</b>	<b>Electromagnetic control of an oscillating turbulent jet in a confined cavity</b>	<b>81</b>
5.1	Introduction . . . . .	82
5.2	Problem definition and methods . . . . .	83
5.2.1	Description of the set-up . . . . .	83
5.2.2	Dimensionless numbers . . . . .	83
5.2.3	Magnetic field calculation . . . . .	84
5.2.4	Flow simulations . . . . .	85
5.2.5	Validation . . . . .	87
5.3	Influence of electromagnetic forcing on self-sustained oscillations . . . . .	87
5.3.1	Mean velocity . . . . .	87
5.3.2	Oscillation frequency . . . . .	92
5.3.3	Pressure oscillations . . . . .	93
5.3.4	Jet angle amplitude . . . . .	93
5.3.5	Flow regimes . . . . .	95



5.4	Zero-dimensional model of the jet oscillation . . . . .	95
5.4.1	Unforced flow ( $N = 0$ ) . . . . .	95
5.4.2	Electromagnetically forced flow ( $N \neq 0$ ) . . . . .	96
5.5	Determination of the model parameters and its implications . . . . .	97
5.5.1	Non-dimensional model . . . . .	97
5.5.2	Parameter fitting . . . . .	98
5.5.3	Parameter estimation . . . . .	99
5.5.4	Model application . . . . .	100
5.6	Conclusion . . . . .	101
	Bibliography . . . . .	106
5.A	Electromagnetic field . . . . .	106
<b>6</b>	<b>Dynamics of a bifurcated jet in a confined cavity with a free surface</b>	<b>109</b>
6.1	Introduction . . . . .	109
6.2	Numerical method and validation . . . . .	110
6.2.1	Description of the set-up . . . . .	110
6.3	Oscillation mechanism free surface . . . . .	113
6.3.1	Jet splitting . . . . .	113
6.3.2	Pressure deficit growth . . . . .	114
6.3.3	Maximum pressure deficit and fluid overshoot . . . . .	117
6.3.4	Pressure deficit decrease . . . . .	119
6.4	Influence of a wall . . . . .	119
6.5	Conclusion . . . . .	121
	Bibliography . . . . .	122
<b>7</b>	<b>Conclusions and outlook</b>	<b>125</b>
7.1	General conclusions . . . . .	125
7.1.1	Benchmark MHD free surface flow problem . . . . .	125
7.1.2	Mechanism for self-sustained jet oscillations . . . . .	125
7.1.3	Model description of self-sustained jet oscillations . . . . .	126

---

7.1.4	Electromagnetic forcing of single jet oscillations . . . . .	126
7.2	Research opportunities . . . . .	127
7.2.1	Zero-dimensional models . . . . .	127
7.2.2	Damping of oscillations . . . . .	127
7.2.3	Towards improved continuous steel casting . . . . .	128
	Bibliography . . . . .	130
	<b>List of Publications</b>	<b>133</b>
	<b>Acknowledgements</b>	<b>135</b>
	<b>Curriculum Vitae</b>	<b>137</b>



# Summary

Continuous steel casting is an industrial process where turbulent liquid steel jets enter a thin mould through a submerged nozzle. In the mould the steel is cooled, such that it solidifies. The submerged jets can show self-sustained oscillatory behaviour, which has an impact on the distribution of heat, the solidification of the steel and therefore the overall quality of the steel. Oscillations of the liquid steel jets also influence the free surface in the mould, leading to the unwanted inclusion of slag particles and again degraded quality of the steel. By the application of an electromagnetic brake, the liquid steel flow can be controlled, jet oscillations can be suppressed, and hence the quality of the steel product improved.

In this thesis we use numerical and analytical methods to study the flow dynamics of self-sustained single and bifurcated submerged liquid jet oscillations in a liquid filled thin cavity with and without a free surface. Furthermore we study the influence of electromagnetic forces on single jets and free surface flows.

Firstly, we developed three-dimensional, time dependent flow simulation methods that combine large eddy turbulence modelling with electromagnetic body forces and two different approaches to free surface modelling, viz. Volume of Fluid (VOF) and Moving Mesh Interface Tracking (MMIT). Various aspects of these simulation codes were validated against experimental flow and free surface data by Kalter (2015), obtained in a parallel PhD project through Particle Image Velocimetry in a water model.

Secondly, to further validate the numerical simulation codes, we derived an analytical solution for a two-dimensional benchmark problem, consisting of a shallow cavity with a free surface, where the flow is driven by an electromagnetic force and the free surface deformation is restored by both gravity and surface tension. Under specific constraints for the Reynolds number, Hartmann number, capillary number, Bond number and cavity aspect ratio, we analytically solve the details of the flow dynamics and the free surface deformation using lubrication theory and matching of asymptotic expansions. With these solutions we demonstrate the validity of both numerical models. Consecutively we use the numerical solutions to evaluate the validity of the analytical solution when the constraints for which it was derived are relaxed. In future research, the presented analytical solution and the information about the range of the dimensionless numbers for which it is valid, can serve as a benchmark prob-

lem for newly developed numerical simulation codes for free surface magnetohydrodynamic flows.

Thirdly, using the results of our three-dimensional computational simulations, we developed a zero-dimensional, delay differential equation type model which quantitatively describes the self-sustained oscillation of a jet in a thin cavity. Three terms in the zero-dimensional model equation represent the three physical mechanisms that contribute to the self-sustained oscillation, viz. (i) pressure driven oscillation growth, (ii) amplitude limitation by geometry and (iii) delayed destruction of the recirculation zone. The zero-dimensional model equation contains four model parameters, and we show that these parameters can be a priori calculated from the Reynolds number ( $Re$ ), the cavity width to nozzle diameter ratio ( $W/d$ ), the inlet velocity and the nozzle diameter. By comparing predictions from the zero-dimensional model to data from our three-dimensional computational simulations as well as experimental data by Kalter (2015), we show that the zero-dimensional model with a priori calculated model parameters correctly predicts the frequency and waveform of the jet oscillation for a wide range of Reynolds numbers and cavity width to nozzle diameter aspect ratios. In agreement with our three-dimensional simulations, the zero-dimensional model predicts that for given aspect ratio there is a critical Reynolds number below which the self-sustained oscillations vanish.

Fourthly, we extended our zero-dimensional model to include the effect of a body force on the self-sustained oscillations. In particular, the body force studied is an electromagnetic force, originating from an externally applied magnetic field and an imposed electrical current across the domain. Again, results from the zero-dimensional model are being compared to experimental data by Kalter (2015) and data from our own three-dimensional computational simulations. We show that the three physical mechanisms that contribute to the self-sustained oscillation, and thus the form of the model equation, remain the same as in the absence of electromagnetic body forces. The value of the four model parameters, however, now also depends on an additional dimensionless number, viz. the (signed) Stuart number, representing the ratio of electromagnetic body forces and inertial forces. We present closed relations to a priori predict the value of the four model parameters as a function of the Reynolds number, the Stuart number, the cavity width to nozzle diameter aspect ratio, the inlet velocity, and the nozzle diameter. From both zero-dimensional model predictions and three-dimensional computational simulations, we demonstrate that three flow regimes can be distinguished, separated by the positive critical Stuart number and the negative critical Stuart number. In between these two values, inertial forces are dominant. Outside this range, electromagnetic forces are dominant, and either enhance or suppress oscillations.

Finally, using detailed spatio-temporally resolved flow and pressure data from our three-dimensional model simulations, we demonstrate the validity of the pressure-based mechanism for self-sustained jet oscillations in a thin cavity, as suggested earlier in literature (Honeyands, Kalter). For both single and bifurcated jet arrangements, the jets deflect towards the jet-induced bounded recirculation zones. The pressure deficit in the recirculation zone deflects the jet further, leading to an increasing pressure deficit. This continues until the recirculation zone cannot grow any further due to geometrical restrictions and the jet reaches

an extreme position. The liquid flow then escapes the recirculation zone, feeding a different recirculation zone. For the single jet configuration this leads to the jet being deflected to the opposite side. For the bifurcated jet configuration this leads to the opposite jet being deflected.

We conclude this thesis with the main findings, and we describe how these main findings can lead to the further understanding of self-sustained oscillations in a continuous steel casting mould.



# Samenvatting

Tijdens het continu gieten van staal wordt vloeibaar staal via een dompelpijp in een gietvorm gegoten. De gietvorm wordt actief gekoeld, waardoor het staal langzaam stolt. De turbulente jets die uit de dompelpijp stromen, kunnen zichzelf in stand houdend, oscillerend gedrag vertonen. Dit gedrag heeft invloed op zowel de warmteverspreiding in de gietvorm als op het staaloppervlak aan de bovenzijde van de gietvorm. Beide kunnen een negatief effect hebben op de kwaliteit van het geproduceerde staal. De oscillaties van de jets kunnen beïnvloed worden met behulp van een zogenaamde elektromagnetische rem, waardoor de kwaliteit van het staal verbetert.

In dit proefschrift gebruiken we numerieke simulaties en wiskundige modellen om de vloeistofdynamische mechanismen achter de oscillaties van jets in gietvormen te ontrafelen. We bestuderen zowel rechte als gesplitste dompelpijpen in een gietvorm met of zonder een vrij oppervlak. Daarnaast bestuderen wij de invloed van elektromagnetische krachten hierop.

Ten eerste hebben wij simulatieprogramma's ontwikkeld waarmee de driedimensionale, tijdsafhankelijke, turbulente stroming in de gietvorm, onder invloed van elektromagnetische krachten, gesimuleerd kan worden. We hebben daarin twee methodes geïmplementeerd voor het numeriek simuleren van het vrije oppervlak: de Volume of Fluid (VOF) methode en de Moving Mesh Interface Tracking (MMIT) methode. De simulatieprogramma's zijn gevalideerd aan de hand van experimentele data over de vloeistofstroming en het gedrag van het vrije oppervlak, zoals verkregen in een parallel promotieproject van Kalter (2015) met behulp van Particiale Image Velocimetry.

Ten tweede hebben wij om onze computersimulatieprogramma's verder te kunnen valideren een relevant tweedimensionaal magneto-hydrodynamisch stromingsprobleem gedefinieerd dat wij analytisch konden oplossen zodat we de oplossingen konden vergelijken met de resultaten van de numerieke simulaties. Dit validatieprobleem bestaat uit de stroming in een ondiepe laag vloeistof met een vrij oppervlak, welke vervormt ten gevolge van een opgelegde elektromagnetische kracht, de zwaartekracht en de oppervlaktespanning. Met behulp van lubrication theory en matching of asymptotic expansions hebben wij de stroming in de vloeistoflaag en de vervorming van het vrije oppervlak mathematisch bepaald voor kleine waarden van het Reynolds getal, het Hartmann getal, het capillair getal, het Bond getal en de breedte-diepte



verhouding van de vloeistoflaag. Met deze mathematische oplossing hebben we de geldigheid van de numerieke simulatiemethodes aangetoond. Omgekeerd hebben we daarna de numerieke simulaties gebruikt om te onderzoeken in hoeverre de analytische oplossing ook voor grotere waarden van de genoemde kentallen geldig blijft. Met deze kennis kan onze mathematische oplossing in toekomstig onderzoek gebruikt worden voor de validatie van nieuwe numerieke simulatiecodes magnetohydrodynamische vrije oppervlakte stromingen.

Ten derde hebben wij een nuldimensionaal model ontwikkeld dat zowel het optreden als de frequenties en de golfvorm van de zichzelf in stand houdende jetoscillaties in een dunne gietvorm kwantitatief voorspelt. Dit nuldimensionale model is geïnspireerd door de mechanismen die we hebben waargenomen in onze driedimensionale numerieke simulaties en is mathematisch gebaseerd op een tijdsafhankelijke differentiaalvergelijking met een vertragingsterm. De modelvergelijking bevat drie termen, die de drie stadia van de oscillatie beschrijven, namelijk (i) groei van de oscillatie ten gevolge van drukminima in de geïnduceerde stromingsrecirculaties, (ii) demping en beperkte amplitude door de geometrische begrenzing en (iii) vertraagde vernietiging van de recirculatiezone. Het model bevat vier modelconstanten. Wij tonen aan dat deze vier constanten a priori kwantitatief kunnen worden bepaald uit het Reynolds getal, de breedte van de gietvorm, de diameter van de gietpijp en de instroomsnelheid van de jet. Op basis van vergelijkingen met experimentele data van Kalter (2015) en resultaten van onze drie-dimensionale numerieke simulaties tonen wij aan dat het ontwikkelde nuldimensionale model de frequentie en golfvorm van de jetoscillatie correct voorspelt. Bovendien voorspelt het nuldimensionale model correct dat er voor elke verhouding tussen de breedte van de gietvorm en de diameter van de gietpijp een kritisch Reynolds getal bestaat, waaronder de zichzelf in stand houdende oscillaties verdwijnen.

Ten vierde hebben wij het nuldimensionale model voor de jetoscillaties in een dunne gietvorm uitgebreid naar de situatie waarin een elektromagnetische volumekracht, opgewekt door een extern opgelegd magneetveld en een extern opgelegde elektrische stroom, werkzaam is op de vloeistof. Weer vergelijken we de resultaten van het nuldimensionale model met experimentele resultaten van Kalter (2015) en met de resultaten van onze driedimensionale simulaties. We laten zien dat ook in aanwezigheid van elektromagnetische krachten dezelfde drie fysische mechanismen ten grondslag liggen aan de oscillaties. Echter, de vier model parameters zijn nu afhankelijk van een extra dimensieloos kental, namelijk het Stuart getal. Het Stuart getal is de verhouding tussen de elektromagnetische en de traagheidskrachten. Uit zowel de resultaten van het nuldimensionale model, als de driedimensionale simulaties blijkt dat er drie regimes in het stromingsgedrag optreden, gescheiden door een positief en een negatief kritisch Stuart getal. Tussen beide waarden zijn de traagheidskrachten dominant. Voor grotere absolute waarden van het Stuart getal hebben de elektromagnetische krachten de overhand, waarbij de oscillaties respectievelijk onderdrukt of versterkt worden.

Ten slotte hebben wij de juistheid van het op druk gebaseerde mechanisme voor de zichzelf in stand houdende jet oscillatie in een dunne gietvorm, zoals eerder voorgesteld in de literatuur (Honeyands, Kalter), aangetoond met behulp van de stroomsnelheid en druk uit onze tijdsafhankelijke, driedimensionale simulaties. Zowel enkele als gesplitste jets buigen af in de richting van de door de jet veroorzaakte recirculatiezone. Ten gevolge van het lo-

kale drukminimum in het midden van deze recirculatie buigt de jet steeds verder af, leidend tot een versterkt drukminimum. Dit zet zich voort totdat de recirculatiezone niet verder kan groeien ten gevolge van de geometrische begrenzing, waardoor de jet een extremum bereikt. De vloeistof stroomt dan weg uit de recirculatiezone, waarop een andere recirculatie in de tegenoverliggende zijde van de holte wordt gevoed. Voor een enkele jet zal deze jet afbuigen naar de andere zijde van de gietvorm, en voor een gesplitste jet zal de jet aan de andere zijde afbuigen.

We sluiten dit proefschrift af met een beschouwing over hoe de belangrijkste bevindingen gebruikt kunnen worden om te komen tot een beter begrip en een betere beheersing van vloeistofoscillaties in gietvormen bij continu staalgieten.



# 1. Introduction

## 1.1 Background

In the current century, the world steel production was nearly doubled from  $0.85 \times 10^9$  metric tons in 2001 to  $1.5 \times 10^9$  metric tons in 2012. While the Dutch steel production, solely due to the Tata Steel (formerly Corus) plant in IJmuiden, has increased by 14% in this period, the production rate in China exploded with a 370% growth.<sup>21,22</sup> The European steel market is still recovering from the economic crisis in 2008 and not yet back to the production rate of 2007.

The casting of metal in the beginning of the twentieth century was a batch process, casting the liquid metals in blocks. Already in 1887, the first idea for a continuous caster was patented.<sup>1</sup> The basic concept never changed and is schematically depicted in Figure 1.1. The vertical, water cooled mould is filled with metal and the solidified metal is extracted and cut at the bottom. By the middle of the twentieth century this method was used and further developed, mostly for copper and aluminium casting.

Steel casting was more difficult since the melting temperature is relatively high ( $\sim 1500^\circ C$ ) and the solidification is slow, because of the relatively low thermal conductivity. Innovations, such as<sup>1</sup>

- the oscillating mould (1949) with negative strip time (1954),
- the bending of the steel strip with a liquid core into a horizontal position (1963),
- the submerged pipe to prevent nitrogen pick-up and re-oxidation (1965),
- the tundish and rotating tower (1968) (solving the problem of the liquid steel arriving at the caster in batches) and
- the electromagnetic brake (EMBr) (Kawasaki in the early 80s), to reduce oscillations and damp turbulence

were techniques that helped to improve the efficiency and quality of the produced steel. An EMBr helps increasing the production rate and quality of steel.

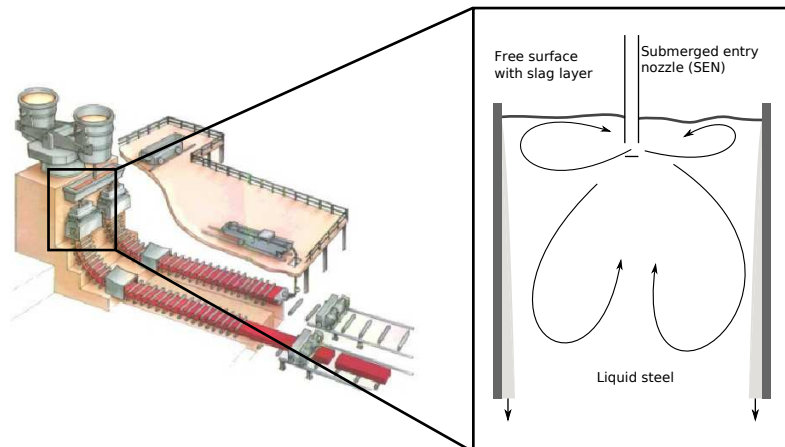


**Figure 1.1** Schematic representation of the continuous casting process (left<sup>19</sup>), with the complete system from ladle to solid strip. The liquid steel arrives at the system in batches, flows into the tundish to make it a batch process, after which it is poured into the mould. (right, zoom-in) Mould of the continuous casting process. The liquid steel enters the mould via the submerged entry nozzle (SEN).

## 1.2 Physical phenomena in steel casting

Continuous steel casting is a complex industrial process. Many different physical phenomena are taking place in the steel casting process.<sup>1</sup>

1. Fluid mechanics is an important phenomenon in the steel casting process. The flow is highly turbulent in the top of the caster near the jets emerging from the submerged entry nozzle (SEN), and the fluid might relaminarize further down the mould. The flow may induce large scale oscillations in the mould.<sup>5,7</sup>
2. A slag layer is present on top of the liquid. This slag layer prevents oxidation of the liquid steel when in direct contact with air. Due to large velocities in the top of the mould, the steel-slag interface can move violently, possibly leading to the inclusion of the slag and other pollutants into the steel.<sup>4</sup> Gravitational forces, and to a lesser degree surface tension forces, play a key role in the behavior of this interface.
3. An electromagnetic break (EMBr) is an external magnetic field that is often applied to the steel flow.<sup>3</sup> The EMBr is installed in order to damp the flow and free surface oscillations. The magnetic field induces an electrical current and subsequently a Lorentz

force, which may not only affect the large scale motions and free surface oscillations, but also the turbulence and its isotropy.<sup>10</sup>

4. The solidification of the liquid steel starts at the boundaries to form a solid shell. This solidified shell is lubricated by the slag layer to protect it from contact with the copper mould. Flow oscillations and inclusions in the liquid steel largely determine the quality of the solid steel product.<sup>1</sup>
5. The heat transfer from the liquid steel to the surroundings plays an important role in the solidification process. The rate and uniformity of the heat transfer determine the optimal thickness and uniformity of the solidified shell respectively, and thus ensure a high quality of the solid steel.<sup>1</sup>
6. The thermomechanical behavior of the solidifying shell becomes relevant further down the mould. As the steel cools down, it shrinks. This may create an isolating air gap between the solid steel and the mould, highly reducing the heat transfer from the steel to the surroundings.
7. The tapering of the mould, in order to compensate for thermomechanical shrinkage.<sup>1</sup>
8. The copper mould oscillates significantly in order to reduce the risk of the solidifying shell to stick to the mould, despite the lubricating behaviour of the slag layer in between steel and mould.<sup>1</sup>
9. The liquid core reduction, where the solidified shells on opposite sides of the caster are pressed together, reduces the size of the liquid core and speeds up the solidification.<sup>1</sup>
10. Argon is injected into the mould, to prevent clogging of the small nozzle and to blow out any pollutants residing in the caster.<sup>20</sup>

### 1.3 Research objectives

In this thesis we address, from a fundamental point of view, the first three of the physical phenomena mentioned in section 1.2, namely (i) fluid flow and turbulence, (ii) the free surface movement, and (iii) the influence of electromagnetic forcing on both. We will not address the remainder of the aforementioned phenomena that play a role in practical continuous steel casting.

In this thesis we use analytical methods and two- and three-dimensional Computational Fluid Dynamics (CFD) simulations. Complementary, an experimental study is carried out.<sup>6</sup> By answering the research questions detailed in this section, we will unravel fundamental physical aspects of the flow oscillations, free surface behavior and electromagnetic control that are difficult to assess experimentally. Furthermore, we will work towards the development of an Large Eddy Simulation (LES) based, Volume Of Fluid (VOF) free surface numerical simulation code for magnetohydrodynamic (MHD) flows in the OpenFOAM framework, validated

against water model experiments and applicable to the optimization of MHD flows in steel casting.

### 1.3.1 Mechanism for self-sustained flow oscillations in a thin cavity

In thin slab continuous steel casting, the liquid steel is fed into a thin mould through a so-called bifurcated (two-port) nozzle, as illustrated in Figure 1.1. The two jets may induce large scale flow oscillations. It is known,<sup>7</sup> that under certain conditions, the oscillations of both jets in a bifurcated configuration align in anti-phase, in other words, both oscillators are coupled. Honeyands and Herbertson<sup>5</sup> and Kalter et al.<sup>7</sup> hypothesized a mechanism for these anti-symmetric oscillations. This mechanism is based on the pressure deficit in the recirculation zones that form due to the confinement and both jets.

Large scale self-sustained oscillations are also found in more fundamental flow configurations, such as a single jet in a confined cavity. Similar to the bifurcated jet, the proposed physical mechanism behind these oscillations is based on the pressure deficit in the recirculation zones that form due to the confinement.

The observation of these pressure deficits in oscillating recirculation zones is difficult to realize experimentally, which makes the proof for these hypotheses difficult. Numerical simulations on the other hand, can provide full space and time resolved fields of the velocity and pressure throughout the domain. This leads us to the first research question

*Can we prove the pressure based mechanism for self-sustained single and bifurcated jet oscillations in a thin cavity?*

### 1.3.2 Prediction of large scale jet oscillations in a thin cavity

The occurrence and frequency of the large scale self-sustained flow oscillations depend on the geometry of the cavity and the flow properties. To obtain this dependence, parameter studies can be carried out both numerically and experimentally, but in both approaches this will require extensive effort. The ability for a priori prediction of the occurrence and frequency of these large scale oscillations would therefore be of great practical value. Simple, zero-dimensional models can be found in literature, that describe various types of oscillations in nature and technology.

This motivated us to address the question

*How can jet oscillations in a confined cavity be represented by a simple, predictive model?*

### 1.3.3 Electromagnetic flow control of jet oscillations in a thin cavity

Body forces can be used to enhance or suppress flow oscillations. In steel casting, for example, electromagnetic forcing is widely used to suppress flow oscillations. The applicabil-

ity of the developed predictive model becomes more apparent when this model additionally incorporates body forces, such as the electromagnetic force. These electromagnetic body forces can have a significant influence on fluid flows.<sup>8-11</sup>

This leads us to the research question

*How can body forces, such as the electromagnetic force, be incorporated into a simple, predictive model for self-sustained flow oscillation in a confined cavity?*

### **1.3.4 Magnetohydrodynamic free surface flow in a shallow cavity**

The electromagnetic control of large scale oscillations also influences the behavior of the free surface. This may, in principle, again be studied by numerical flow simulations. Even though several authors have combined the physics of free surface flows and MHD in numerical simulations,<sup>12,14-18,23</sup> their validation has been very limited. Also, for MHD free surface flows, simple test problems, preferably with analytical solutions, are not encountered in literature. Experiments<sup>2,13</sup> are not generally suitable for verification, due to the difficulty of the proper definition of boundary conditions. This leads us to the following research question

*Can we devise a simple, analytically tractable benchmark problem for magnetohydrodynamic free surface flow, including the relevant electromagnetic, surface tension and gravity forces?*

From a numerical perspective, such a benchmark problem is a powerful tool for thorough validation of computational methods. Algorithms that do not pass these tests, should not be applied on more complicated configurations.

## **1.4 Funding of this PhD thesis**

This thesis presents research that has been part of project 10488 funded by the Dutch Technology Foundation (STW). Partners in this project were Tata Steel Europe, ABB and VorTech. Furthermore, support was received from SURFsara for using the Lisa Compute Cluster, project MP-235-12.

## **1.5 Outline**

The outline of the thesis is as follows. In chapter 2 we present relevant details of the numerical methods, as far as those are not addressed in the other chapters. The first research question will be addressed in chapters 4 and 6. The second and third research question are addressed in chapters 4 and 5 respectively. The fourth research question will be the subject of chapter 3. In chapter 7 we will discuss our main findings and discuss opportunities in potential future research.



## Bibliography

- [1] Abbel, G. Continugieten van plakken bij Corus IJmuiden: Achtergronden en Geschiedenis. Technical report, Corus IJmuiden, IJmuiden (2000).
- [2] Alpher, R. A., Hurwitz, H., Johnson, R. H., and White, D. R. Some Studies of Free-Surface Mercury Magneto-hydrodynamics. *Reviews of Modern Physics*, volume 32(4):pp. 758–769 (1960).
- [3] Cukierski, K. and Thomas, B. G. Flow Control with Local Electromagnetic Braking in Continuous Casting of Steel Slabs. *Metallurgical and Materials Transactions B*, volume 39(1):pp. 94–107 (2007).
- [4] Hibbeler, L. and Thomas, B. Mold slag entrainment mechanisms in continuous casting molds. *Iron and Steel Technology*, volume 10(10):pp. 121–136 (2013).
- [5] Honeyands, T. and Herbertson, J. Flow dynamics in thin slab caster moulds. *Steel Research International*, volume 66(7):pp. 287–293 (1995).
- [6] Kalter, R. *Electromagnetic control of oscillating flows in a cavity*. Ph.D. thesis, Delft, University of Technology (2014).
- [7] Kalter, R., Tummers, M. J., Kenjereš, S., Righolt, B. W., and Kleijn, C. R. Oscillations of the fluid flow and the free surface in a cavity with a submerged bifurcated nozzle. *International Journal of Heat and Fluid Flow* (2013).
- [8] Kenjereš, S. Electromagnetic enhancement of turbulent heat transfer. *Physical Review E*, volume 78(6):p. 066309 (2008).
- [9] Kenjereš, S. Large eddy simulations of targeted electromagnetic control of buoyancy-driven turbulent flow in a slender enclosure. *Theoretical and Computational Fluid Dynamics*, volume 23(6):pp. 471–489 (2009).
- [10] Kenjereš, S. and Hanjalić, K. On the implementation of effects of Lorentz force in turbulence closure models. *International Journal of Heat and Fluid Flow*, volume 21(3):pp. 329–337 (2000).
- [11] Kenjereš, S. and Hanjalić, K. Numerical simulation of magnetic control of heat transfer in thermal convection. *International Journal of Heat and Fluid Flow*, volume 25(3):pp. 559–568 (2004).
- [12] Miao, X., Lucas, D., Ren, Z., Eckert, S., and Gerbeth, G. Numerical modeling of bubble-driven liquid metal flows with external static magnetic field. *International Journal of Multiphase Flow*, volume 48:pp. 32–45 (2013).
- [13] Morley, N. B., Gaizer, A. A., Tillack, M. S., and Abdou, M. A. Initial liquid metal magnetohydrodynamic thin film flow experiments in the McGA-loop facility at UCLA. *Fusion Engineering and Design*, volume 27(0):pp. 725–730 (1995).
- [14] Samulyak, Bo, Li, Kirk, and McDonald. Computational algorithms for multiphase magnetohydrodynamics and applications to accelerator targets. *Condensed Matter Physics*, volume 13:p. 43402 (2010).
- [15] Samulyak, R., Du, J., Glimm, J., and Xu, Z. A numerical algorithm for MHD of free surface flows at low magnetic Reynolds numbers. *Journal of Computational Physics*, volume 226(2):pp. 1532–1549 (2007).
- [16] Tagawa, T. Numerical Simulation of a Falling Droplet of Liquid Metal into a Liquid Layer in the Presence of a Uniform Vertical Magnetic Field. *ISIJ International*, volume 45(7):pp. 954–961 (2005).
- [17] Tagawa, T. Numerical Simulation of Liquid Metal Free-surface Flows in the Presence of a Uniform Static Magnetic Field. *ISIJ International*, volume 47(4):pp. 574–581 (2007).
- [18] Tagawa, T. and Ozoe, H. Effect of external magnetic fields on various free-surface flows. *Progress in Computational Fluid Dynamics, An International Journal*, volume 8(7):p. 461 (2008).
- [19] van Vliet, E. Numerical simulations of the electromagnetic controlled solidifying mould flow in a steel caster using OpenFOAM. *Workshop on Numerical Simulations of MHD Flow* (2010).
- [20] Wang, J., Zhu, M., Zhou, H., and Wang, Y. Fluid Flow and Interfacial Phenomenon of Slag and Metal in Continuous Casting Tundish With Argon Blowing. *Journal of Iron and Steel Research, International*,

volume 15(4):pp. 26–31 (2008).

- [21] World Steel Association. *Steel Statistical Yearbook 2011*. World Steel Association (2011).
- [22] World Steel Association. *Steel Statistical Yearbook 2013*. World Steel Association (2013).
- [23] Zhang, C., Eckert, S., and Gerbeth, G. The Flow Structure of a Bubble-Driven Liquid-Metal Jet in a Horizontal Magnetic Field. *Journal of Fluid Mechanics*, volume 575:pp. 57–82 (2007).



## 2. Methods

### 2.1 Introduction

The numerical simulations performed in this thesis have been performed within the *OpenFOAM*<sup>18</sup> framework. Several extensions have been implemented during the course of the project. In this chapter we will more extensively describe parts of the numerical methods, as far as they have not been addressed in the consecutive chapters. In section 2.2 we describe one-way coupled magnetohydrodynamics (MHD) and in section 2.3 we describe the single phase one-way coupled MHD solver. In sections 2.4 and 2.5 implementation details of the MHD free surface solvers are described, combining MHD with the Volume Of Fluid (VOF) and Moving Mesh Interface Tracking (MMIT) method respectively. In section 2.6 a description of the LES model is given and in section 2.7 relevant information on the boundary condition in the LES model is presented.

### 2.2 One-way coupled magnetohydrodynamics

Magnetohydrodynamics describes the interaction between electromagnetic fields and fluid flow and exists in different flavours. In liquid metal MHD, the induced magnetic field is small in comparison to the imposed magnetic field. This one-way coupled MHD in which the imposed magnetic field influences the flow, but the magnetic field is not influenced by the flow, is described by conservation of mass, momentum and charge, which respectively reduce to<sup>4</sup>

$$\nabla \cdot \mathbf{u} = 0, \quad (2.1)$$

$$\frac{\partial \mathbf{u}}{\partial t} + (\mathbf{u} \cdot \nabla) \mathbf{u} = \frac{1}{\rho} \nabla p + \nabla \cdot (\nu \nabla \mathbf{u}) + \frac{1}{\rho} \mathbf{f}_L, \quad (2.2)$$

$$\nabla \cdot \mathbf{j} = 0. \quad (2.3)$$

Here,  $\mathbf{u}$  is the fluid velocity,  $\rho$  the fluid density,  $p$  the pressure,  $\nu$  the kinematic viscosity of the fluid,  $\mathbf{f}_L$  the Lorentz force and  $\mathbf{j}$  the electrical current density. The Lorentz force is expressed as

$$\mathbf{f}_L = \mathbf{j} \times \mathbf{b}, \quad (2.4)$$

where  $\mathbf{b}$  is the externally imposed magnetic field. The electrical current density is expressed using Ohm's law for a moving conducting fluid, as

$$\mathbf{j} = \sigma (-\nabla\phi + \mathbf{u} \times \mathbf{b}), \quad (2.5)$$

where  $\sigma$  is the electrical conductivity of the fluid and  $\phi$  the electric potential.

The one-way coupled MHD approximation is valid when the magnetic Reynolds number  $Re_m = \mu\sigma u_0 l \ll 1$ , where  $\mu$  is the magnetic permeability,  $u_0$  a characteristic velocity scale and  $l$  a characteristic length scale.

## 2.3 One-way coupled magnetohydrodynamics solver

The numerical solver for one-way coupled MHD simulations used in this thesis (chapter 5), which is also a basis for the free surface solvers as discussed below, is built on the *pimpleFoam* solver and pre-dominantly based on Van Vliet<sup>24</sup>. The main addition to the native PISO algorithm<sup>8,9</sup> in OpenFOAM is the step where the equation for the electric potential,  $\phi$ , is solved.<sup>11</sup> Combining conservation of charge and Ohm's law (equations 2.3 and 2.5) leads, for constant electrical conductivity, to the Poisson equation:

$$\nabla^2\phi = \nabla \cdot (\mathbf{u} \times \mathbf{b}). \quad (2.6)$$

In *pimpleFoam*, this Poisson equation is implemented within the *OpenFOAM 2.1* framework using the object oriented basis of the software. This results in equation 2.6 being solved in each time-step. From  $\phi$ , the current  $\mathbf{j}$  is calculated (equation 2.5), and then the Lorentz force  $\mathbf{f}_L$  (equation 2.4) is determined.

Furthermore, Van Vliet<sup>24</sup> implemented the four step projection method after Ni et al.<sup>17</sup> in this numerical solver. This means that the terms  $\mathbf{u} \times \mathbf{b}$  in equations 2.5 and 2.6 are evaluated at grid cell face centers rather than grid cell centers. This is a conservative scheme, which becomes especially important in higher Hartmann number (see equation 2.7) flows, as it guarantees the balance between pressure and Lorentz force at the cell center.

We demonstrate validation of the numerical solver with laminar Hartmann flow.<sup>4</sup> Hartmann flow is the flow of a fluid with viscosity  $\nu$  and electrical conductivity  $\sigma$  between two isolating flat plates separated by a distance  $2w$ , driven by a pressure gradient  $\frac{\partial p}{\partial x}$ , under the influence of a transversal magnetic field  $\mathbf{b} = b\hat{y}$ , and optionally a spanwise electric field  $\mathbf{e} = e_0\hat{z}$ . With  $\mathbf{u} = u(y)\hat{x}$  the solution to this problem is

$$\frac{u(y)}{u_0} = \left(1 - \frac{\cosh\left(Ha\frac{y}{w}\right)}{\cosh Ha}\right), \quad \sigma b^2 u_0 = -\frac{\partial p}{\partial x} - \sigma e_0 b, \quad Ha = bw\sqrt{\frac{\sigma}{\rho\nu}}. \quad (2.7)$$

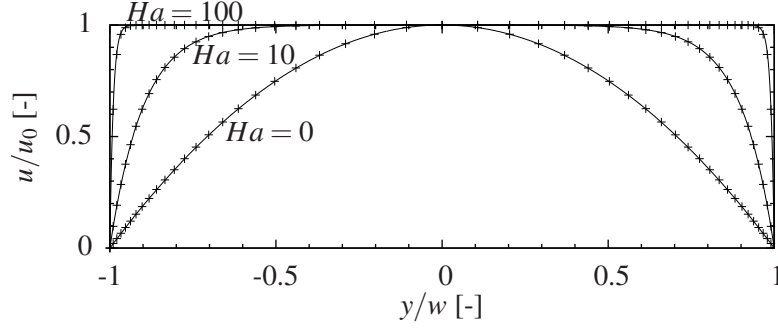


**Figure 2.1** Analytical (solid lines) and numerical (symbols) solution for Poiseuille flow ( $Ha = 0$ ) and Hartmann flow ( $Ha = 10$  and  $Ha = 100$ ) at  $Re = 10$ .

For  $Re = 10$ , Figure 2.1 shows the numerical and analytical solutions for  $Ha = 0$ ,  $Ha = 10$  and  $Ha = 100$ .

## 2.4 Volume of fluid and magnetohydrodynamics

The Volume of Fluid (VOF) method for simulating two immiscible fluids is based on solving a transport equation for an indicator function, which determines the separation between the two fluids.<sup>7,20</sup> The Continuum Surface Force (CSF) approach is used for implementation of the interfacial tension force<sup>2</sup> and an artificial compression velocity is introduced for maintaining a sharp interface.<sup>26</sup>

The describing equations for two-phase VOF flows are the continuity equation (see equation 2.1) and the Navier-Stokes equations,<sup>2,7</sup>

$$\frac{\partial \rho u_i}{\partial t} + u_j \frac{\partial \rho u_i}{\partial x_j} = -\frac{\partial p}{\partial x_i} + \frac{\partial}{\partial x_j} \left[ \mu \left( \frac{\partial u_i}{\partial x_j} + \frac{\partial u_j}{\partial x_i} \right) \right] + f_i + \gamma \kappa \frac{\partial \alpha}{\partial x_i}, \quad (2.8)$$

where  $\alpha$  is the indicator function,  $f_i$  the body force,  $\rho$  and  $\mu$  the phase averaged density and viscosity (i.e.  $\rho = \alpha \rho_1 + (1 - \alpha) \rho_2$ ) and  $\kappa$  the curvature of the interface in the CSF approach,<sup>2</sup> determined by

$$\kappa = \frac{\partial}{\partial x_k} \left[ \frac{1}{\left| \frac{\partial \alpha}{\partial x_j} \right|} \frac{\partial \alpha}{\partial x_k} \right]. \quad (2.9)$$

and the transport equation for the indicator function  $\alpha$ <sup>20</sup>

$$\frac{\partial \alpha}{\partial t} + \frac{\partial}{\partial x_j} (\alpha u_j) + \frac{\partial}{\partial x_j} (u_{r,i} \alpha (1 - \alpha)) = 0. \quad (2.10)$$

The indicator function equals 1 for the first fluid and 0 for the second fluid and is in the range  $(0, 1)$  around the interface, as indicated in Figure 2.2. The third term includes the artificial compression velocity,  $u_{r,i}$  and is zero outside the interface region. This term can be derived from the continuity equations for the fluid fractions in the two-fluid Euler approach, leading to the relative velocity  $u_{r,i} = u_{1,i} - u_{2,i}$  between both fluids.<sup>1</sup> The term compressibility does not refer to compression of the distinct fluids, but compression of the interface itself, which can be seen as additional convection of the fluid fraction due to  $u_{r,i}$ . For the theoretical infinitesimally thin interface, the third term in equation 2.10 will vanish, leading to the conventional VOF equation.

In the one-way coupled MHD-VOF solver, the body force  $f_i$  is the Lorentz force (see equation 2.4), which is responsible for the interaction with the magnetic field. From conservation of charge (equation 2.3) and the definition of the current density (equation 2.5), a Poisson equation for the electric potential is derived:

$$\frac{\partial}{\partial x_i} \left( \sigma \frac{\partial \phi}{\partial x_i} \right) = \frac{\partial}{\partial x_i} (\sigma \epsilon_{ijk} u_j b_k). \quad (2.11)$$

This equation differs from single phase MHD equations, as the electrical conductivity  $\sigma$  is generally different across the fluids.  $\sigma$  is linearly interpolated between both fluids, which means harmonic interpolation on the resistivity, i.e.

$$\sigma = \alpha \sigma_1 + (1 - \alpha) \sigma_2 \text{ or } \frac{1}{\rho_e} = \frac{\alpha}{\rho_{e,1}} + \frac{1 - \alpha}{\rho_{e,2}}, \text{ with } \rho_e = \frac{1}{\sigma}. \quad (2.12)$$

We will use the VOF method for free surface flows, i.e., fluid 1 is the liquid, which is water, salty water or another electrically conductive fluid, and fluid 2 is air.

## 2.5 MMIT Magnetohydrodynamics

The moving mesh interface tracking (MMIT) method is based on aligning a boundary of the numerical mesh with the interface between two phases, as is shown in Figure 2.2. This results in a sharp interface by definition and allows for the implementation of exact boundary conditions at the interface. The approach as proposed by Muzaferija and Perić<sup>16</sup> and the implementation by Tuković and Jasak<sup>23</sup> was used. A separate mesh is constructed for each fluid phase. When the flow field changes in time, first the mesh on this boundary is updated accordingly and second the interior mesh points are adjusted based on the free surface movement.

The moving mesh interface tracking method introduces in addition to continuity and momentum equations the so called space conservation law, i.e.

$$\frac{d}{dt} \int_V dV - \int_S n_i u_{s,i} dS = 0, \quad (2.13)$$

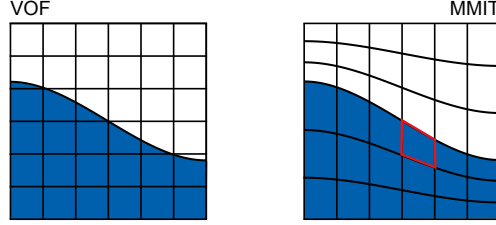


**Figure 2.2** Schematic representation of the VOF (left) and MMIT (right) methods. The blue control volumes indicate the liquid phase, and the white control volumes the gas phase.

where  $u_{s,i}$  is the velocity of the face  $S$  and  $n_i$  the outward face normal. This velocity of each face of every control volume  $V$  has to be accounted for in the integrated momentum equations,<sup>16,23</sup> in terms of an additional flux  $-\rho u_{s,j} u_i$ .

For the interface, the boundary condition can be exactly imposed at the mesh boundary, e.g. no mass should cross the boundary and the stresses at opposite sides of the interface should match. Non-zero mass fluxes through the interface are corrected by moving the boundary. This correction is used as a boundary condition in the Poisson equation for moving the interior points in the domain by an amount  $d_i$ :

$$\frac{\partial}{\partial x_j} \left( \Gamma \frac{\partial d_i}{\partial x_j} \right) = 0, \quad (2.14)$$

where  $\Gamma$  is a diffusion parameter that is inversely proportional to the square of the distance to the free surface.

For the implementation of the magnetohydrodynamic force, the Poisson equation for the electric potential is solved (as described in section 2.4), and the Lorentz force calculated and applied between mesh updates, which hence does not need further treatment. When the second fluid is non-conducting, the boundary condition for the electric potential  $\phi$  needs to account for a non-zero Lorentz force, as the velocity is non-zero, hence

$$\frac{d\phi}{dn} = n_i \epsilon_{ijk} u_j b_k, \quad (2.15)$$

where  $n_i$  is the surface normal vector of the interface, as defined by the mesh. This boundary condition is schematically shown in Figure 2.3.

We will use the MMIT method for water-air free surface flows. Air, being the top-layer, has a negligible influence on the free surface behavior. Therefore, the secondary mesh can be omitted from the simulation domain.



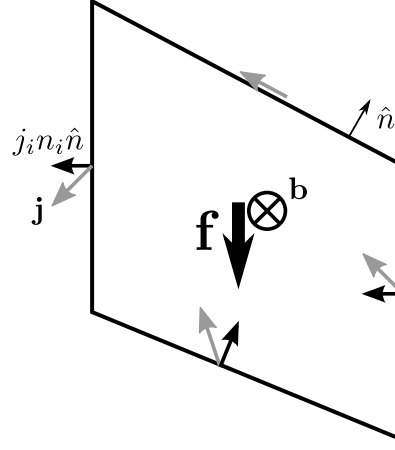


**Figure 2.3** Control volume in the MMIT method, indicating the interface condition, as the flow normal to the interface is zero. The definition of the current at boundaries of the control volume (gray arrows,  $\mathbf{j}$ ), the face normal ( $\hat{\mathbf{n}}$ ), the face normal component of the current (black arrows,  $j_i n_i \hat{\mathbf{n}}$ ) and the resulting Lorentz force (thick arrow,  $\mathbf{f}$ ).

## 2.6 Dynamic Smagorinsky model

To account for the turbulence in the liquid flow, we apply the Large Eddy Simulation (LES) approach. In LES, one decomposes the instantaneous velocity into a filtered velocity and a residual velocity:  $U_i = \bar{u}_i + u'_i$ . The filtered velocity,  $\bar{u}_i$  is the part of the velocity that can be represented by the mesh and can be solved for. The residual velocity  $u'_i$  represents the contribution of the smallest, subgrid-sized eddies which cannot be solved.<sup>19</sup> We denote the implicit filtering operation by  $(\bar{\cdot})$ .

After applying the filter on the Navier-Stokes equations (equation 2.2):

$$\frac{\partial \bar{u}_i}{\partial t} + \bar{u}_j \frac{\partial \bar{u}_i}{\partial x_j} = -\frac{1}{\rho} \frac{\partial p}{\partial x_i} + \frac{\partial}{\partial x_j} \left( \nu \frac{\partial \bar{u}_i}{\partial x_j} - \tau_{ij}^R \right), \quad (2.16)$$

where  $\tau_{ij}^R$  is the residual stress, defined as

$$\tau_{ij}^R = \overline{U_i U_j} - \bar{u}_i \bar{u}_j. \quad (2.17)$$

Furthermore, the anisotropic residual-stress tensor  $\tau_{ij}^r = \tau_{ij}^R - \frac{2}{3} k^r \delta_{ij}$  is used instead of the residual-stress tensor, where  $k^r = \frac{1}{2} \tau_{ii}^R$  is the residual kinetic energy. Now the isotropic part is incorporated in the filtered pressure  $p = p + \frac{2}{3} k^r$ . The anisotropic residual-stress tensor is the component of the filtered Navier-Stokes equations that needs to be modelled.

The dynamic Smagorinsky model<sup>6,13</sup> is an improved version of the standard Smagorinsky model.<sup>21</sup> In the standard Smagorinsky model, the residual stress is modelled as:

$$\tau_{ij}^r = -2\nu_r \overline{S}_{ij}, \quad \nu_r = (C_S \Delta)^2 \overline{S}, \quad \mathcal{S} = (2\overline{S}_{ij} \overline{S}_{ij})^{1/2}, \quad \overline{S}_{ij} = \frac{1}{2} \left( \frac{\partial \overline{u}_i}{\partial x_j} + \frac{\partial \overline{u}_j}{\partial x_i} \right). \quad (2.18)$$

where  $\nu_r$  is the eddy viscosity of the residual motions,  $\overline{S}$  the characteristic rate of strain,  $\overline{S}_{ij}$  the filtered rate of strain and  $C_S$  is the Smagorinsky coefficient, a model parameter, typically taking a value between 0.05 and 0.2.

In the dynamic Smagorinsky model, the Smagorinsky coefficient is not constant and based on the local flow conditions. It has the advantage that it correctly handles differences in turbulence intensities throughout the domain and intrinsically handles the damping of turbulence towards the walls. Furthermore, it was shown to be effective in modelling the subgrid scales in low magnetic Reynolds number MHD flows.<sup>12</sup>

The dynamic Smagorinsky model applies another filter, the test-filter. This filter is wider than the original filter (often twice as wide) and denoted by  $\widetilde{(\cdot)}$ . When the test filter of width  $\widetilde{\Delta}$  is applied a smaller part of the turbulent spectrum is resolved, as compared to the originally applied filter with width  $\Delta$ . In the overlapping part of the spectrum, that is, the part smaller than the double filter width, but larger than the original filter width, two different expressions for the subgrid scale stress will provide a local, dynamic Smagorinsky coefficient.

The subgrid scale stress,  $\tau_{ij}^r$  follows from equations 2.18 and the subtest scale stress  $T_{ij}$  is calculated in a similar way on the wider test filter<sup>19</sup>

$$\tau_{ij}^r = -2c_S \Delta^2 \overline{S} \overline{S}_{ij}, \quad T_{ij} = -2c_S \widetilde{\Delta}^2 \widetilde{\mathcal{S}} \widetilde{S}_{ij}, \quad (2.19)$$

where  $c_S = C_S^2$ .

The contribution to the resolved stress tensor by the scales of motion in between the two filter widths,  $L_{ij}$ , can be shown to be

$$L_{ij} = T_{ij} - \widetilde{\tau}_{ij}^r = \widetilde{\overline{u}_i \overline{u}_j} - \overline{u}_i \overline{u}_j \quad (2.20)$$

and also

$$L_{ij} = -2c_S M_{ij}, \quad (2.21)$$

with

$$M_{ij} = \Delta^2 \widetilde{\mathcal{S}} \widetilde{S}_{ij} - \widetilde{\Delta}^2 \widetilde{\mathcal{S}} \widetilde{S}_{ij}. \quad (2.22)$$

The difference between the two expressions is minimized with a least squares method, which will result in

$$c_S = \frac{1}{2} \frac{L_{ij} M_{ij}}{M_{ij}^2}. \quad (2.23)$$

A problem is that  $c_S$  may become too large locally.<sup>13</sup> Two possible solutions are (i) to apply some (local) averaging or (ii) to truncate isolated large values of  $c_S$ . We follow the approach

for local averaging as outlined by Zang et al.<sup>27</sup> which is the area weighted average of the face-interpolated values of  $L_{ij}M_{ij}$  and  $M_{ij}^2$ , which, on hexahedral cells for arbitrary variable  $f$  becomes

$$\langle f \rangle = \frac{1}{2}f + \frac{1}{12} \sum_{nb=1}^6 f_{nb}, \quad (2.24)$$

with  $\langle \cdot \rangle$  denoting the averaging procedure, such that the local coefficient becomes

$$c_S = \frac{1}{2} \frac{\langle L_{ij}M_{ij} \rangle}{\langle M_{ij}^2 \rangle}. \quad (2.25)$$

For the test-filter operation  $\widetilde{(\cdot)}$ , we use the following filter, universally applicable for all kinds of meshes

$$\widetilde{u}_i = \frac{\sum_f A_f \bar{u}_{f,i}}{\sum_f A_f} \quad (2.26)$$

where  $\bar{u}_{f,i}$  is the face-interpolated value and  $A_f$  is the face surface area. Please note that in the remainder of this thesis we will omit in our notation the overline of the implicit filtering operation, and denote  $\bar{u}_i$  by  $u_i$ .

This dynamic Smagorinsky model is also applied in our free surface (VOF) simulations. This is valid, because the Reynolds stresses are effectively weighted by the volume fraction  $\alpha$ .<sup>14</sup>

## 2.7 Spalding's Law

In wall-bounded Large Eddy Simulations, where, depending on the grid size and flow conditions at the boundary, the boundary layer may or may not be fully resolved, a universal velocity profile should be imposed as boundary condition in near-wall cells in terms of wall-units  $y^+ = yu_\tau/\nu$  and  $u^+ = u/u_\tau$  when  $y^+ > 1$ .  $u_\tau$  is the friction velocity,

$$u_\tau = \sqrt{(\nu + \nu_{SGS}) \frac{\partial u}{\partial n}}, \quad (2.27)$$

An example of such a universal wall function is Spalding's law,<sup>5,15,22,25</sup> which implicitly gives  $u^+$  as a function of  $y^+$ :

$$y^+ = u^+ + \frac{1}{E} \left[ e^{\kappa u^+} - \left( 1 + \kappa u^+ + \frac{1}{2}(\kappa u^+)^2 + \frac{1}{6}(\kappa u^+)^3 \right) \right], \quad (2.28)$$

where  $E = 9.8$  and  $\kappa = 0.41$ , which is a unification of the log law  $u^+ = \frac{1}{\kappa} \ln(y^+) + B$  and the viscous profile  $u^+ = y^+$ .<sup>19</sup> The shape of the universal Spalding's law, the log law and the viscous profile are shown in Figure 2.4.

A common approach for the implementation of wall functions is to calculate the friction velocity  $u_\tau$  (equation 2.27), calculate  $y^+$  from the wall-distance  $y$ , find  $u^+$  from the wall-function

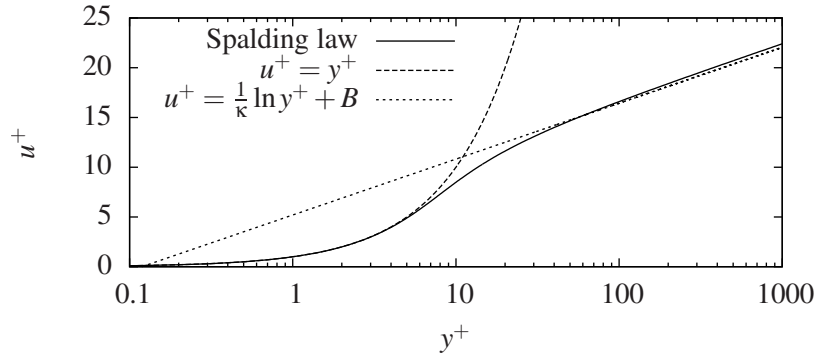


**Figure 2.4** Spaldings law in wall-units (solid line), compared to the log law (long dash, with  $B = 5.2$  and  $\kappa = 0.41$ ) and the viscous layer (short dash).

(equation 2.28), calculate the wall-parallel velocity component  $u$  and impose that value at the first grid cell near the wall,<sup>3</sup> which in principle turns it into a slip velocity condition.

The implementation in OpenFOAM differs from the above, as the wall function is imposed as a momentum source at the boundary.<sup>10</sup> This is realized via the value of the sub-grid-scale viscosity,  $\nu_{SGS}$  at the wall. Physically,  $\nu_{SGS,w} = 0$ , however, here a non-zero value introduces a momentum flux in the discretized form of the Navier-Stokes equations. In the context of the computational algorithm, it can be summarized as follows, with the superscript  $n$  denoting the time step index:

1. The PISO algorithm is used to calculate  $u_i^n, p^n$ .
2. The LES model is applied to compute  $\nu_{SGS}^n$ .
3. For each boundary grid cell,  $u_\tau$  is calculated from  $u_i^n$  and  $\nu_{SGS,w}^n$ .
4. An updated  $\nu_{SGS,w}$  is determined
  - For very small  $u_\tau$ ,  $\nu_{SGS,w} = 0$ , the wall region is fully resolved, and no further steps are necessary.
  - For larger  $u_\tau$ , equation 2.28, which is implicit in  $u_\tau$  via  $y^+$  and  $u^+$  is iteratively solved for  $u_\tau$ .
5.  $\nu_{SGS,w}^{n+1}$  is calculated from  $u_\tau$  via equation 2.27 and hence acts as a momentum source in the next time-step, which repeats at step 1.

## Bibliography

- [1] Berberović, E., van Hinsberg, N. P., Jakirlić, S., Roisman, I. V., and Tropea, C. Drop impact onto a liquid layer of finite thickness: Dynamics of the cavity evolution. *Physical Review E*, volume 79(3):p. 036306 (2009).
- [2] Brackbill, J. U., Kothe, D. B., and Zemach, C. A continuum method for modeling surface tension. *Journal of Computational Physics*, volume 100(2):pp. 335–354 (1992).
- [3] Chung, T. J. *Computational Fluid Dynamics*. Cambridge University Press, 1 edition (2002).
- [4] Davidson, P. A. *An Introduction to Magnetohydrodynamics*. Cambridge University Press, 1 edition (2001).
- [5] Duprat, C., Balarac, G., Métais, O., Congedo, P. M., and Brugire, O. A wall-layer model for large-eddy simulations of turbulent flows with/out pressure gradient. *Physics of Fluids*, volume 23(1):p. 015101 (2011).
- [6] Germano, M., Piomelli, U., Moin, P., and Cabot, W. H. A dynamic subgrid-scale eddy viscosity model. *Physics of Fluids A: Fluid Dynamics*, volume 3(7):p. 1760 (1991).
- [7] Hirt, C. and Nichols, B. Volume of fluid (VOF) method for the dynamics of free boundaries. *Journal of Computational Physics*, volume 39(1):pp. 201–225 (1981).
- [8] Issa, R. I. Solution of the implicitly discretised fluid flow equations by operator-splitting. *Journal of Computational Physics*, volume 62(1):pp. 40–65 (1986).
- [9] Jasak, H. *Error Analysis and Estimation for the Finite Volume Method with Applications to Fluid Flows*. Ph.D. thesis, Imperial College, London (1996).
- [10] Jones, W. P. Turbulence modelling and numerical solution methods for variable density and combusting. In Libby, P. A. and Williams, F. A., editors, *Turbulent Reacting Flows*, pp. 309–374. Academic Press Inc. (1994).
- [11] Kenjereš, S. and Hanjalić, K. On the implementation of effects of Lorentz force in turbulence closure models. *International Journal of Heat and Fluid Flow*, volume 21(3):pp. 329–337 (2000).
- [12] Knaepen, B. and Moin, P. Large-eddy simulation of conductive flows at low magnetic Reynolds number. *Physics of Fluids*, volume 16(5):p. 1255 (2004).
- [13] Lilly, D. K. A proposed modification of the Germano subgrid-scale closure method. *Physics of Fluids A: Fluid Dynamics*, volume 4(3):p. 633 (1992).
- [14] Liovic, P. and Lakehal, D. Interface-turbulence interactions in large-scale bubbling processes. *International Journal of Heat and Fluid Flow*, volume 28(1):pp. 127–144 (2007).
- [15] Martín-Alcntara, A., Sanmiguel-Rojas, E., Gutirrez-Montes, C., and Martnez-Bazan, C. Drag reduction induced by the addition of a multi-cavity at the base of a bluff body. *Journal of Fluids and Structures*, volume 48:pp. 347–361 (2014).
- [16] Muzaferija, S. and Perić, M. Computation of Free-Surface Flows using the Finite-Volume Method and Moving Grids. *Numerical Heat Transfer, Part B: Fundamentals*, volume 32(4):pp. 369–384 (1997).
- [17] Ni, M.-J., Munipalli, R., Morley, N., Huang, P., and Abdou, M. A current density conservative scheme for incompressible MHD flows at a low magnetic Reynolds number. Part I: On a rectangular collocated grid system. *Journal of Computational Physics*, volume 227(1):pp. 174–204 (2007).
- [18] OpenCFD Ltd. The Open Source Computational Fluid Dynamics (CFD) Toolbox (12/2011).
- [19] Pope, S. B. *Turbulent Flows*. Cambridge University Press, Cambridge, 1 edition (2000).
- [20] Rusche, H. *Computational Fluid Dynamics of Dispersed Two-Phase Flows at High Phase Fractions*. PhD thesis, Imperial College (2002).
- [21] Smagorinsky, J. General circulation experiments with the primitive equations I. The basic experiment. *Monthly Weather Review*, volume 91(3):pp. 99–164 (1963).
- [22] Spalding, D. B. A single formula for the law of the wall. *Journal of Applied Mechanics*, volume 28:pp. 455–458 (1961).

- 
- [23] Tuković, Ž. and Jasak, H. A moving mesh finite volume interface tracking method for surface tension dominated interfacial fluid flow. *Computers and Fluids*, volume 55:pp. 70–84 (2012).
  - [24] Van Vliet, E. Personal communication (2010-2014).
  - [25] de Villiers, E. *The Potential of Large Eddy Simulation for the Modeling of Wall Bounded Flows*. PhD thesis, Imperial College, London (2006).
  - [26] Weller, H. G. A New Approach to VOF-based Interface Capturing Methods for Incompressible and Compressible Flow. Technical report, OpenCFD (2008).
  - [27] Zang, Y., Street, R. L., and Koseff, J. R. A dynamic mixed subgrid-scale model and its application to turbulent recirculating flows. *Physics of Fluids A: Fluid Dynamics*, volume 5(12):pp. 3186–3196 (1993).



### 3. Analytical solutions of one-way coupled magnetohydrodynamic free surface flow<sup>§</sup>

We study the flow in a two-dimensional layer of conductive liquid under the influence of surface tension, gravity, and Lorentz forces due to imposed potential differences and transverse magnetic fields, as a function of the Hartmann number, the Bond number, the Reynolds number, the capillary number and the height-to-width ratio  $A$ . For aspect ratios  $A \ll 1$  and Reynolds numbers  $Re \leq A$ , lubrication theory is applied to determine the steady state shape of the liquid surface to lowest order. Assuming low Hartmann ( $Ha \leq O(1)$ ), capillary ( $Ca \leq O(A^4)$ ), Bond ( $Bo \leq O(A^2)$ ) numbers and contact angles close to  $90^\circ$ , the flow details below the surface and the free surface elevation for the complete domain are determined analytically using the method of matched asymptotic expansions. The amplitude of the free surface deformation scales linearly with the capillary number and decreases with increasing Bond number, while the shape of the free surface depends on the Bond number and the contact angle condition. The strength of the flow scales linearly with the magnetic field gradient and applied potential difference and vanishes for high aspect ratio layers ( $A \rightarrow 0$ ). The analytical model results are compared to numerical simulations using a finite volume moving mesh interface tracking (MMIT) method and a volume of fluid (VOF) method, where the Lorentz force is calculated from the equation for the electric potential. It is shown that the analytical result for the free surface elevation is accurate within 0.4% for MMIT and 1.2% for VOF when  $Ha^2 \leq 1$ ,  $Ca \leq A^4$ ,  $Bo \leq A^2$ ,  $Re \leq A$  and  $A \leq 0.1$ . For  $A = 0.1$ , the analytical solution remains accurate within 1% of the MMIT solution when either  $Ha^2$  is increased to 400,  $Ca$  to  $200A^4$  or  $Bo$  to  $100A^2$ .

<sup>§</sup>Parts of this chapter have been published as: Righolt, B. W., Kenjereš, S., Kalter, R., Tummers, M. J., and Kleijn, C. R. Analytical solutions of one-way coupled magnetohydrodynamic free surface flow *Applied Mathematical Modelling*, 2015



### 3.1 Introduction

Magnetohydrodynamic (MHD) free surface flow of a conductive liquid in a spatially non-uniform magnetic field is relevant to various applications in e.g. metallurgy<sup>11,14,18,28</sup> and crystal growth processes, such as Czochralski and Bridgman growth.<sup>12,14,30</sup>

Wall-bounded single phase MHD flow of a conducting liquid in a magnetic field has been the subject of many theoretical studies, e.g. pipe<sup>32</sup> and duct<sup>17</sup> flow in a uniform magnetic field, convection in a non-uniform magnetic field<sup>1</sup>, buoyancy driven Darcy flow in a uniform magnetic field<sup>5,9,26</sup>, and lubrication flow with injected currents.<sup>16</sup> Free surface MHD flow has been studied both theoretically and experimentally, e.g. driven by an imposed magnetic field,<sup>21</sup> by injected currents,<sup>19,25</sup> or due to buoyancy.<sup>33</sup>

In this chapter we will study the one-way coupled magnetohydrodynamic (MHD) free surface flow of a conductive fluid in a shallow, two-dimensional cavity subject to a differentially applied electric potential in a spatially non-uniform magnetic field. The Lorentz force will be the only driving force for the flow, while gravity and surface tension act as the restoring forces for the free surface deformation. We will use the analytical methods of lubrication theory and matched asymptotic expansions to determine the free surface elevation and flow inside the cavity. This combination of methods has been used previously to study flows in shallow cavities, for example in buoyancy driven single phase flow,<sup>7</sup> and later for free surface flow driven by a Marangoni force.<sup>29</sup> It has also been used for single phase MHD flow<sup>13</sup> and free surface MHD flow in a uniform magnetic field<sup>2</sup>. The combination of a free surface and a non-uniform magnetic field distinguishes our work from previous studies.

Our analytical solutions will subsequently be compared with numerical results from two finite volume based free surface, one-way coupled Navier-Stokes MHD flow solvers. The free surface is modelled using a moving mesh interface tracking (MMIT) method<sup>35</sup> and a volume of fluid (VOF) method. The electric potential in the one-way coupled MHD problem is calculated from a Poisson equation.

The goal of this chapter is to (i) find asymptotic analytical solutions for the flow in a conductive layer of fluid influenced by Lorentz, gravity and surface tension forces, (ii) validate the analytical solution and two different free surface MHD flow solvers against each other and (iii) use the numerical solvers to explore the parameter space, in terms of Hartmann number, capillary number, Bond number, Reynolds number and aspect ratio, for which the analytical solution is accurate. With the obtained knowledge about its accuracy and limitations, the presented asymptotic analytical solutions may subsequently serve as a benchmark for the validation of other numerical solvers for combined free surface and MHD flows.

This chapter is outlined as follows. The mathematical framework is presented in Section 3.2, this includes the derivation of the flow in the core, the free surface elevation and the turning flow near the side walls. Section 3.3 introduces both numerical MHD free surface flow solvers. In Section 3.3 we validate the numerical models and the analytical solution in terms of the various dimensionless numbers.

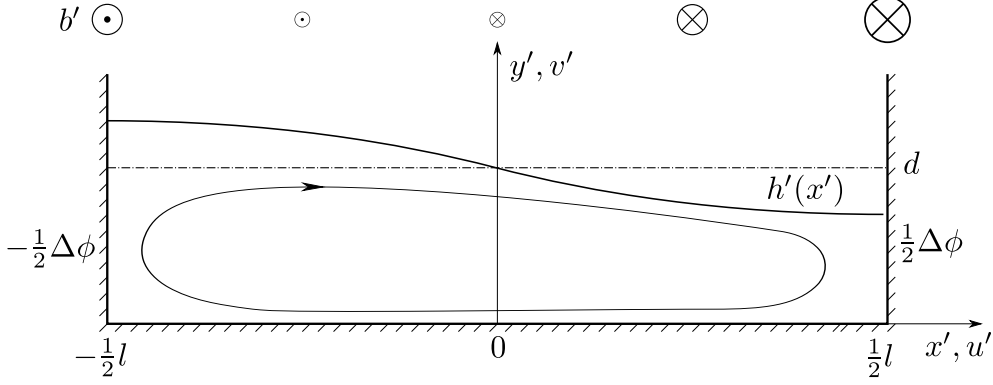


**Figure 3.1** Schematic representation of the two-dimensional liquid layer, with a potential difference  $\Delta\phi$  across the domain and an insulated bottom. The dash-dotted line is the undisturbed interface and the solid line  $h(x)$  is the equilibrium surface position after application of a magnetic field in the direction perpendicular to the  $xy$ -plane, where the relative field strength is indicated in the top.

## 3.2 Analytical derivation

We consider a two-dimensional, finite-size liquid layer of width  $l$  and initial height  $d$ , as depicted in Figure 3.1. The aspect ratio  $A$  of the cavity is defined as  $A = d/l$ . The liquid has an electrical conductivity  $\sigma$ , density  $\rho$  and kinematic viscosity  $\nu$ . The fluid above the liquid layer is assumed to have negligible electrical conductivity, density and viscosity. The surface tension between the two phases is denoted by  $\gamma$  and the downward directed gravitational force by  $g$ .

The left wall of the system is kept at a fixed electrical potential  $-\frac{1}{2}\Delta\phi$ , the right wall at  $\frac{1}{2}\Delta\phi$  and the bottom wall is electrically insulated. A magnetic field  $\mathbf{b}'/b_0 = -(\alpha z'/l)\hat{\mathbf{x}} - (1 + \alpha x'/l)\hat{\mathbf{z}}$  is imposed, which in the plane of interest, the  $z = 0$  plane, gives a linearly increasing magnetic field  $\mathbf{b}' = -b_0(1 + \alpha x'/l)\hat{\mathbf{z}}$ . The Lorentz force associated with this magnetic field has a zero  $z$ -component in the  $z = 0$  plane.

In equilibrium, a net current flows from the right to the left wall, which due to its interaction with the magnetic field leads to a Lorentz force  $\mathbf{f}' = \mathbf{j}' \times \mathbf{b}'$ . This causes a net downward force on the conducting liquid, which is stronger at the right side than at the left side. This will initiate a circulating flow inside the fluid that via pressure build-up deforms the interface. Viscous, gravitational and surface tension forces act to oppose the Lorentz force.

### 3.2.1 Conservation equations

The problem will be studied from the conservation equations for mass, momentum and current, which, for an incompressible, non-Newtonian fluid, read

$$\nabla' \cdot \mathbf{u}' = 0, \quad (3.1)$$

$$\frac{\partial \mathbf{u}'}{\partial t'} + (\mathbf{u}' \cdot \nabla') \mathbf{u}' = -\frac{1}{\rho} \nabla' p' + \nu \nabla'^2 \mathbf{u}' + \frac{1}{\rho} \mathbf{j}' \times \mathbf{b}' + \mathbf{g}', \quad (3.2)$$

$$\nabla' \cdot \mathbf{j}' = 0. \quad (3.3)$$

In this set of equations,  $\mathbf{u}'$  is defined as the velocity  $\mathbf{u}' = u' \hat{\mathbf{x}} + v' \hat{\mathbf{y}}$  and  $\mathbf{g}'$  is defined as the gravitational force  $\mathbf{g}' = -g \hat{\mathbf{y}}$ . The flow is not influencing the magnetic field, as the magnetic Reynolds number  $Re_m = \sigma \mu u^* l \ll 1$ , with  $\mu$  the magnetic permeability and  $u^*$  the characteristic velocity scale. Under these conditions, the current  $\mathbf{j}'$  can be deduced from Ohm's law for moving media via the electric potential  $\phi$  and is defined as  $\mathbf{j}' = \sigma (-\nabla' \phi' + \mathbf{u}' \times \mathbf{b}')$ .<sup>8</sup>

### 3.2.2 Boundary conditions

The liquid layer is bounded by four boundaries.

#### Walls

The walls are located at  $x' = -\frac{1}{2}l$ ,  $x' = \frac{1}{2}l$  and  $y' = 0$ , namely the left side wall, the right side wall and the bottom wall. The boundary conditions here are straightforward

1.  $x' = -\frac{1}{2}l$ :  $u' = v' = 0$  and  $\phi' = \frac{1}{2} \Delta \phi$
2.  $x' = \frac{1}{2}l$ :  $u' = v' = 0$  and  $\phi' = -\frac{1}{2} \Delta \phi$
3.  $y' = 0$ :  $u' = v' = 0$  and  $\phi'_{y'} = 0$

Thus, the side walls are kept at a fixed potential, while the bottom wall is insulated. All walls impose no-slip conditions for the fluid velocity.

#### Free surface

The free surface is located at  $y' = h'(x')$  and at this interface the kinematic condition holds. Surface tension acts against surface deformation and no current will flow across the interface.

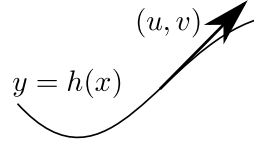


**Figure 3.2** The kinematic boundary condition can be derived from this figure.

**Kinematic condition** The kinematic boundary condition can be derived from the fact that no fluid moves from the interface into the second fluid, in other words (or see Figure 3.2).

$$\lim_{\Delta x' \rightarrow 0} \frac{h'(x' + \Delta x') - h'(x')}{\Delta x'} = h'_{x'} = \frac{v'}{u'} \quad (3.4)$$

$$u' h'_{x'} = v' \quad (3.5)$$

**Surface tension** To describe the surface tension, the normal and tangential vectors at the interface are defined (see Figure 3.3)

$$\hat{t} = \frac{1}{N}(1, h'_{x'}) \quad (3.6)$$

$$\hat{n} = \frac{1}{N}(-h'_{x'}, 1) \quad (3.7)$$

$$N = \sqrt{1 + h'^2_{x'}}. \quad (3.8)$$

Furthermore, the stress tensor is defined as

$$S'_{ij} = -p' \delta_{ij} + \mu(u'_{i,j} + u'_{j,i}). \quad (3.9)$$

Such that at the interface for constant surface tension  $\gamma$

$$S'_{ij} n_j t_i = 0 \quad (3.10)$$

$$S'_{ij} n_j n_i = \gamma K. \quad (3.11)$$

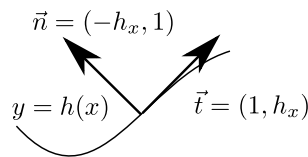


**Figure 3.3** The normal and tangential vectors at the interface.

The curvature  $K$  can be derived from  $K = \nabla \cdot n = n_{1x} + n_{2y} = \frac{h'_{x'x'}}{N^3}$ .

Evaluating the tangential component of Eq. 3.10 using the stress definition 3.9 gives

$$2h'_{x'}(v'_{y'} - u'_{x'}) + (1 - h'^2_{x'})(v'_{x'} + u'_{y'}) = 0. \quad (3.12)$$

And for the normal component (Eq. 3.11):

$$\gamma \frac{h'_{x'x'}}{N^3} = \frac{1}{N^2} \left[ (-p' + 2\mu u'_{x'})h'^2_{x'} + (-p' + 2\mu v'_{y'}) - 2\mu(u'_{y'} + v'_{x'})h'_{x'} \right] \quad (3.13)$$

**Current boundary condition** No current will flow across the interface, which results in the last boundary condition, which includes the electric potential:

$$j'_i n_i = 0, \quad (3.14)$$

With  $\vec{j}' = (-\phi'_{x'} + v'b', -\phi'_{y'} - u'b')$  this gives:

$$\phi'_{x'} h'_{x'} - \phi'_{y'} = b'(u' + v'h'_{x'}). \quad (3.15)$$

### Other constraints

Some other constraints can be derived for this system in steady state

- There is no net mass flow in the horizontal direction, thus

$$\int_0^{h'(x')} u'(x', y') dy' = 0. \quad (3.16)$$

- The total volume in the cavity is conserved, thus

$$\int_{-\frac{1}{2}l}^{\frac{1}{2}l} h'(x') dx' = V = ld. \quad (3.17)$$

- Finally the contact point behaviour at the three-phase point has to be described, which, for a certain contact angle  $\theta$ , reads

$$h'_{x'} \left( \pm \frac{1}{2} \right) = \mp A^{-1} \tan \left( \theta - \frac{\pi}{2} \right). \quad (3.18)$$

### 3.2.3 Lubrication theory

The mathematical formulation of the problem, does not have a simple, closed form solution of the differential equations. The lubrication theory will be applied to the problem, such that a solution can be derived for the centre of the domain, in the lowest order of the asymptotic limit (infinitely thin layer). This solution will then be matched with the outer flow near the walls.<sup>36</sup>

We will solve this problem in dimensionless, lubrication type variables,

$$\begin{aligned} x' &= lx, & y' &= dy, & h' &= dh, & u' &= u^*u, \\ v' &= Au^*v, & p' &= \frac{\mu u^* l}{d^2}p, & b' &= b_0b, & \phi' &= (\Delta\phi)\phi. \end{aligned} \quad (3.19)$$

Here the non-primed variables are the lubrication type variables.  $x$  and  $y$  are the horizontal and vertical coordinates respectively,  $h$  is the free surface elevation,  $u$  and  $v$  are the horizontal and vertical velocity components,  $b$  is the perpendicular component of the magnetic field and  $\phi$  the electric potential.  $b_0$  is the magnetic field strength in the centre of the cavity ( $x = 0$ ) and the characteristic velocity  $u^*$  is defined as

$$u^* = \frac{\sigma \Delta \phi b_0 \alpha d}{\rho \nu} A, \quad (3.20)$$

which follows from the balance between viscous and Lorentz forces.

The system is in a steady, two-dimensional motion. In lubrication variables the conservation equations reduce to:

$$u_x + v_y = 0, \quad (3.21)$$

$$\begin{aligned} Re A^2 (uu_x + vv_y) &= -Ap_x + A^3 u_{xx} + Au_{yy} \\ &\quad - \frac{1}{\alpha} (\phi_y + Ha^2 Aub) b, \end{aligned} \quad (3.22)$$

$$\begin{aligned} Re A^3 (uv_x + vv_y) &= -p_y + A^4 v_{xx} + A^2 v_{yy} \\ &\quad + A \frac{1}{\alpha} (\phi_x - Ha^2 Avb) b - A \frac{Bo}{Ca}, \end{aligned} \quad (3.23)$$

$$A^2 \phi_{xx} + \phi_{yy} = Ha^2 [A^3 (vb)_x - A(ub)_y]. \quad (3.24)$$

The subscripts denote derivatives with respect to the coordinate in the subscript.

In this context, the Reynolds number,  $Re$ , the Hartmann number,  $Ha$ , the Bond number,  $Bo$  and the capillary number  $Ca$ , are defined as

$$Re = \frac{u^* d}{\nu}, \quad Ha^2 = \frac{\sigma b_0^2 d^2 \alpha}{\rho \nu}, \quad Bo = \frac{\rho g d^2}{\gamma}, \quad Ca = \frac{\rho \nu u^*}{\gamma}. \quad (3.25)$$

In order to eliminate the pressure from the conservation equations, we introduce the stream function  $\psi$ , which obeys the continuity equation (Equation 3.21)

$$u = \psi_y, \quad v = -\psi_x, \quad (3.26)$$

such that a single equation in  $\psi$  remains instead of equations for the horizontal and vertical momentum (Equations 3.22 and 3.23):

$$\begin{aligned} & ReA^2 [\psi_y \psi_{xyy} - \psi_x \psi_{yyy} - A^2 (\psi_x \psi_{xxy} - \psi_y \psi_{xx})] \\ & = A\psi_{yyy} + 2A^3\psi_{xyy} + A^5\psi_{xxx} \quad (3.27) \\ & - \frac{1}{\alpha} [\phi_{yy}b + A^2 (\phi_{xx}b + \phi_x b_x) + Ha^2 A (\psi_{yy}b^2 + A^2\psi_{xx}b^2 + 2A^2\psi_x b b_x)], \end{aligned}$$

and for the charge conservation equation

$$A^2\phi_{xx} + \phi_{yy} = -Ha^2 (A^3\psi_{xx}b + A^3\psi_x b_x + A\psi_{yy}b). \quad (3.28)$$

The boundary conditions at the wall are straightforwardly transformed, while the free surface boundary conditions are respectively transformed to

$$u'h'_{x'} = v', \quad (3.29)$$

$$2A^2h'_{x'}(v'_{y'} - u'_{x'}) + (1 - A^2h'^2_{x'})(u'_{y'} + A^2v'_{x'}) = 0, \quad (3.30)$$

$$Ca^{-1}A^3h'_{x'}(1 + A^2h'^2_{x'})^{-3/2} = -p + 2A^2(1 + A^2h'^2_{x'})^{-1} \quad (3.31)$$

$$[v'_{y'} - h'_{x'}u'_{y'} + A^2h'_{x'}(-v'_{x'} + h'_{x'}u'_{x'})],$$

$$A^2\phi'_{x'}h'_{x'} - \phi'_{y'} = (Au' + A^3h'_{x'}v')b', \quad (3.32)$$

where a third dimensionless group,  $Ca$ , the capillary number, is introduced

$$Ca = \frac{\mu u^*}{\gamma}. \quad (3.33)$$

The modified pressure  $p_m$  is introduced to eliminate the hydrostatic pressure from the Navier-Stokes equation (Equation 3.23), such that

$$p_m = p + A\frac{Bo}{Ca}(y - 1), \quad (3.34)$$

and the boundary condition from Equation 3.31, results in

$$\begin{aligned} A^3h_{xx}(1 + A^2h_x^2)^{-3/2} &= -Ca p_m + ABo(h - 1) + 2A^2(1 + A^2h_x^2)^{-1} \\ & [-\psi_{xy} - h_x\psi_{yy} + A^2h_x(\psi_{xx} + h_x\psi_{xy})], \end{aligned} \quad (3.35)$$

### 3.2.4 Core flow

The system of four equations is now reduced to a set of two equations with the stream function  $\psi$  and the electric potential  $\phi$  as unknowns. We will be looking for a solution where the flow

is in the  $x$ -direction only in the lowest order near  $x = 0$ . To obtain the expression that is valid in the region far away from the wall, the stream function will be expanded as

$$\psi = \sum_{n=0}^{\infty} A^n \psi_n(x, y), \quad (3.36)$$

where a similar expansion can be used for the pressure  $p$ , the electric potential  $\phi$  and the interface deformation  $h(x) = \sum_{n=0}^{\infty} A^n h_n(x)$ , where  $h_0 = 1$  is the undisturbed interface.

For the dimensionless parameters we will use the following asymptotic limits

$$Re = \overline{Re}A, \quad Ha^2 = \overline{Ha}^2, \quad (3.37)$$

where  $\overline{Re}$  and  $\overline{Ha}^2$  are both of order  $O(1)$ . The presented solution strategies will be valid for  $Re \leq O(A)$  and  $Ha^2 \leq O(1)$ .

To obtain the equation for the lowest order stream function  $\psi_0$ , the assumptions in Equations 3.36 and 3.37 are substituted in Equations 3.32 and 3.27. By collecting all the terms in the same  $n$ -th order in  $A$ , the equations for  $\psi_n$  and  $\phi_n$  can be obtained to arbitrarily order. This will give us

$$\psi_{0yyyy} = \frac{1}{\alpha} \left( \phi_{1yy}b + \overline{Ha}^2 \psi_{0yy}b^2 \right), \quad \phi_{1yy} + \overline{Ha}^2 \psi_{0yy}b = 0. \quad (3.38)$$

It should be noted that the lowest order equation for the stream function contains higher order terms of the electric potential, which can be eliminated by means of the higher order equations of the electric potential, thus:

$$\psi_{0yyyy} = 0, \quad \phi_{0yy} = 0. \quad (3.39)$$

The boundary conditions

$$\left. \begin{array}{l} \psi_0 = \psi_{0y} = \phi_{0y} = 0 \quad \text{on } y = 0, \\ \psi_0 = \psi_{0yy} = \phi_{0y} = 0 \\ h_{1xx} = -\overline{Ca}p_{m0} + \overline{Bo}h_1 \quad \text{on } y = 1 + Ah_1, \end{array} \right\} \quad (3.40)$$

are obtained from no-slip and electrically insulating conditions, Equation 3.16 and by substituting the asymptotic expansions for the free surface, where the following asymptotic limit is used (with  $\overline{Ca} = O(1)$ ):

$$Ca = \overline{Ca}A^4, \quad Bo = \overline{Bo}A^2, \quad (3.41)$$

thus  $Ca = O(A^4)$  and  $Bo = O(A^2)$ . However, the derivation is also valid for  $Ca \leq A^4$ .  $Bo$  can appear in the equations to any order, as it is competing with surface tension as the restoring force. Using these assumptions, the surface tension and gravity force will turn out to first act at the same order of magnitude of the asymptotic expansions. For smaller  $Bo$ , surface tension dominates the restoring force, while for larger Bond number gravity will dominate as a restoring force.



For  $\psi_0$  we will get  $\psi_0 = 0$ , while for the solution of the lowest order electric potential, it can be seen that the solution  $\phi_0 = x$  satisfies the Poisson equation for the electric potential as well as the boundary conditions at the outer walls, the bottom wall and the free surface. It follows that  $p_0 = 0$  and thus  $h_1 = 0$

This result has implications for the limiting case  $A = 0$ . In the case of an infinitely wide or very thin layer, the zeroth order solution will be the only term remaining, as all terms of  $O(A)$  and higher vanish. Thus, in this case, the electromagnetic forces will not cause flow in the domain. In this paper we study bounded domains with  $0 < A \ll 1$ , such that higher order terms should be included. Progressing to the first order solution, we obtain

$$\psi_{1yyyy} = \frac{1}{\alpha} \left( \phi_{2yy}b + \overline{Ha}^2 \psi_{1yy}b^2 + \phi_{0xx}b + \phi_{0x}b_x \right), \quad (3.42)$$

$$\phi_{0xx} + \phi_{2yy} = -\overline{Ha}^2 \psi_{1yy}b, \quad (3.43)$$

which, with known  $b$  and  $\phi_0$ , simplifies to

$$\psi_{1yyyy} = \frac{1}{\alpha} \phi_{0x}b_x = -1. \quad (3.44)$$

Subject to the boundary conditions at the bottom wall and top free surface (Equations 3.29-3.32)

$$\left. \begin{array}{l} \psi_1 = \psi_{1y} = 0 \quad \text{on} \quad y = 0, \\ \psi_1 = \psi_{1yy} = 0 \quad \text{on} \quad y = 1 + Ah_1 + A^2h_2, \end{array} \right\} \quad (3.45)$$

this gives

$$\psi_1(x, y) = -\frac{1}{48}y^2(2y^2 - 5y + 3). \quad (3.46)$$

Reintroducing the pressure by means of Equations 3.22 and 3.23 allows to solve for the pressure, which reads

$$p_{m1} = -\frac{1 + \alpha x}{\alpha} \left( y - \frac{5}{8} \right) + p_{ref}, \quad (3.47)$$

where  $p_{ref}$  is the reference pressure.

The boundary condition at  $y = 1 + Ah_1(x) + A^2h_2(x)$ , based on the modified pressure  $p_{m1}$  reads, where  $p_{ref}$  is eliminated in favor of a different integration constant,

$$h_{2xxx} = -\overline{Ca}p_{m1x} + \overline{Bo}h_{2x}, \quad (3.48)$$

$$h_{2xxx} = \frac{3}{8}\overline{Ca} + \overline{Bo}h_{2x}. \quad (3.49)$$

This third order differential equation in  $h_2$ , gives the general solution

$$h_2(x) = \frac{1}{\sqrt{\overline{Bo}}} \left( \lambda_1 e^{\sqrt{\overline{Bo}}x} + \lambda_2 e^{-\sqrt{\overline{Bo}}x} \right) - \frac{3\overline{Ca}}{8\overline{Bo}}x + \lambda_3, \quad (3.50)$$

with  $\lambda_1$ ,  $\lambda_2$  and  $\lambda_3$  constants that will follow from the matching condition with the boundary layer flow and the other constraints.

### 3.2.5 End wall flow

It follows from Equation 3.46 that the flow in the central part of the domain is strictly horizontal ( $v = 0$ ). This core flow solution breaks down near vertical side walls, where the liquid has to change direction. To study this boundary layer behaviour, the stretching coordinates  $\xi$  and  $\eta$  are introduced as

$$\xi = \frac{x + \frac{1}{2}}{A^\nu}, \eta = y. \quad (3.51)$$

The origin of this coordinate system is located in the lower left corner of the shallow cavity. It can easily be verified that for the derivative of an arbitrary function  $f$ ,  $f_y = f_\eta$  and  $f_x = A^{-\nu} f_\xi$ . Using this in Equation 3.27, results in

$$\begin{aligned} & ReA^{2-\nu} (\psi_\eta \psi_{\xi\eta\eta} - \psi_\xi \psi_{\eta\eta\eta} - A^{2-3\nu} (\psi_\xi \psi_{\xi\xi\eta} - \psi_\eta \psi_{\xi\xi\xi})) \\ &= A\psi_{\eta\eta\eta} + 2A^{3-2\nu} \psi_{\xi\xi\eta} + A^{5-4\nu} \psi_{\xi\xi\xi} \\ &\quad - \frac{1}{\alpha} [\phi_{\eta\eta} b + A^{2-2\nu} (\phi_{\xi\xi} b + \phi_\xi b_\xi)] + \\ & Ha^2 (A(b^2 \psi_{\eta\eta}) + A^{3-2\nu} (b_\xi \psi_{\xi\xi} b + b^2 \psi_{\xi\xi} + b \psi_\xi b_\xi)). \end{aligned} \quad (3.52)$$

It follows that there is a significant degeneration for  $\nu = 1$ , such that  $\xi = A^{-1}(x + \frac{1}{2})$ . Variables in terms of the stretched coordinates, thus the side wall solution, will be denoted by a " $\tilde{\cdot}$ ". The magnetic field  $b = -(1 + \alpha x)$  is then expressed as  $\tilde{b} = (-1 + \frac{1}{2}\alpha) - A\alpha\xi = \tilde{b}_0 + A\tilde{b}_1$  and the equation for the stream function becomes

$$\begin{aligned} & \overline{Re}A^2 (\tilde{\psi}_y \tilde{\psi}_{\xi y y} - \tilde{\psi}_\xi \tilde{\psi}_{y y y} - \tilde{\psi}_\xi \tilde{\psi}_{\xi\xi y} + \tilde{\psi}_y \tilde{\psi}_{\xi\xi\xi}) \\ &= A\nabla^4 \tilde{\psi} - \frac{1}{\alpha} [\tilde{b}\nabla^2 \tilde{\phi} + \tilde{b}_\xi \tilde{\phi}_\xi + \overline{Ha}^2 A (\tilde{b}^2 \nabla^2 \tilde{\psi} + 2\tilde{\psi}_\xi \tilde{b} \tilde{b}_\xi)], \end{aligned} \quad (3.53)$$

where the  $\nabla$  operator is defined in terms of the stretched coordinates  $\xi$  and  $\eta$ , giving the Laplacian operator  $\nabla^2 = \frac{\partial^2}{\partial \xi^2} + \frac{\partial^2}{\partial \eta^2}$  and the biharmonic operator  $\nabla^4 = \frac{\partial^2}{\partial \xi^4} + 2\frac{\partial^2}{\partial \xi^2 \partial \eta^2} + \frac{\partial^2}{\partial \eta^4}$ . The conservation of current evolves, as a result of stretching, into

$$\nabla^2 \tilde{\phi} = -\overline{Ha}^2_\alpha A (\tilde{b}\nabla^2 \tilde{\psi} + \tilde{b}_\xi \tilde{\psi}_\xi). \quad (3.54)$$

Expanding the side wall stream function  $\tilde{\psi}$  similar to the core flow  $\psi$

$$\tilde{\psi} = \sum_{n=0}^{\infty} A^n \tilde{\psi}_n(x, y), \quad (3.55)$$

leads to an equation for the leading order stream function in the left wall boundary layer  $\tilde{\psi}_0$

$$\nabla^4 \tilde{\psi}_0 = \frac{1}{\alpha} \left[ \tilde{b}_0 \nabla^2 \tilde{\phi}_1 + \tilde{b}_1 \nabla^2 \tilde{\phi}_0 + \tilde{b}_{1\xi} \tilde{\phi}_{0\xi} + \tilde{b}_{0\xi} \tilde{\phi}_{1\xi} + \overline{Ha^2} \left( \tilde{b}_0^2 \nabla^2 \tilde{\psi}_0 + 2\tilde{b}_0 \tilde{b}_{0\xi} \tilde{\psi}_{0\xi} \right) \right]. \quad (3.56)$$

Simultaneously we obtain from the charge conservation equation

$$\nabla^2 \tilde{\phi}_0 = 0, \quad (3.57)$$

$$\nabla^2 \tilde{\phi}_1 = -\overline{Ha^2} \left( \tilde{b}_0 \nabla^2 \tilde{\psi}_0 + \tilde{b}_{0\xi} \tilde{\psi}_{0\xi} \right), \quad (3.58)$$

which, together with  $\tilde{b}_{0\xi} = 0$ , reduces Equation 3.56 to

$$\nabla^4 \tilde{\psi}_0 = 0. \quad (3.59)$$

This has the solution  $\tilde{\psi}_0 = 0$ , which agrees with the observation for the core flow. When the contact angle boundary condition is limited to

$$\tan(\theta - \frac{1}{2}\pi) = mA^2, \quad (3.60)$$

where  $m \leq O(1)$  is a measure for the contact angle. The boundary condition for the free surface gives  $\tilde{h}_{1\xi\xi} = 0$  and  $\tilde{h}_{1\xi}(0) = 0$ . Thus, for the free surface deformation it is obtained that  $\tilde{h}_1 = 0$ .

It is observed that  $\phi = x$  relates to  $\tilde{\phi}_0 = -\frac{1}{2}$  and  $\tilde{\phi}_1 = \xi$ , which is satisfying the above problem. Using  $\tilde{\psi}_0 = 0$ , the first order stream function  $\tilde{\psi}_1$  obeys

$$\nabla^4 \tilde{\psi}_1 = \frac{1}{\alpha} \left[ \tilde{b}_0 \nabla^2 \tilde{\phi}_2 + \tilde{b}_1 \nabla^2 \tilde{\phi}_1 + \tilde{b}_{1\xi} \tilde{\phi}_{1\xi} + \tilde{b}_{0\xi} \tilde{\phi}_{2\xi} + \overline{Ha^2} \left( 2\tilde{b}_0 \tilde{b}_1 \nabla^2 \tilde{\psi}_0 + \tilde{b}_0^2 \nabla^2 \tilde{\psi}_1 \right) \right]. \quad (3.61)$$

Reducing this with relation  $\nabla^2 \tilde{\phi}_2 = -\overline{Ha^2} \left( \tilde{b}_1 \nabla^2 \tilde{\psi}_0 + \tilde{b}_0 \nabla^2 \tilde{\psi}_1 \right)$  from charge conservation results in

$$\nabla^4 \tilde{\psi}_1 = \frac{1}{\alpha} \tilde{b}_{1\xi} \tilde{\phi}_{1\xi} = -1, \quad (3.62)$$

which ultimately describes the change of flow direction in the boundary layer flow near the left wall.

The walls at the side and bottom are no-slip, meaning  $\tilde{\psi}_1 = \tilde{\psi}_{1y} = 0$  at the bottom and  $\tilde{\psi}_1 = \tilde{\psi}_{1\xi} = 0$  at the left wall. For the free surface  $\tilde{\psi}_1 = 0$  (from Equation 3.16),  $\tilde{\psi}_{1\xi} = 0$  (from Equation 3.5) and  $\tilde{\psi}_{1yy} - \tilde{\psi}_{1\xi\xi} = 0$  (from Equations 3.12, 3.13 and 3.15), effectively reducing at this order to  $\tilde{\psi}_1 = \tilde{\psi}_{1yy} = 0$ . The solution for  $\xi \rightarrow \infty$  should match with the core flow solution (Equation 3.46).

The derivation for the right wall flow can be obtained following the exact same arguments, but with the stretching coordinate  $\zeta = A^{-1}(\frac{1}{2} - x)$ , and leads to the same results as the left wall. This will not be repeated here.

A final boundary condition for the top surface is obtained from Equation 3.31

$$\tilde{h}_{2\xi\xi} = 0, \quad (3.63)$$

Combining this with the contact angle boundary condition 3.18,  $\tilde{h}_{2\xi} = m$  (and similarly for the right wall) and the volume conserving property (Equation 3.17), this leads to a closed expression for the free surface elevation that is valid over the full width of the liquid layer:

$$h_2(x) = \frac{1}{\sqrt{Bo}} \left[ \frac{3Ca}{8Bo} \frac{\sinh(\sqrt{Bo}x)}{\cosh(\frac{1}{2}\sqrt{Bo})} - m \frac{\cosh(\sqrt{Bo}x)}{\sinh(\frac{1}{2}\sqrt{Bo})} \right] - \frac{3Ca}{8Bo}x + \frac{2m}{Bo}, \quad (3.64)$$

From Equation 3.46 we see that the flow strength scales with a single dimensionless parameter,  $\alpha$ , while the free surface elevation depends on  $Ca$  and  $Bo$  as well. This has as an interesting consequence that, for example, the velocities in the liquid layer can be increased at fixed free surface elevation, or vice versa.

In the absence of gravity, e.g.  $Bo = 0$ , Equation 3.49 would simplify to  $h_{2xxx} = 3/8Ca$ , with solution

$$h_2 = \frac{1}{16}Ca \left( x^3 - \frac{3}{4}x \right) - m \left( x^2 - \frac{1}{12} \right), \quad (3.65)$$

which is consistent with Equation 3.64, in the limit for  $Bo \rightarrow 0$ . For decreasing influence of surface tension, in other words, for increasing  $Ca$ , the linear term in Equation 3.64 will become dominant. However, the limit  $Ca \rightarrow \infty$  does not exist, as close enough to the side walls, surface tension is always significant.

Reducing Equation 3.65 to units carrying a dimension, gives

$$\Delta h' = A^2 dh_2 = \frac{Cad\alpha}{16A^2} \left( \frac{x'^3}{l^3} - \frac{3x'}{4l} \right) = \frac{\sigma\Delta\phi b_0 dl\alpha}{\gamma} \left( \frac{x'^3}{l^3} - \frac{3x'}{4l} \right), \quad (3.66)$$

The horizontal velocity profile in dimensioned variables, follows from the stream function for the core flow (Equation 3.46):

$$u'(y') = -\frac{1}{48}Au^* \left( 8\frac{y'^3}{d^3} - 15\frac{y'^2}{d^2} + 6\frac{y'}{d} \right). \quad (3.67)$$

### 3.2.6 Analytic solution for the end wall flow

The flow in the side wall is described by the biharmonic Equation 3.62

$$\nabla^4 \tilde{\psi}_1 = -1. \quad (3.68)$$

With boundary conditions

$$\left. \begin{aligned} \tilde{\psi}_1 = 0, \tilde{\psi}_{1\eta} = 0 & \quad \text{on } \eta = 0 \\ \tilde{\psi}_1 = 0, \tilde{\psi}_{1\eta\eta} - \tilde{\psi}_1\xi\xi = 0, \tilde{\psi}_\xi = 0 & \quad \text{on } \eta = 1 \\ \tilde{\psi}_1 = 0, \tilde{\psi}_{1\xi} = 0 & \quad \text{on } \xi = 0 \\ \tilde{\psi}_1 = \psi_1(\eta), \tilde{\psi}_{1\xi} = 0 & \quad \text{for } \xi \rightarrow \infty. \end{aligned} \right\} \quad (3.69)$$

We will now apply the transformation

$$\chi(x, y) = \tilde{\psi}_1 - \psi_1(y). \quad (3.70)$$

For clarity and staying in line with literature notation, we will now use  $x, y$  instead of  $\xi, \eta$  and reduce the boundary conditions to:

$$\left. \begin{aligned} \chi = 0, \chi_y = 0 & \quad \text{on } y = 0 \\ \chi = 0, \chi_{yy} = 0 & \quad \text{on } y = 1 \\ \chi = f(y) = -\psi_1(y), \chi_x = 0 & \quad \text{on } x = 0 \\ \chi = 0, \chi_x = 0 & \quad \text{for } x \rightarrow \infty. \end{aligned} \right\} \quad (3.71)$$

The solution to Equation 3.70 can be found using the Laplace transform:

$$f(p, y) = \mathcal{L}[\chi(x, y)] = \int_0^\infty \chi(x, y) e^{-px} dx, \quad (3.72)$$

As a first step, Equation 3.70 is Laplace transformed

$$\begin{aligned} \mathcal{L}[\nabla^4 \chi] &= \frac{\partial^4 f}{\partial y^4} + 2p^2 \frac{\partial^2 f}{\partial y^2} + p^4 f = p^3 \chi(0, y) \\ &+ \cancel{p^2 \chi_x(0, y)} + p \chi_{xx}(0, y) + \chi_{xxx}(0, y) + 2 \left[ p \frac{\partial^2 \chi}{\partial y^2}(0, y) + \frac{\partial^2 \chi_x}{\partial y^2}(0, y) \right] 0. \end{aligned} \quad (3.73)$$

This reduces the differential equation in coordinates  $x$  and  $y$  to a differential equation in  $y$  only. At  $x = 0$  additional boundary conditions on  $\chi_{xx}$  and  $\chi_{xxx}$  are required by the above formula.  $\chi(0, y)$  is expanded in a sine series as follows

$$\chi(0, y) = \sum_{n=1}^{\infty} b_n \sin(n\pi y) \quad \text{with } b_n = 2 \int_0^1 \chi(0, y) \sin(n\pi y) dy \quad (3.74)$$

The unknown functions  $\chi_{xx}$  and  $\chi_{xxx}$  are expanded by the same means, thus

$$\frac{\partial^2 \chi}{\partial x^2}(0, y) = \sum_{n=1}^{\infty} c_n \sin(n\pi y) \quad \frac{\partial^3 \chi}{\partial x^3}(0, y) = \sum_{n=1}^{\infty} d_n \sin(n\pi y), \quad (3.75)$$

however, the coefficients  $c_n$  and  $d_n$  can not be determined at this point.

The ordinary differential equation for the function  $f(p, y)$  now becomes

$$\frac{\partial^4 f}{\partial y^4} + 2p^2 \frac{\partial^2 f}{\partial y^2} + p^4 f = \sum_{n=1}^{\infty} \beta_n(p) \sin(n\pi y) \quad (3.76)$$

$$\beta_n(p) = \frac{(p^3 - 2pn^2\pi^2) b_n + pc_n + d_n}{(p^2 - n^2\pi^2)^2}. \quad (3.77)$$

The general solution of this differential equation is

$$f(p, y) = K_1 \sin(py) + K_2 \cos(py) + K_3 y \sin(py) + K_4 y \cos(py) + \sum \beta_n(p) \sin(n\pi y). \quad (3.78)$$

The four boundary conditions on the two boundaries for  $y$  provide the integration constants  $K_i$

$$K_1 = \sum_n -\beta_n(p) \frac{n\pi}{p - \cos p \sin p} \quad (3.79)$$

$$K_2 = 0 \quad (3.80)$$

$$K_3 = \sum_n \beta_n(p) \sin^2 p \frac{n\pi}{p - \cos p \sin p} \quad (3.81)$$

$$K_4 = \sum_n \beta_n(p) \sin p \cos p \frac{n\pi}{p - \cos p \sin p} \quad (3.82)$$

$$(3.83)$$

And thus

$$f(p, y) = \sum_n \beta_n(p) \left[ \sin(n\pi y) + \frac{n\pi}{p - \cos p \sin p} (-\sin(py) + \sin^2 p \sin(py)y + \sin p \cos p \cos(py)y) \right] \quad (3.84)$$

The inverse Laplace transform will in principle provide the stream function  $\chi$ . It should however be noted that the coefficient  $\beta_n$  still contains unknowns  $c_n$  and  $d_n$ . The inverse Laplace transform and the unknown coefficients can be found in the same solution step, using complex analysis. The steps follow the procedure by Benthem<sup>3</sup> and is schematically summarized in figure 3.4.

The inverse Laplace transformation is given by the Bromwich integral (see Kwok<sup>20</sup> and Duffy<sup>10</sup> p61):

$$\chi(x, y) = \frac{1}{2\pi i} \lim_{R \rightarrow \infty} \int_{a-iR}^{a+iR} f(p, y) e^{px} dp \quad (3.85)$$

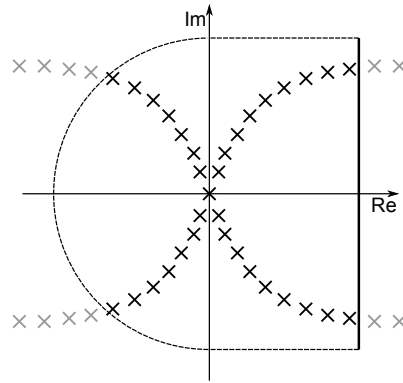


**Figure 3.4** The inverse Laplace transform is provided by the integral along the solid line. The path integral is closed by adding the dashed, semi-circle, which integral is zero by Jordan's lemma. The residue theorem gives the integral for the poles (dark crosses) inside the closed path.

where  $a > 0$ . The contour integral can be closed with the left semi-circle, and by application of Jordan's lemma, this gives:

$$\chi(x, y) = \frac{1}{2\pi i} \oint_C f(p, y) e^{px} dp \quad (3.86)$$

The integral can be evaluated by applying the Cauchy residue theorem

$$\chi(x, y) = \sum_k \text{Res}(f(p_k, y)), \quad (3.87)$$

where the summation is over the poles of  $f(p, y)$  inside the closed contour. It is observed that the first pole is  $p = 0$  and the subsequent poles are solutions of  $p - \cos p \sin p = 0$  (or  $2p - \sin 2p = 0$ ).

$2p - \sin(2p) = 0$  has infinitely many complex solutions, which we will find numerically. Therefore we will truncate the above infinite sums after the first  $P$  terms. There, we need to find the poles inside the closed loop and thus the poles closest to the origin. To find the poles of  $2p - \sin(2p) = 0$  we will combine the search algorithm outlined by Meylan and Gross<sup>22</sup> with knowledge about the equation.

The algorithm is based on the fact that the anti-clockwise integral of the variation of the argument along a closed loop is a measure for the amount of poles inside this closed loop. The brute force algorithm is based on performing the closed loop integral on boxes and refining the boxes until only one pole is counted inside. Newton's method will then be used to find a pole. If the starting point is outside the basin of attraction of the pole, another refinement step will be performed. Applying the brute force method on the current problem is rather expensive. The brute force method will be applied on a significantly reduced subset of the complex numbers

- If  $p$  is a pole, then are  $p^*$ ,  $-p$  and  $-p^*$  also poles of the equation. In other words, finding the poles in the first quadrant is sufficient.
- Writing  $p = x + iy$ , we obtain

$$x = \sin x \cosh y, \quad (3.88)$$

$$y = \cos x \sinh y. \quad (3.89)$$

Which can be reduced to  $x^2 = \cosh^2 y - y^2 \coth^2 y$ , which is a monotonically increasing function. In other words, if we find the pole in the first quadrant closest to the origin, we know that each subsequent pole in the first quadrant has a larger real and imaginary part than the current pole.

Using this algorithm, as many poles as desired can be found, while the found poles are also the ones closest to the origin, which is necessary for the intended inverse Laplace transform. In order to find the Laplace transform, we apply the residue theorem. The residue at  $p = 0$  is 0, which follows from

$$\text{Res}(f(0, y)) = \lim_{p \rightarrow 0} pf(p, y) = 0. \quad (3.90)$$

The residues at the other poles are depending on the unknown coefficients  $c_n$  and  $d_n$ . To calculate the unknown quantity, we make us of

$$\text{Res}\left(\frac{g(p)}{h(p)}\right) = \frac{g(p)}{h'(p)}. \quad (3.91)$$

For this problem,  $h(p) = p - \sin p \cos p$  and  $h'(p) = 2 \sin^2 p$  can be used. With the numerically obtained poles and the above method for calculating the residue at pole  $p_k$ , we find, when including all prefactors

$$\text{Res}(f(p_k, y)) = F(p_k, y) \sum_{n=1}^{\infty} n\pi \beta_n(p) \quad (3.92)$$

with

$$F(p_k, y) = \frac{-\sin(p_k y) + \sin^2 p_k \sin(p_k y)y + \sin p_k \cos p_k \cos(p_k y)y}{2 \sin^2 p_k}. \quad (3.93)$$

The coefficient  $c_n$  and  $d_n$  are still undetermined, but we will choose them such, that the residues for the poles with  $\text{Re}(p_k) > 0$  vanish for arbitrary  $y$ , in other words, for the specific pole  $p_k$ , this requires

$$\sum_{n=1}^P n\pi \frac{(p_k^3 - p_k n^2 \pi^2) b_n + p_k c_n + d_n}{(p_k^2 - n^2 \pi^2)^2} = 0, \quad (3.94)$$

where the infinite sum is truncated after the first  $P$  terms. Considering the first  $P$  poles in the first quadrant and obtaining the  $P$  in the fourth quadrant for free, this gives a set of  $2P$



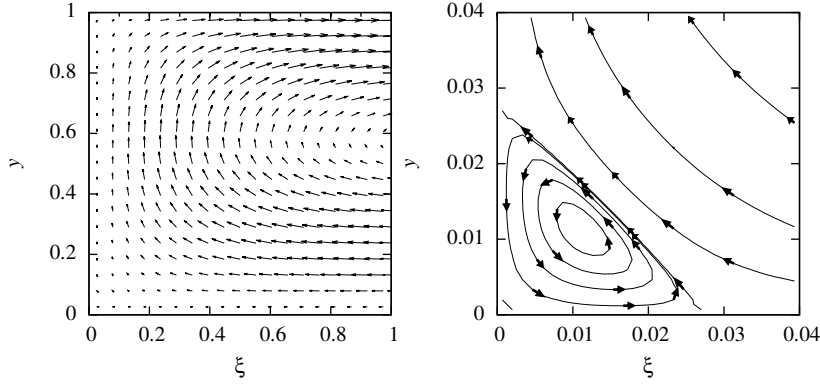


**Figure 3.5** The velocity vector plot (left) in the left side wall region is depicted, which is derived from the side wall stream function (Equation 3.95) for  $P = 2048$ . The flow is turning clockwise, while the velocity at the left and bottom boundary is zero and the top boundary is a free surface. The streamline plot (right) is determined for  $P = 8192$  shows isocontours of the stream function in the region of the lower left corner of the domain, demonstrating the existence of a counter-rotating eddy in the corner.

equations in  $2P$  unknowns. In matrix notation this results in a full matrix of  $(2P)^2$  complex components, which can be solved for  $c_n$  and  $d_n$  by Gauss elimination.

When the poles  $p_k$  and coefficients  $c_n$  and  $d_n$  are known, Equation 3.87 provides the solution to the problem.

$$\chi(x, y) = \sum_{k=1}^{2P} \sum_{n=1}^P n\pi\beta_n(-p_k)F(-p_k, y)e^{-p_k x}, \quad (3.95)$$

which can straightforwardly be transformed back to the streamfunction  $\tilde{\psi}_1$ . It should be noted that, the Gauss elimination is an  $O(P^3)$  algorithm, while the calculation of  $\tilde{\psi}_1$  is in principle  $O(P^2)$ , the prefactor for the latter calculation is rather large, based on the amount of operations and the fact that is operated on a grid looping over  $x$  and  $y$ .

Figure 3.5 shows the currently obtained velocity field for  $P = 2048$  and streamlines in the region close to the corner for  $P = 8192$ . A counter-rotating eddy was found close to the corner, as was predicted by Moffatt<sup>23</sup>. Such a counter-rotating eddy was not found in the corner near the free surface.

Figure 3.6 shows the velocity magnitude along the line  $\xi = y$ , where a different number of poles are included to calculate the stream function. It shows the convergence of the velocity magnitude with an increasing number of poles. It can be seen that increasing the amount of poles above 4 does not change the velocity profile beyond a distance of 0.1 from the corner, while  $P = 1024$  and  $P = 8192$  are enough for an accurate velocity profile beyond a distance of 0.01 and 0.002 respectively.

The minimum in this velocity profile is related to the centre of the eddy. Increasing the

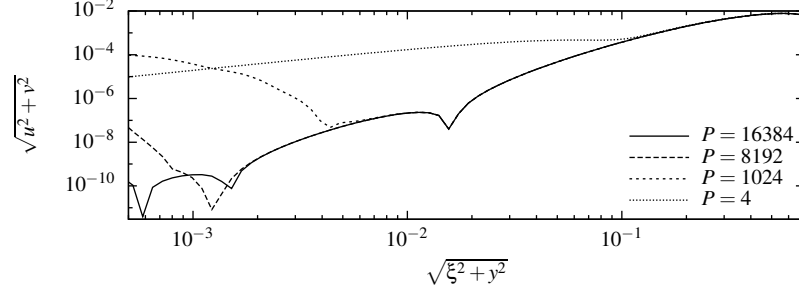


**Figure 3.6** The velocity magnitude along the line  $\xi = y$  in Figure 3.5, which shows the effect of increasing the amount of poles (see Equation 3.95) on the velocity magnitude for  $P = 4$ ,  $P = 1024$ ,  $P = 8192$  and  $P = 16384$ .

number of poles reveals a secondary minimum, which is an indication for the second eddy of the infinite series of eddies in the corner, as predicted by Moffatt<sup>23</sup>.

### 3.2.7 Increased magnetic interaction

In the derivation of the free surface elevation (Equation 3.64), it was found that for the Hartmann number  $Ha = O(1)$ , only  $O(A)$  flow is present. Suppose the square of the Hartmann number increases by an order in  $A$ , thus  $Ha^2 = \overline{Ha^2} A^{-1}$ . For this higher Hartmann number, it can be shown that, again,  $\psi_0 = 0$  and the core flow  $\psi_1$ , can be solved by

$$\psi_{1yyyy} = -1, \quad \psi_1 = -\frac{1}{48}y^2(2y^2 - 5y + 3), \quad (3.96)$$

which would result in the general solution for  $h_2$  as given by Equation 3.50.

For the side wall solution, again  $\tilde{\psi}_0 = 0$  is found, however, at higher order

$$\nabla^4 \tilde{\psi}_1 = \frac{1}{\alpha} \left( \phi_{1\xi} \tilde{b}_{1\xi} + \overline{Ha^2} \alpha \tilde{\psi}_{1\xi} \tilde{b}_0 \tilde{b}_{1\xi} \right) = -1 - \left( \frac{1}{2}\alpha - 1 \right) \overline{Ha^2} \alpha \tilde{\psi}_{1\xi}. \quad (3.97)$$

which means that the analytical side wall solution from Section 3.2.5 is no longer valid for  $Ha^2 = O(A^{-1})$ .

For  $Ha^2 = O(A^{-2})$ , the primary flow in the core region will no longer be one-dimensional, as the equation for the core flow would read

$$\psi_{0yyyy} = \frac{1}{\alpha} \overline{Ha^2} \psi_{0x} b b_x = \overline{Ha^2} (1 + \alpha x) \psi_{0x}. \quad (3.98)$$

### 3.3 Numerical modeling

The analytic solution to the liquid layer problem with a Lorentz force will be compared with numerical solutions obtained from two different methods for evaluating free surface flows. The first method is the moving mesh interface tracking (MMIT) method, where the mesh aligns with the free surface. The second method is the volume of fluid (VOF) method, where the free surface is tracked with a transport equation for the liquid fraction.

The numerical simulations are performed using the standard<sup>31</sup> and extended<sup>34</sup> OpenFOAM software. Available solvers were extended with the one-way coupled MHD equations for both methods, respectively *interTrackFoam* of distribution *1.6 extend* and *interFoam* of distribution *2.1*.

#### 3.3.1 Moving mesh interface tracking method

The moving mesh interface tracking method is based on aligning a boundary of the numerical mesh with the free surface. This results in a sharp interface by definition and allows for the implementation of exact boundary conditions at the interface. The approach as proposed by Muzaferija and Perić<sup>24</sup> and the implementation by Tuković and Jasak<sup>35</sup> was used.

The moving mesh interface tracking method introduces, in addition to continuity and momentum equations, the so called space conservation law, i.e.

$$\frac{d}{dt'} \int_{V'} dV' - \int_{S'} \hat{\mathbf{n}} \cdot \mathbf{v}_s' dS' = 0 \quad (3.99)$$

where  $\mathbf{v}_s'$  is the velocity of the surface. This velocity of the surface of an arbitrary control volume  $V'$  has to be accounted for in the integrated mass and momentum conservation equations.<sup>24,35</sup>

The boundary conditions from Section 3.2.2 do also apply for the numerical simulations, e.g. no mass should cross the boundary and the stresses at opposite sides of the interface should match. Non-zero mass fluxes through the free surface are corrected by moving the boundary. This correction is used as a boundary condition in the Laplace equation for moving the interior points in the domain by an amount  $\mathbf{d}'$ :

$$\nabla' \Gamma \cdot \nabla' \mathbf{d}' = 0 \quad (3.100)$$

where  $\Gamma$  is a diffusion parameter that is inversely proportional to the square of the distance to the free surface.

#### Details of the numerical simulation

The simulations were performed on an initially square cell grid containing  $20N \times N$  cells, representing the bottom layer only, with  $A = 0.05$  and  $Re = A$ ,  $Ha = 1$ ,  $Ca = A^4$

and  $Bo = A^2$ . Figure 3.7(top) shows the vertical velocity component along a horizontal line  $y = 0.5$  for various  $N$ . The difference in maximum velocity obtained on a mesh with  $N = 20$ , compared to  $N = 10$  and  $N = 30$  meshes was 0.5% and  $-0.05\%$  respectively. The convective term is discretized with a second order central differencing scheme, the time derivative with a second order implicit method and the least squares method was used for gradient calculation.

The numerical values for the material properties of the top phase are defined to be  $\sigma_2/\sigma = 0$ ,  $\rho_2/\rho = 0$  and  $\nu_2/\nu = 0$ , and are necessary for the boundary conditions, for example the pressure in the gas phase is assumed to be constant. The zero conductivity constraint for the top phase was implemented via the boundary condition for the electric potential at the interface.

### 3.3.2 Volume of fluid method

The VOF method is based on solving a transport equation for an indicator function, which determines the spatial distribution of the fractions of two immiscible fluids and consequently the density of the liquid in the Navier-Stokes equations.<sup>15,27</sup> The Continuum Surface Force (CSF) approach is used for implementation of the interfacial tension force between the two fluids<sup>6</sup> and an artificial compression velocity is introduced for sharpening the resulting diffuse interface between the two fluids.<sup>37</sup>

The describing equations for two-phase VOF flows are the continuity equation

$$\frac{\partial v_j}{\partial x_j} = 0, \quad (3.101)$$

where  $v_i$  is the velocity vector, the Navier-Stokes equations,<sup>6,15</sup>

$$\frac{\partial \rho v_i}{\partial t} + v_j \frac{\partial \rho v_i}{\partial x_j} = -\frac{\partial p}{\partial x_i} + \frac{\partial}{\partial x_j} \left[ \mu \left( \frac{\partial v_i}{\partial x_j} + \frac{\partial v_j}{\partial x_i} \right) \right] + f_i + \gamma \kappa \frac{\partial \alpha}{\partial x_i}, \quad (3.102)$$

where  $\alpha$  is the indicator function,  $f_i$  the body force,  $\rho$  and  $\mu$  the phase averaged density and viscosity and  $\kappa$  the curvature of the interface in the CSF approach,<sup>6</sup> determined by

$$\kappa = \frac{\partial}{\partial x_k} \left[ \frac{1}{\left| \frac{\partial \alpha}{\partial x_j} \right|} \frac{\partial \alpha}{\partial x_k} \right]. \quad (3.103)$$

and the transport equation for the indicator function  $\alpha$ <sup>27</sup>

$$\frac{\partial \alpha}{\partial t} + \frac{\partial}{\partial x_j} (\alpha v_j) + \frac{\partial}{\partial x_j} (v_{r,i} \alpha (1 - \alpha)) = 0. \quad (3.104)$$

For the studied liquid-air flow, the indicator function equals 1 for the liquid phase and 0 for the air phase and is in the range  $(0, 1)$  around the interface. The third term includes the

artificial compression velocity,  $v_{r,i}$  and is zero outside the interface region. This term can be derived from the continuity equations for the phase fractions in the two-fluid Euler approach, leading to the relative velocity  $v_{r,i} = v_{l,i} - v_{g,i}$  between the liquid and the gas phase.<sup>4</sup> The term compressibility does not refer to compression of the distinct phases, but compression of the interface itself, which can be seen as additional convection of the phase fraction due to  $v_{r,i}$ .

The body force  $f_i$  is the Lorentz force,

$$f_i = \epsilon_{ijk} j_j b_k. \quad (3.105)$$

The magnetic field  $b_i$  is externally applied and constant in time, whereas the current density  $j_i$  is calculated from the electric potential  $\phi$ . From conservation of current

$$\frac{\partial j_j}{\partial x_j} = 0 \quad (3.106)$$

and the definition of the current density

$$j_i = \sigma \left( -\frac{\partial \phi}{\partial x_i} + \epsilon_{ijk} u_j b_k \right), \quad (3.107)$$

an additional Poisson's equation for the electric potential is introduced

$$\frac{\partial}{\partial x_i} \left( \sigma \frac{\partial \phi}{\partial x_i} \right) = \frac{\partial}{\partial x_i} (\sigma \epsilon_{ijk} u_j b_k), \quad (3.108)$$

where the electrical conductivity  $\sigma$  is linearly interpolated between both phases, which means harmonic interpolation on the resistivity.

### Details of the numerical simulation

The simulations were performed on a square cell grid containing  $20N \times 3N$  cells, where the bottom  $20N \times N$  cells were initially filled with the conductive fluid, and the remaining part was filled with gas. For these simulations hence  $A = 0.05$  and furthermore  $Re = A$ ,  $Ha = 1$ ,  $Ca = A^4$  and  $Bo = A^2$ . Figure 3.7(bottom) shows the vertical velocity component along a horizontal line  $y = 0.5$  for various  $N$ . The difference in maximum velocity obtained on a mesh with  $N = 20$ , compared to  $N = 10$  and  $N = 30$  meshes was 6.6% and 0.2% respectively. The time derivative is discretized using a second order implicit method, whereas the convective and diffusive terms are discretized using a second order central differencing scheme.

The values for  $\sigma_2$ ,  $\rho_2$  and  $\nu_2$  are explicitly used during the simulation, and are non-zero to avoid singularities in the problem. For the present simulations  $\sigma_2/\sigma = 10^{-18}$ ,  $\rho_2/\rho = 10^{-3}$  and  $\nu_2/\nu = 10$ .

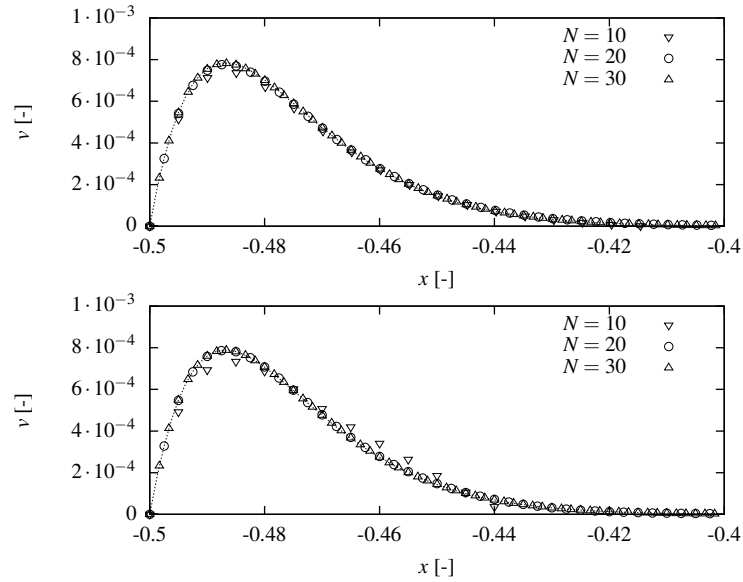


**Figure 3.7** The vertical velocity  $v$  along the horizontal line  $y = 0.5$  for respectively  $N = 10$ ,  $N = 20$  and  $N = 30$ . (top) For the MMIT simulations, where the grid consists of  $20N \times N$  control volumes. (bottom) For the VOF simulations where the grid consist of  $20N \times 3N$  control volumes, with the bottom  $20N \times N$  control volumes initially liquid filled.

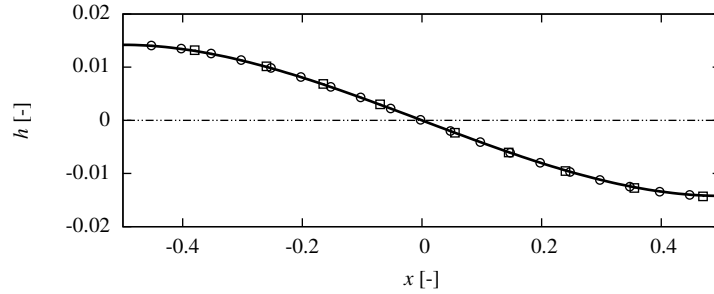
## 3.4 Numerical results

### 3.4.1 Base case

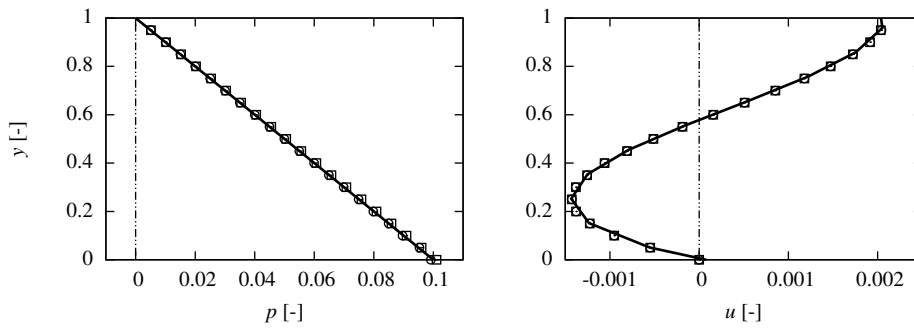
For  $A = 0.1$ , Figure 3.8 compares the free surface elevation of the analytical results for the first order deformation with the numerical results from both the MMIT and VOF method. For  $Re = A$ ,  $Ha = 1$ ,  $Bo = A^2$  and  $Ca = A^4$ , it can be seen that the analytical solution is in good agreement with the numerically determined free surface elevations.

Figure 3.9 shows the pressure and horizontal velocity (from Equation 3.46 and 3.26) for the vertical line  $x = 0$ . Again a good agreement is obtained between analytical results and numerical simulations.

In Figure 3.10, both velocity components along the line  $y = 0.5$  in the region close to the wall are depicted. The analytic solution is obtained from Equation 3.95, with  $P = 1024$ . For both velocity components and both simulation methods, it is seen that the velocity profiles obtained from the numerical simulations accurately match the analytical expression for these components.



**Figure 3.8** Elevation  $h$  of the free surface over the width of the domain for  $A = 0.1$ ,  $Re = A$ ,  $Ha^2 = 1$ ,  $Bo = A^2$  and  $Ca = A^4$ . The MMIT simulation (circles), the VOF simulation (squares) and the first order analytic approximation (solid line) of Equation 3.64 are shown.



**Figure 3.9** Pressure  $p$  (left) and horizontal velocity  $u$  (right) for the line  $x = 0$  for  $A = 0.1$ ,  $Re = A$ ,  $Ha^2 = 1$ ,  $Bo = A^2$  and  $Ca = A^4$ . The MMIT simulation (circles), the VOF simulation (squares) and the first order analytic approximation (solid line) are shown.

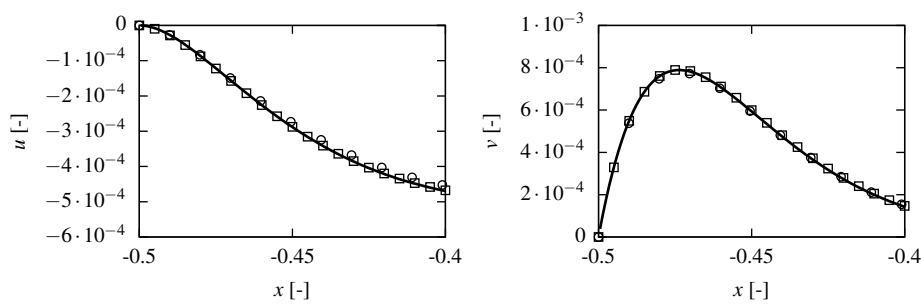


**Figure 3.10** The horizontal (left) and vertical (right) velocity component along the line  $y = 0.5$  for  $A = 0.1$ ,  $Re = A$ ,  $Ha^2 = 1$ ,  $Bo = A^2$  and  $Ca = A^4$ . The MMIT simulation (circles), the VOF simulation (squares) and the first order analytic approximation of Equation 3.95 using  $P = 1024$  (solid line) are shown.

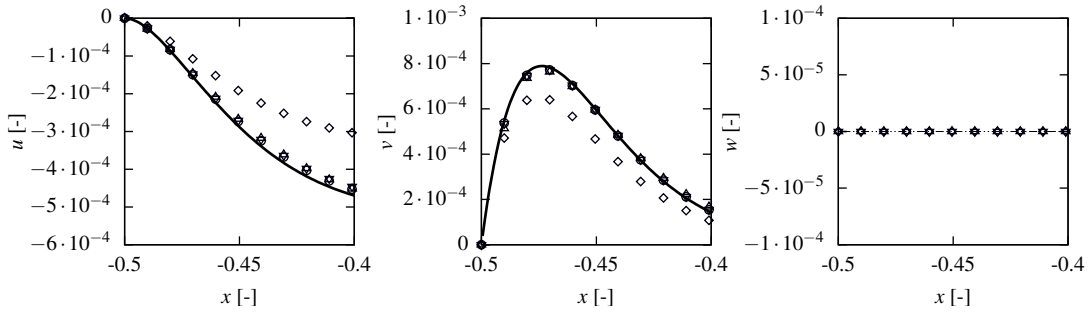


**Figure 3.11** Horizontal (left) and vertical (middle) velocity components (as Figure 3.10) and spanwise velocity component (right), along the line  $y = 0.5$  for  $A = 0.1$ ,  $Re = A$ ,  $Ha^2 = 1$ ,  $Bo = A^2$ ,  $Ca = A^4$  and  $\theta = 90^\circ$ , for the analytical solution (solid line), the two-dimensional numerical simulation ( $\circ$ ), and the numerical simulation for a cavity with  $z$ -dimension  $100d$  ( $\triangle$ ),  $10d$  ( $\nabla$ ) and  $d$  ( $\diamond$ ).

### 3.4.2 Three-dimensionality of the flow

In this section we will numerically evaluate, using the MMIT method, the effect of bounding walls in the third dimension on the two-dimensional flow in the  $z = 0$ -plane. In the  $z = 0$ -plane, the Lorentz force has a zero component in the  $z$ -direction, therefore the three-dimensionality of the magnetic field does not influence the equations for  $u$  and  $v$  in that plane (Equations 3.22 and 3.23). By introducing walls to bound the domain in the  $z$  direction, however, additional viscous shear from these walls can be expected. Figure 3.11 compares the velocity components for increasing size  $w$  of the domain in the  $z$ -direction. This size was consecutively increased from  $w = d$ , to  $w = d/A$  and to  $w = d/A^2$ . For  $w = d$ , the velocities in the  $xy$ -plane are significantly smaller than analytically derived, whereas the shape of these velocity profiles has not changed. This is caused by the viscous shear from the walls that bound the domain in the  $z$ -direction. When the extend of the domain in the  $z$  direction increases, Figure 3.11 shows that the velocity profiles converge to the velocity profile from the two-dimensional numerical simulation and the analytical solution, without generating a significant velocity component in the spanwise direction. Therefore, for large enough domain sizes in the third dimension, the presented two-dimensional analytical solution is valid for the flow in the  $z = 0$ -plane of the formulated three-dimensional problem.

### 3.4.3 Increased deformation

Section 3.2.7 showed the difficulties in deriving the final solution for increasing Hartmann number. In this section we will obtain numerical results for the surface elevation under higher Hartmann number, as well as higher capillary number, Bond number, Reynolds number and aspect ratio, in order to determine to what degree the analytic solution of Equation 3.64 holds.



### MMIT

Figure 3.12 shows the free surface elevation for a set of cases in which, starting from  $A = 0.1$ ,  $\theta = 90^\circ$ ,  $Re = A$ ,  $Ha^2 = 1$ ,  $Ca = A^4$ ,  $Bo = A^2$ , either of the parameters  $Ha$ ,  $Ca$ ,  $Bo$  or  $A$  is increased to large values for which the analytical solution is not expected to hold.

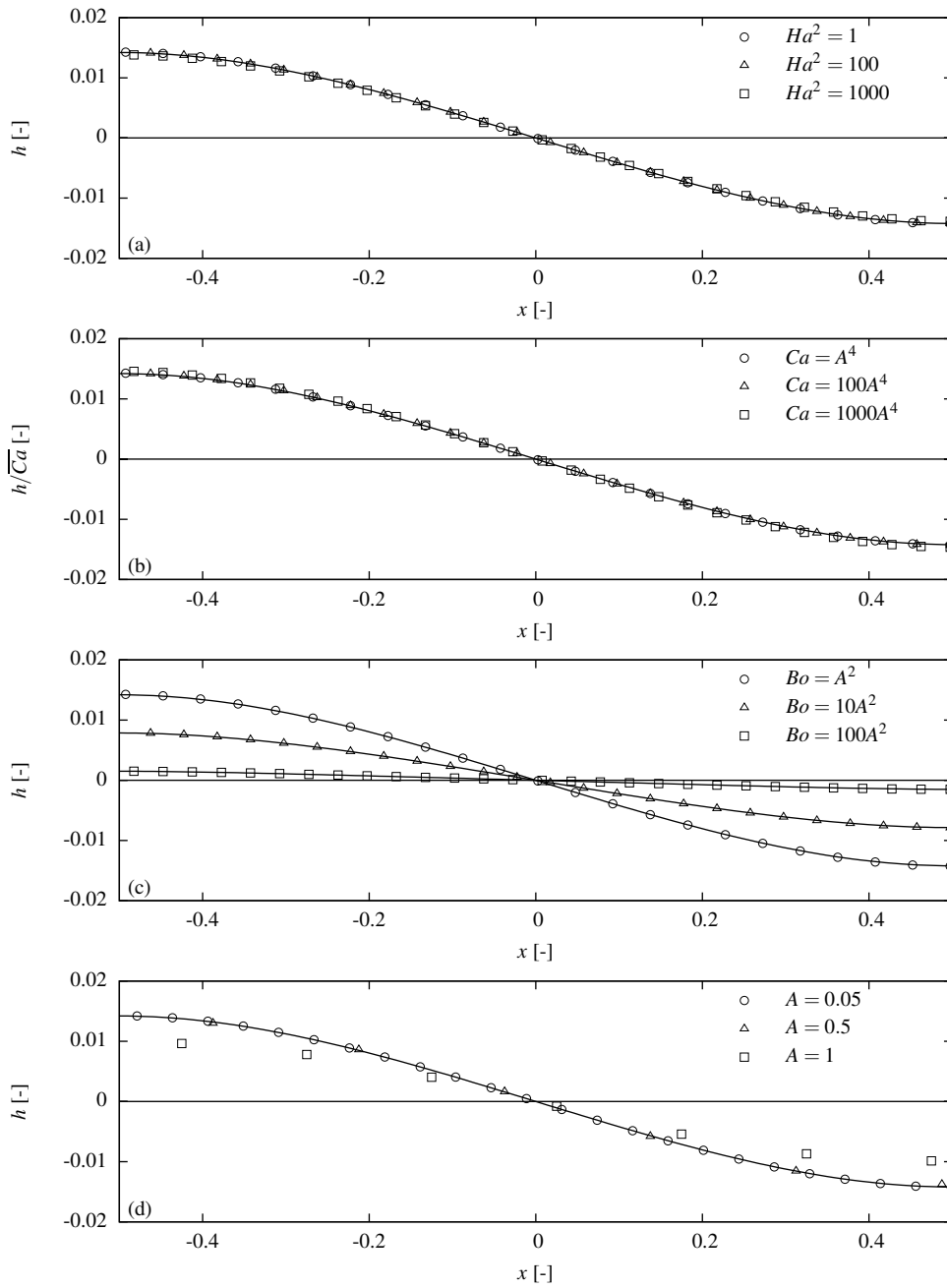
From Figure 3.12(a) it can be seen, that, even though the derivation for the free surface elevation is valid for  $Ha^2 \leq O(1)$ , the analytical solution using  $Ha^2 = 1000$  still closely agrees with the numerical solution.

Also for capillary number increasing up to  $Ca = 1000A^4$ , the numerical solution remains close to the analytical expression, as can be seen from Figure 3.12(b), where both numerical and analytical free surface elevations are scaled with the capillary number. We obtain this results, even though from a comparison between the boundary condition used with the present assumptions on  $Ca$  (Equation 3.41) and the full boundary condition (Equation 3.13), it follow that for increasing values of  $Ca$  the boundary condition gets increasingly complex. Figure 3.12(c) shows that for increasing  $Bo$  numbers, the free surface elevation quickly decreases, as does the surface curvature in the core, in line with Equation 3.64. The analytical model fits the numerical data well for increasing  $Bo$ . Finally, Figure 3.12(d) shows that for an aspect ratio as large as  $A = 0.5$ , the analytically determined free surface elevation is still matching the numerical result of the MMIT method very well.

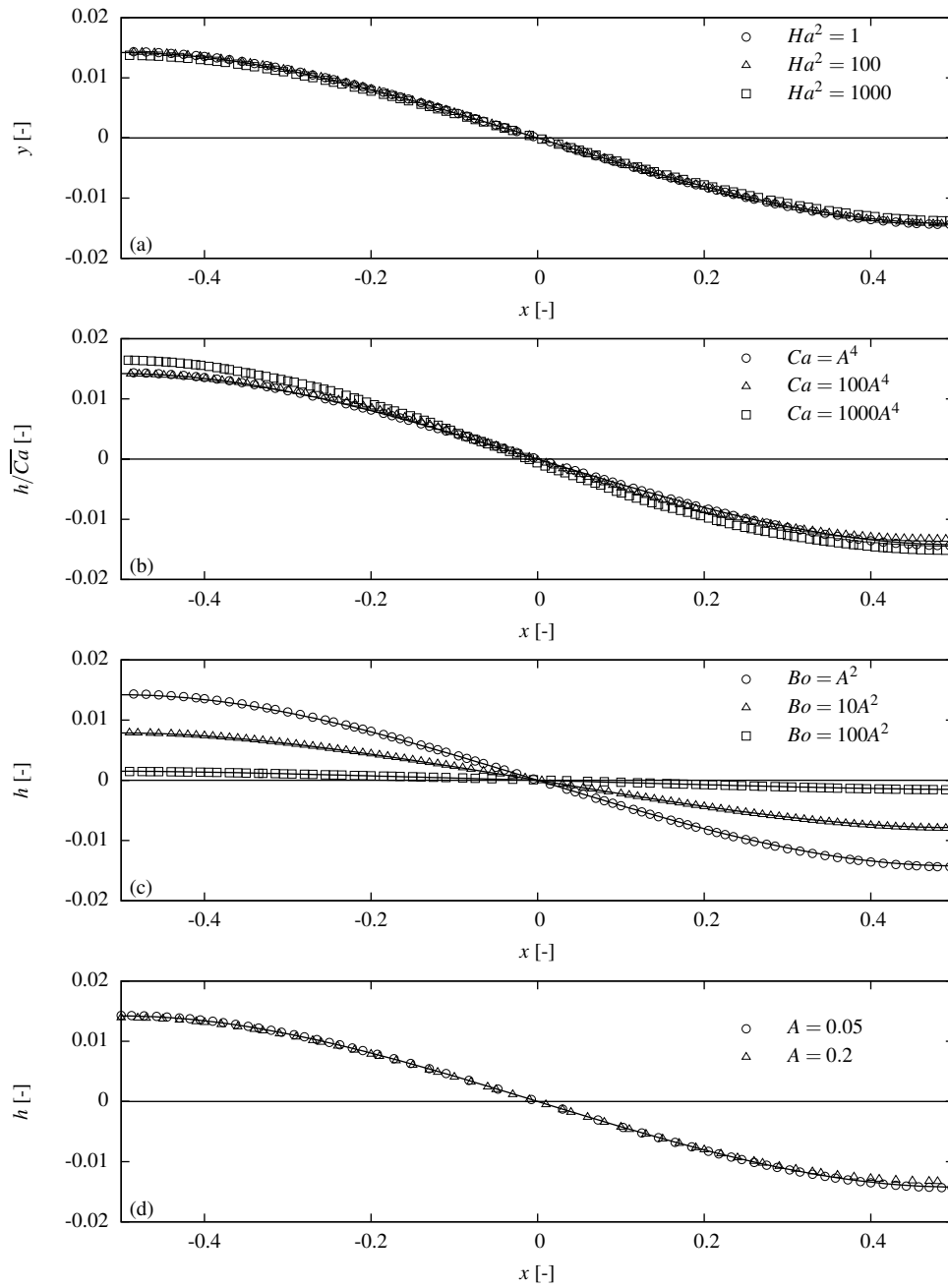
### VOF

Figure 3.13 shows what happens to the free surface elevation when increasing either  $Ha$ ,  $Ca$ ,  $Bo$  and  $A$  using the VOF method. As for the MMIT method, it is seen that the analytical expression for the free surface elevation is relatively accurate even for larger values of the dimensionless parameters than assumed in deriving the analytical model. This is especially so for  $Ha$  and  $Bo$ .

For large  $Ca = 1000A^4$ , the free surface elevation starts to deviate visibly, whereas for  $A \geq 0.5$ , the simulations did not result in a converged steady state solution, which we have also seen for  $Ha^2 > 4000$ . As various of the properties are varied over many orders of magnitude, challenges with numerical stability are not surprising. Further addressing these issues is outside the scope of this chapter. We can however conclude that the MMIT method is more robust in handling these parameter variations.



**Figure 3.12** The surface elevation  $h$  from the MMIT simulations (symbols), horizontally rescaled to  $[-0.5, 0.5]$ , where from  $A = 0.1$ ,  $Ha^2 = 1$ ,  $Ca = A^4$ ,  $Bo = A^2$ , either of the parameters  $Ha^2$  (a),  $Ca$  (b),  $Bo$  (c) and  $A$  (d) is varied. The solid line indicates the analytic solution (Equation 3.64)



**Figure 3.13** The surface elevation  $h$  from the VOF simulations (symbols), horizontally rescaled to  $[-0.5, 0.5]$ , where from  $A = 0.1$ ,  $Ha^2 = 1$ ,  $Ca = A^4$ ,  $Bo = A^2$ , either of the parameters  $Ha^2$  (a),  $Ca$  (b),  $Bo$  (c) and  $A$  (d) is varied. The solid line indicates the analytic solution (Equation 3.64)

### 3.4.4 Error

The normalized root mean square distance between the derived analytical elevation (Equation 3.64) and the calculated profile is defined as

$$e[x_i] = \frac{\sum_i (A^2 h(x_i A) - y_i)^2}{\sum_i (A^2 h(x_i A))^2} \quad \text{with } h(x) = \frac{3 \overline{Ca}}{8 \overline{Bo}} \left( \frac{\sinh(\sqrt{Bo} x)}{\cosh\left(\frac{1}{2}\sqrt{Bo}\right)} \frac{1}{\sqrt{Bo}} - x \right) \quad (3.109)$$

Figure 3.14 shows this normalized root mean square distance for either increasing  $Ha^2$ ,  $Ca$ ,  $Bo$ ,  $A$  or  $Re$  and for both numerical approaches. This distance is a measure for the deviation of the analytical result from the numerical simulation. It shows that the analytical solution starts to deviate more than 1% from the numerical solution for  $Ha^2 > 1000$ . For  $Ca > 1000A^4$  the analytical solution deviates more than 1% from the MMIT solution.

For the aspect ratio it is also concluded from Figure 3.14, that the analytical solution is within 1% from the free surface elevation obtained from the MMIT model for values of the aspect ratio  $A$  up to 0.5. For Reynolds numbers increasing to  $Re = 1000A$ , the free surface elevation obtained from the analytic model is within 1% from the free surface elevation obtained from the MMIT method.

In general, it can be seen from Figure 3.14 that the VOF solution for the free surface elevation always deviates more from the analytical solution than the MMIT solutions. In addition to the numerical challenges mentioned above, it should be noted that the properties of the top phase are non-zero in the VOF simulation, in contrast to the MMIT simulations and analytical derivation.

## 3.5 Conclusions

In this chapter we have studied the flow and free surface elevation of a layer of conductive liquid with height-to-width ratio  $A \ll 1$ , that is subject to a potential difference horizontally across the domain and a traverse  $x$ -dependent magnetic field. It was shown that the surface tension and gravity forces in combination with the unevenly distributed Lorentz forces on the fluid induce a steady state flow, which scales linearly with conductivity, magnetic field gradient and applied potential difference and which vanishes for infinitely long layers ( $A \rightarrow 0$ ), whereas the free surface deformation depends on the capillary number, the Bond number and the contact angle condition.

Increasing pressure within the layer will cause the interface to deform. The profile of this interface was derived analytically for Hartmann numbers up to  $O(1)$ , capillary numbers up to  $O(A^4)$ , Bond numbers up to  $O(A^2)$  and Reynolds numbers up to  $O(A)$ , while  $A \ll 1$ . It was proven that to lowest order approximation, the surface elevation profile is a function of the capillary number, the Bond number and the contact angle condition. The magnitude

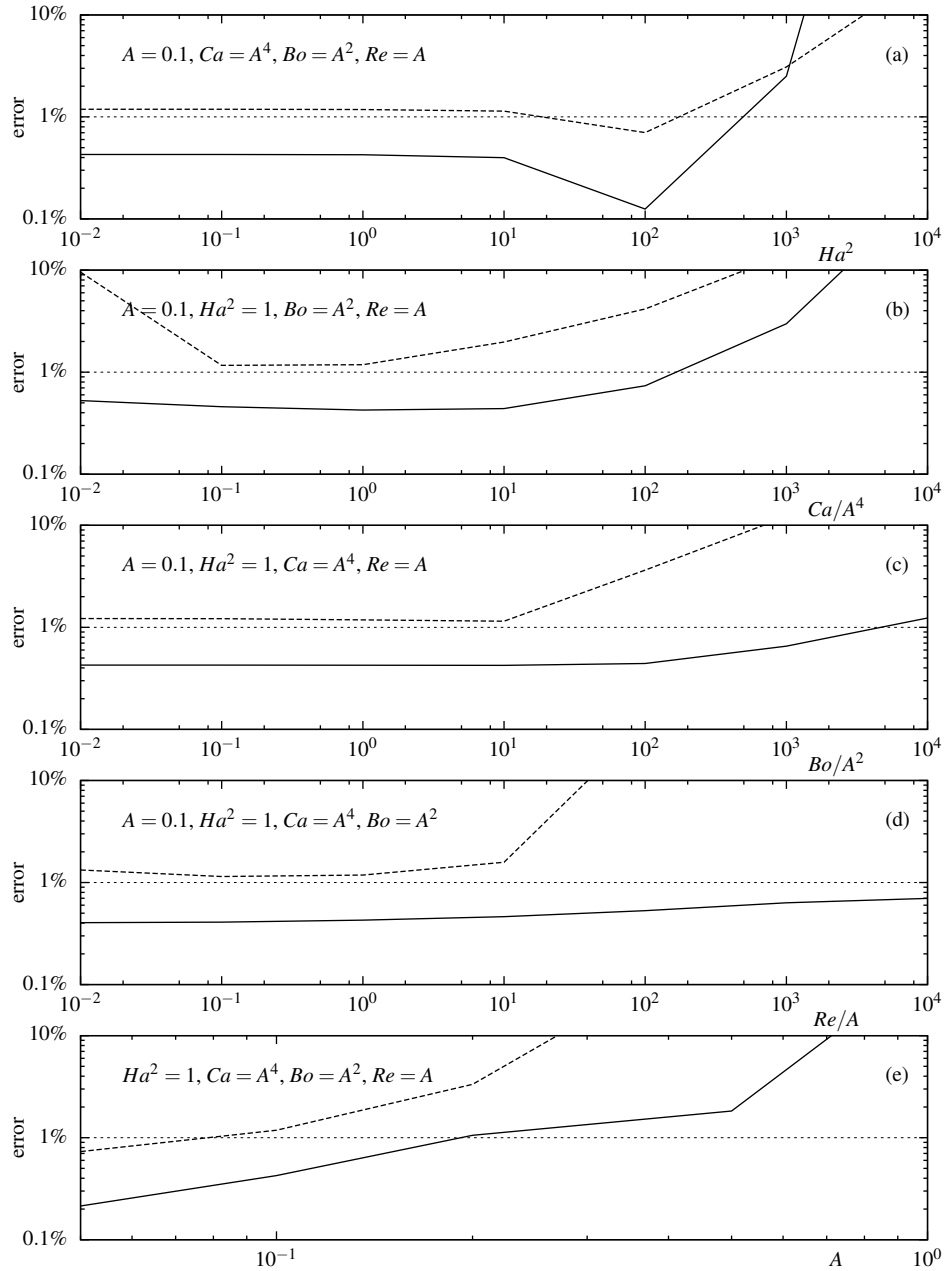


**Figure 3.14** The normalized root mean square distance between the rescaled elevation from the numerical simulation, either MMIT (solid line) or VOF (dashed line) and the analytical free surface elevation, where from the case  $A = 0.1, Re = A, Ha^2 = 1, Ca = A^4$  and  $Bo = A^2$  either (from top to bottom)  $Ha^2, Ca, Bo, A$  or  $Re$  is varied. The root mean square distance is normalized with  $\int h^2(x) dx$ .

of the free surface displacement scales linearly with the capillary number and decreases with increasing Bond number. The shape of the free surface is determined by both the Bond number and the contact angle boundary condition.

Furthermore, the biharmonic equation for the stream function in the side wall region was solved analytically, showing the turning of the flow and the presence of small eddies in the corner regions.

The first order approximation of the analytic solution was compared to finite volume computational models for free surface flow simulation using either a moving mesh interface tracking technique or a volume of fluid method to track the interface, in combination with a one-way coupled MHD solver via the equation for the electric potential. The analytically derived elevation and subsurface flow properties match the numerical simulations well.

The analytical solution presented in this paper is derived up to  $O(A)$ . This means that the lowest order neglected terms are of order  $O(A^2)$ . For small enough aspect ratio ( $A = 0.1$ ) these terms quickly reduce to values smaller than 1%. Indeed, the difference with the numerically found solution is only 0.4% (MMIT) and 1.2% (VOF) for  $A = 0.1$ . We therefore conclude that the contribution of the neglected higher order terms in the analytical solution, for an aspect ratio of 0.1, is smaller than 1%.

From our numerical simulations we have observed that the MMIT method is more robust than the VOF method. Using the MMIT simulations, it is observed, that for larger values of the Hartmann number, capillary number, Bond number, Reynolds number and aspect ratio, where the underlying assumptions of the analytic solution are no longer satisfied, the analytical solution and numerical results match within 1%, for  $A = 0.1$  and either  $Ha^2$  up to 400,  $Ca$  up to  $200A^4$  or  $Bo$  up to  $100A^2$  and within 2% for  $A = 0.5$ .

## Bibliography

- [1] Alboussière, T., Garandet, J. P., and Moreau, R. Asymptotic analysis and symmetry in MHD convection. *Physics of Fluids*, volume 8(8):pp. 2215–2226 (1996).
- [2] Ben Hadid, H. and Henry, D. Numerical study of convection in the horizontal Bridgman configuration under the action of a constant magnetic field. Part 2. Three-dimensional flow. *Journal of Fluid Mechanics*, volume 333:pp. 57–83 (1997).
- [3] Benthem, J. A Laplace transform method for the solution of semi-infinite and finite strip problems in stress analysis. *Quarterly Journal of Mechanics and Applied Mathematics*, volume 16(4):pp. 413–429 (1963).
- [4] Berberović, E., van Hinsberg, N. P., Jakirlić, S., Roisman, I. V., and Tropea, C. Drop impact onto a liquid layer of finite thickness: Dynamics of the cavity evolution. *Physical Review E*, volume 79(3):p. 036306 (2009).
- [5] Bian, W., Vasseur, P., and Bilgen, E. Effect Of An External Magnetic Field On Buoyancy-driven Flow In a Shallow Porous Cavity. *Numerical Heat Transfer, Part A: Applications*, volume 29(6):pp. 625–638 (1996).
- [6] Brackbill, J. U., Kothe, D. B., and Zemach, C. A continuum method for modeling surface tension. *Journal of Computational Physics*, volume 100(2):pp. 335–354 (1992).
- [7] Cormack, D., Stone, G., and Leal, L. The effect of upper surface conditions on convection in a shallow cavity

- with differentially heated end-walls. *International Journal of Heat and Mass Transfer*, volume 18(5):pp. 635–648 (1975).
- [8] Davidson, P. A. *An Introduction to Magnetohydrodynamics*. Cambridge University Press, 1 edition (2001).
- [9] Davoust, L., Cowley, M. D., Moreau, R., and Bolcato, R. Buoyancy-driven convection with a uniform magnetic field. Part 2. Experimental investigation. *Journal of Fluid Mechanics*, volume 400:pp. 59–90 (1999).
- [10] Duffy, D. G. *Transform methods for solving partial differential equations*. CRC Press (1994).
- [11] Fautrelle, Y. and Sneyd, A. D. Instability of a plane conducting free surface submitted to an alternating magnetic field. *Journal of Fluid Mechanics*, volume 375:pp. 65–83 (1998).
- [12] Garandet, J. and Alboussière, T. Bridgman growth: Modelling and experiments. *Progress in Crystal Growth and Characterization of Materials*, volume 38(1):pp. 73–132 (1999).
- [13] Garandet, J., Alboussière, T., and Moreau, R. Buoyancy driven convection in a rectangular enclosure with a transverse magnetic field. *International Journal of Heat and Mass Transfer*, volume 35(4):pp. 741–748 (1992).
- [14] Gillon, P. Materials processing with high direct-current magnetic fields. *JOM*, volume 47(5):pp. 34–37 (1995).
- [15] Hirt, C. and Nichols, B. Volume of fluid (VOF) method for the dynamics of free boundaries. *Journal of Computational Physics*, volume 39(1):pp. 201–225 (1981).
- [16] Hughes, W. F. and Elco, R. A. Magnetohydrodynamic lubrication flow between parallel rotating disks. *Journal of Fluid Mechanics*, volume 13(01):pp. 21–32 (1962).
- [17] Hunt, J. C. R. Magnetohydrodynamic Flow in Rectangular Ducts. *Journal of Fluid Mechanics*, volume 21(04):pp. 577–590 (1965).
- [18] Juel, A., Mullin, T., Ben Hadid, H., and Henry, D. Magnetohydrodynamic convection in molten gallium. *Journal of Fluid Mechanics*, volume 378:pp. 97–118 (1999).
- [19] Kharicha, A., Teplyakov, I., Ivochkin, Y., Wu, M., Ludwig, A., and Guseva, A. Experimental and numerical analysis of free surface deformation in an electrically driven flow. *Experimental Thermal and Fluid Science*, volume 62:pp. 192–201 (2015).
- [20] Kwok, Y. K. *Applied Complex Variables*. Cambridge University Press, New York, 1 edition (2002).
- [21] Lehnert, B. An Instability of Laminar Flow of Mercury Caused by an External Magnetic Field. *Proceedings of the Royal Society of London. Series A, Mathematical and Physical Sciences*, volume 233(1194):pp. 299–302 (1955).
- [22] Meylan, M. H. and Gross, L. A parallel algorithm to find the zeros of a complex analytic function. *ANZIAM Journal*, volume 44(0):pp. E236–E254 (2003).
- [23] Moffatt, H. K. Viscous and resistive eddies near a sharp corner. *Journal of Fluid Mechanics*, volume 18(01):pp. 1–18 (1964).
- [24] Muzaferija, S. and Perić, M. Computation of Free-Surface Flows using the Finite-Volume Method and Moving Grids. *Numerical Heat Transfer, Part B: Fundamentals*, volume 32(4):pp. 369–384 (1997).
- [25] Northrup, E. F. Some Newly Observed Manifestations of Forces in the Interior of an Electric Conductor. *Physical Review (Series I)*, volume 24(6):pp. 474–497 (1907).
- [26] Ozoe, H. and Okada, K. The effect of the direction of the external magnetic field on the three-dimensional natural convection in a cubical enclosure. *International Journal of Heat and Mass Transfer*, volume 32(10):pp. 1939–1954 (1989).
- [27] Rusche, H. *Computational Fluid Dynamics of Dispersed Two-Phase Flows at High Phase Fractions*. PhD thesis, Imperial College (2002).
- [28] S. Oshima and R. Yamane. Shape-control of Liquid Metal Free Surfaces by Means of a Static Magnetic Field. In J. Szekely, J. W. Evans, K. Blazek, and N. El-Kaddah, editors, *Magnetohydrodynamics in Process Metallurgy*, pp. 251–259. The Minerals, Metals and Materials Society (1991).

- [29] Sen, A. K. and Davis, S. H. Steady thermocapillary flows in two-dimensional slots. *Journal of Fluid Mechanics*, volume 121:p. 163 (1982).
- [30] Series, R. W. and Hurlle, D. T. J. The use of magnetic fields in semiconductor crystal growth. *Journal of Crystal Growth*, volume 113(1-2):pp. 305–328 (1991).
- [31] SGI Corp. OpenFOAM (2012).
- [32] Shercliff, J. A. The Flow of Conducting Fluids in Circular Pipes Under Transverse Magnetic Fields. *Journal of Fluid Mechanics*, volume 1(06):pp. 644–666 (1956).
- [33] Sundaravivelu, K., Kandaswamy, P., and Kumar, K. Effect of magnetic field on the liquid-gas interfacial deformation in thermocapillary convection problem. *Zeitschrift für angewandte Mathematik und Physik*, volume 51(3):p. 491 (2000).
- [34] The OpenFOAM extend project. OpenFOAM-extend (2012).
- [35] Tuković, Z. and Jasak, H. A moving mesh finite volume interface tracking method for surface tension dominated interfacial fluid flow. *Computers and Fluids*, volume 55:pp. 70–84 (2012).
- [36] Verhulst, F. *Methods and Applications of Singular Perturbations*. Springer Science+Business Media, Inc., 1 edition (2005).
- [37] Weller, H. G. A New Approach to VOF-based Interface Capturing Methods for Incompressible and Compressible Flow. Technical report, OpenCFD (2008).





# 4. Dynamics of a single, oscillating turbulent jet in a confined cavity<sup>§</sup>

We demonstrate how the self-sustained oscillation of a confined jet in a thin cavity can be quantitatively described by a zero-dimensional model of the delay differential equation type with two a priori predicted model constants. This model describes the three phases in self-sustained oscillations, viz.: (i) pressure driven growth of the oscillation, (ii) amplitude limitation by geometry and (iii) delayed destruction of the recirculation zone. The two parameters of the model are the growth rate of the jet angle by a pressure imbalance, and the delay time for the destruction of this pressure imbalance. We present closed relations for both model constants as a function of the jet Reynolds number  $Re$ , the inlet velocity  $v_{in}$ , the cavity width  $W$  and the cavity width over inlet diameter  $W/d$  and we demonstrate that these model constants do not depend on other geometric ratios. The model and the obtained model constants have been successfully validated against three dimensional Large Eddy Simulations, and planar Particle Image Velocimetry measurements, for  $1600 < Re \leq 7100$  and  $20 \leq W/d < 50$ . The presented model inherently contains the transition to a non-oscillating mode for decreasing Reynolds numbers or increasing  $W/d$ -ratios and allows for the quantitative prediction of the corresponding critical Reynolds number and critical  $W/d$ .

## 4.1 Introduction

A fluid jet may demonstrate self-sustained oscillations when it is confined in both directions perpendicular to its flow direction. This phenomenon has been observed for jet Reynolds numbers ranging from  $Re = 100^{2,11,19,31}$  up to  $Re = 170,000$ .<sup>20</sup> The physical mechanism for this oscillation is well understood for both laminar<sup>31</sup> and turbulent<sup>10</sup> jets. The dimen-

<sup>§</sup>Published as: Righolt, B. W., Kenjereš, S., Kalter, R., Tummers, M. J., and Kleijn, C. R., Dynamics of an oscillating turbulent jet in a confined cavity. *Physics of Fluids*, 27:095107, 2015

sions of the confining cavity are known to have an important influence on the presence and frequencies of these oscillations. For very wide cavities, the domain becomes unbounded in one direction, and the self-sustained oscillation disappears.<sup>18</sup> A jet in such a wide cavity shows meandering, self-similar behavior.<sup>13</sup> For decreasing cavity width, the oscillation frequency increases,<sup>14,18</sup> until the cavity geometry approaches that of a sudden expansion, where strong asymmetries and oscillations are present as well.<sup>4,6,7</sup> A vast amount of fluidic oscillators exist,<sup>10,19,23,25</sup> which are for example found in backward facing steps, flows over cavities<sup>24</sup> and jets through orifices.<sup>22</sup> The systems have in common that either implicitly or explicitly a delayed feedback loop is present that triggers the oscillatory behavior.

Delayed feedback mechanisms are very common in nature and technology and can result in oscillations of any type. Some of these mechanisms can be described by a delay differential equation (DDE) with a single delay constant. The delay time between the uptake of oxygen in the lungs and the reception in the brain stem plays a role in the arterial  $CO_2$  control system.<sup>16</sup> In economics, the interplay between income and capital stock can be explained with a time delay in investments.<sup>29</sup> Another example is the large time-scale temperature oscillation on the southern hemisphere, often referred to as *El Niño*, with a delay time that is associated with the transit time of Rossby and Kelvin waves across the Pacific ocean.<sup>3,28</sup> DDE models have also been proposed for the oscillation of the reattachment length in a confined jet flow<sup>31</sup> or for convective rolls in a closed box.<sup>30</sup> Although the physical mechanism active in each of the above examples may be very different, they have all been successfully described with DDE-type models.

The objective of the present study is (i) to develop a DDE-type model for the oscillations of a turbulent jet in a confined cavity, which represents the physical phases of the oscillating motion and (ii) to use this model to predict necessary conditions for the existence of self-sustained oscillations depending on the jet Reynolds number  $Re$ , and cavity width to nozzle diameter ratio  $W/d$ . We use both Large Eddy Simulations and experimental data to validate our DDE model and its predictions.

The paper is outlined as follows. The confined jet configuration and numerical methods for 3D LES turbulent flow simulations are given in section 4.2, the experimental validation of the numerical flow simulations is presented in section 4.3. In section 4.4 we present a zero-dimensional DDE-type model for single jet oscillations in a confined cavity and in section 4.5 we discuss how the model parameters in the DDE model can be obtained from given flow properties.

## 4.2 Methods

### 4.2.1 Description of setup

In this paper we study the flow in a cavity as depicted in Figure 4.1. This cavity has dimensions height  $\times$  width  $\times$  thickness ( $H \times W \times T$ ). A downward oriented square tube of inner

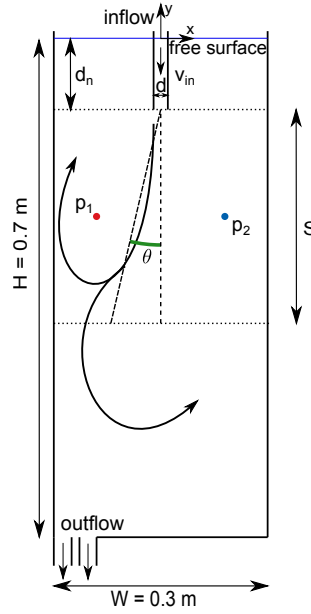


**Figure 4.1** Studied configuration of a single jet in a confined geometry. The cavity has dimensions  $H \times W \times T = 0.7 \times 0.3 \times 0.035 \text{ m}^3$ . The nozzle inner width is  $d = 0.01 \text{ m}$  and is submerged by a distance  $d_n = 0.1 \text{ m}$ . The definition of the instantaneous jet angle  $\theta$ , which is calculated between the nozzle exit and a line at a distance  $S$  downstream from the nozzle exit, and monitoring locations  $p_1$  and  $p_2$  are indicated.

dimensions  $d$  is inserted centrally to a depth  $d_n$ , which injects the fluid into the cavity with a velocity  $v_{in}$ . For  $H \times W \times T = 0.7 \times 0.3 \times 0.035 \text{ m}^3$ ,  $d = 0.01 \text{ m}$  and  $d_n = 0.1 \text{ m}$ , the flow of salt water in this configuration is essentially two-dimensional, as will be demonstrated further in this paper by showing its insensitivity to the precise value of  $T$ , and to friction at the front and back walls. The flow in this configuration was previously investigated experimentally using planar particle imaging velocimetry by Kalter et al.<sup>10</sup>. The outflow was placed off center, in order to allow for optical access. In the present study we use the same dimensions  $H$ ,  $T$ ,  $d$ ,  $d_n$ , whereas the width  $W$  is varied between  $W/d = 10$  and  $W/d = 100$ . For the cases  $W/d \geq 50$  the height  $H$  was increased to  $H/W = 2.5$ . The top of the cavity is a free surface and the working fluid has a density  $\rho = 1.1 \times 10^3 \text{ kgm}^{-3}$  and viscosity  $\nu = 1.27 \times 10^{-6} \text{ m}^2\text{s}^{-1}$ .

In Figure 4.1 the instantaneous jet angle  $\theta$  is defined. The jet angle was determined by a least squares fit of a straight line through the points  $x_i = \max_x(|v(y_i)|)$ , in other words, through the  $x$ -coordinates of the locations of maximum velocity magnitude for every line  $y = y_i$  in the range  $(-d_n - S) < y_i < (-d_n)$ , where we set  $S$  equal to  $W$ . Figure 4.2 shows the collections  $(x_i, y_i)$  and the resulting linear fit for three time instances in half a period of the

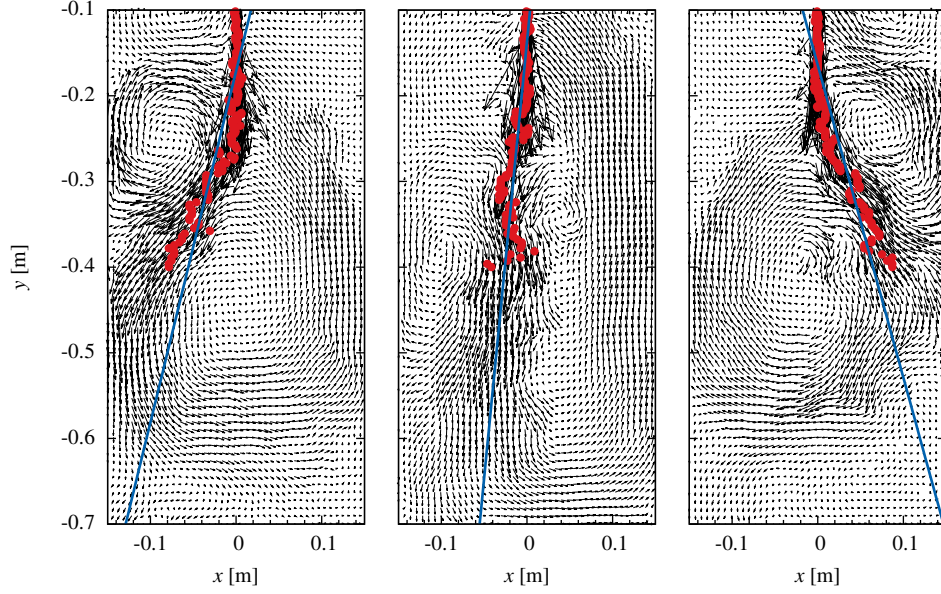


**Figure 4.2** The instantaneous jet angle is calculated from a least squares fit (blue line) through the points of maximum velocity (red dots) per  $y$ -coordinate in the instantaneous velocity field obtained from the numerical simulation (black vectors). Here shown for  $Re = 4700$  and  $W/d = 30$  at  $t = 64$  s (left), a quarter period later at  $t = 74$  s and half a period later at  $t = 84$  s.

oscillation.

## 4.2.2 Numerical fluid flow models

We consider the LES filtered, single phase, incompressible Navier-Stokes equations

$$\frac{\partial v_i}{\partial t} + v_j \frac{\partial v_i}{\partial x_j} = \frac{\partial}{\partial x_j} \left[ (\nu + \nu_{SGS}) \left( \frac{\partial v_i}{\partial x_j} + \frac{\partial v_j}{\partial x_i} \right) \right] - \frac{1}{\rho} \frac{\partial p}{\partial x_i}, \quad (4.1)$$

where  $v_i$  is the velocity,  $\rho$  the fluid density,  $\nu$  the laminar viscosity,  $\nu_{SGS}$  the sub-grid-scale viscosity from the LES model and  $p$  the pressure. We use the finite-volume based tool OpenFOAM 2.1<sup>34</sup> to solve the discretized equations using the PISO scheme.<sup>8</sup>

The dynamic Smagorinsky model<sup>15</sup> has been employed to calculate the sub-grid-scale viscosity as  $\nu_{SGS} = (C\Delta)^2 \mathcal{S}$ , where  $\Delta$  is the local grid size, defined as  $\Delta = (\Delta_x \Delta_y \Delta_z)^{1/3}$  and  $\mathcal{S}$  the characteristic rate of strain,  $\mathcal{S} = (2S_{ij}S_{ij})^{1/2}$  and  $S_{ij} = (\partial v_i / \partial x_j + \partial v_j / \partial x_i) / 2$ . The Smagorinsky constant  $C$  is defined as  $C = \langle L_{ij} M_{ij} \rangle / 2 \langle M_{ij}^2 \rangle$ , with the resolved stress tensor  $L_{ij} = \widetilde{v_i v_j} - \widetilde{v_i} \widetilde{v_j}$  and  $M_{ij} = 2\Delta^2 \widetilde{\mathcal{S} S_{ij}} - 2(\Delta^2)^2 \widetilde{\mathcal{S} S_{ij}}$ , where  $\widetilde{\cdot}$  indicates the fil-

tering operation. An important advantage of the dynamic Smagorinsky model for the studied application is that it automatically handles the damping of turbulence towards the walls.

As recommended by Lilly<sup>15</sup> we use local averaging (indicated by  $\langle \cdot \rangle$ ) of the Smagorinsky coefficient in order to reduce computational instabilities, due to local small values of  $M_{ij}^2$ . We follow the approach of Zang et al.<sup>35</sup> and apply averaging over three control volumes in every direction, as well as clipping of the total viscosity  $\nu + \nu_{SGS}$  at 0, in order to partially allow for backscatter, i.e. the transfer of energy to larger scales.<sup>15</sup> For the studied applications, the region where  $\nu_{SGS}/\nu < -0.5$  occupies less than 1% of the total domain.

The equations are discretized on an orthogonal, rectangular mesh, consisting of  $128 \times 275 \times 34 \approx 1.1 \times 10^6$  grid cells. This being a sufficient grid resolution is demonstrated in Figure 4.3(bottom), which shows contours of the instantaneous  $\nu_{SGS}/\nu$ . The maximum value  $\nu_{SGS}/\nu \leq 10$ , and the domain averaged  $\nu_{SGS}/\nu = 0.1$ .

Temporal discretization is done using a second order fully implicit scheme,<sup>34</sup> with a time step corresponding to  $\max(Co = u\Delta t/\Delta x) = 1$ . Within the distributed version of OpenFoam, higher order explicit temporal discretization schemes are not available. Moreover, Vuorinen et al. have shown that their implementation and application of a third and fourth Runge-Kutta explicit temporal discretization within OpenFOAM led to a small efficiency gain only. The convective and diffusive terms are spatially discretized using a second order central differencing scheme.

The instantaneous value of  $y^+$  at the walls locally reaches values as low as  $y^+ = 0.1$  and as high as  $y^+ = 15$ . We therefore apply, at all solid wall boundaries, a universal velocity profile called Spalding's law,<sup>27</sup> viz.  $y^+ = u^+ + 1/E [\exp(\kappa u^+) - (1 + \kappa u^+ + 1/2(\kappa u^+)^2 + 1/6(\kappa u^+)^3)]$ , with  $y^+ = yu_\tau/\nu$ ,  $u^+ = v/u_\tau$ , the friction velocity  $u_\tau^2 = (\nu + \nu_{SGS}) dv/dn$ ,  $\kappa = 0.41$  and  $E = 9.8$ .<sup>5,9,17,32</sup> This law is valid for  $0 \leq y^+ \leq 300$  and we therefore generally apply it to all walls of the domain. For  $y^+ < 10$ , which is the case for most parts of the walls, Spalding's law reduces to the laminar flow no-slip boundary condition. Indeed, using a laminar flow boundary condition instead of Spalding's law led to minor changes in the flow behaviour only. This also indicates that our simulations are relatively insensitive to the near-wall grid size.

For the inflow via the nozzle, a periodic inlet domain, of length  $10d$ , was applied to guarantee fully developed inflow conditions. The free liquid surface at  $y = 0$  was modeled using a free slip boundary condition.

### 4.3 Validation of the numerical method

We validate the numerical model for a jet of  $Re = v_{in}d/\nu = 4700$  in a confined cavity as defined in Figure 4.1 using data from our previous experiments.<sup>10</sup> In Figure 4.3 vectors of the mean velocity and contours of the horizontal and vertical components of the mean velocity are depicted, both for the present numerical simulation and for the experiment. In Figure

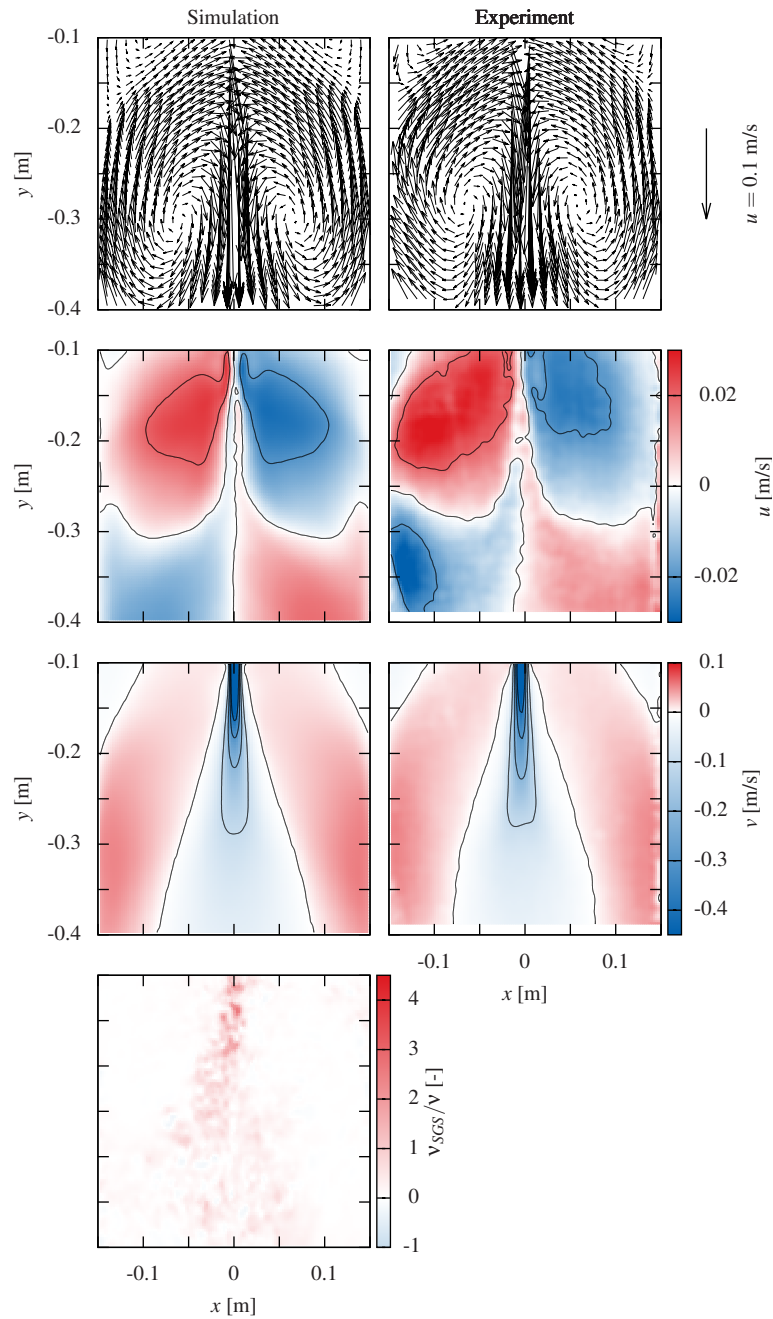


**Figure 4.3** For  $Re = 4700$  and  $W/d = 30$  in the  $z = 0$ -plane, simulation (left) and experiment (right), from top to bottom: Vector fields of the mean velocity, contours of the horizontal mean velocity, contours of the vertical mean velocity and contours of the scaled instantaneous sub-grid-scale viscosity  $\nu_{SGS}/\nu$ .

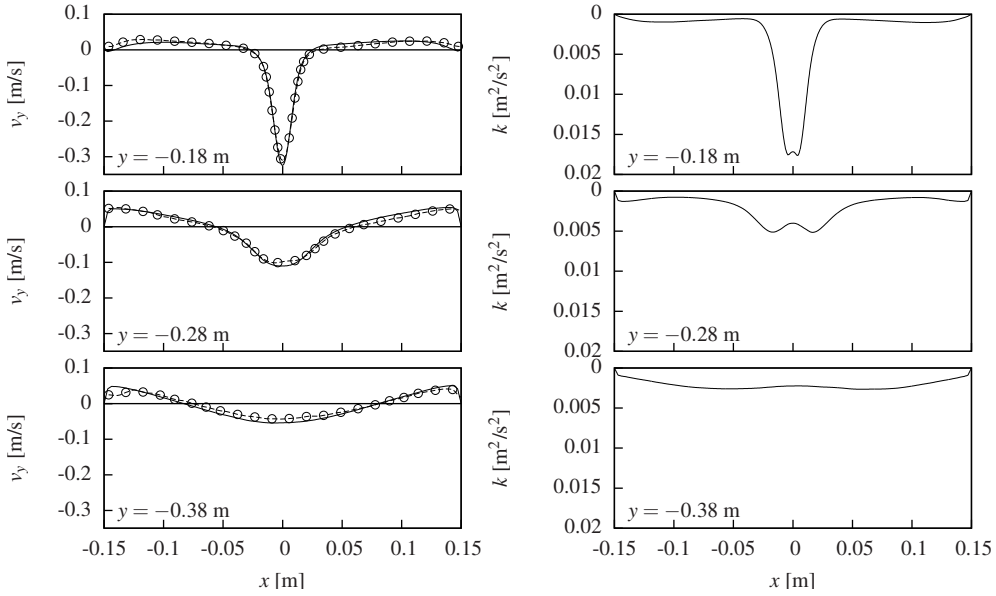


**Figure 4.4** (left) The vertical component of the mean velocity for  $Re = 4700$  and  $W/d = 30$  for the lines  $y = -0.18$  m,  $y = -0.28$  m and  $y = -0.38$  m, which is respectively 0.08 m, 0.18 m and 0.28 m below the nozzle exit for both the numerical simulation (solid red) and the experiments (dashed blue and circles, Kalter et al. <sup>10</sup>) (right) The turbulent kinetic energy obtained from the numerical simulations is shown for the same lines (red).

4.4 the vertical component of the mean velocity on three horizontal lines downstream from the nozzle is depicted. These comparisons show a good agreement between numerical and experimental mean velocities.

Figure 4.4 furthermore shows profiles of the turbulent kinetic energy obtained from the numerical simulations, where at each distance a double peak is observed, which is related to the long term oscillations of the jet in the cavity.

Figure 4.5 shows a time series of the jet angle for both the numerical simulations and the experiments. The dominant frequency of oscillation was determined at  $f = 0.022 \pm 0.001$  Hz for the simulations and  $f = 0.023 \pm 0.002$  Hz for the experiments. This leads to a Strouhal number  $St = fW/v_{in}$  of  $St = 0.011$ , which is in accordance with findings from literature. <sup>10</sup>



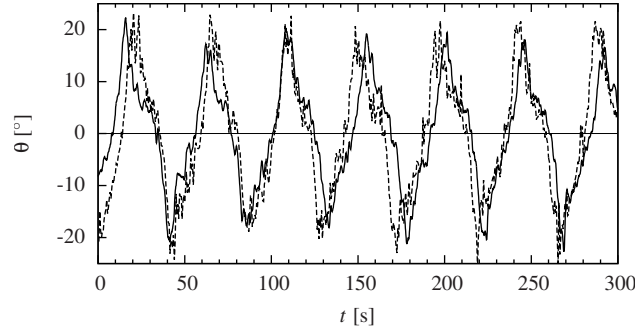


**Figure 4.5** Jet angle  $\theta(t)$  from the numerical simulation (solid red line) and from the PIV measurements (dashed blue line, from Kalter et al. <sup>10</sup>) for  $Re = 4700$  and  $W/d = 30$ .

## 4.4 Model for self-sustained oscillations of a jet in a confined cavity

### 4.4.1 Physical mechanisms

The physical mechanism of the stable self-sustained oscillation of a single jet in a closed, thin cavity has been described earlier to consist of three stages. <sup>10</sup> Initially, the jet flows straight to the bottom, forming two recirculation zones of equal size on both sides of the cavity. Then, due to a small, random pressure difference across the jet, it will move towards one side of the cavity (designated right in this section), after which the self-sustained oscillation is triggered.

In the first stage of the jet oscillation, the jet is oriented slightly to the right ( $\theta < 0$ ), which causes the recirculation zone at the right to be slightly stronger, due to its smaller diameter and higher velocities. This causes a larger pressure deficit in this recirculation zone, which draws the jet further towards the side, hence again creating a larger pressure deficit and further jet deflection.

Thus, the jet angle and pressure deficit in the recirculation zone are tightly coupled. We confirm this by means of our LES simulations. The time dependency of both the jet angle  $\theta$  and the pressure difference  $\Delta p$  across the jet, obtained from these simulations, is shown in Figure 4.6(left) for  $Re = 4700$ , where  $\Delta p$  was determined from the pressure difference,  $\Delta p = p_2 - p_1$  between the monitoring points  $p_1$  and  $p_2$ , as defined in Figure 4.1 and  $\theta$  is defined to be positive for jet deflections to the left.

It is seen from Figure 4.6(left), that  $\theta$  and  $\Delta p$  oscillate with the same period  $\mathcal{T} = 46$  s. The pressure signal is slightly ahead of the jet angle signal, especially during the sweeping motion of the jet far from its extreme positions. The cross correlation function (see Figure 4.6(right)) of both signals shows a peak around  $\Delta t = 2$  s, which means that the jet angle

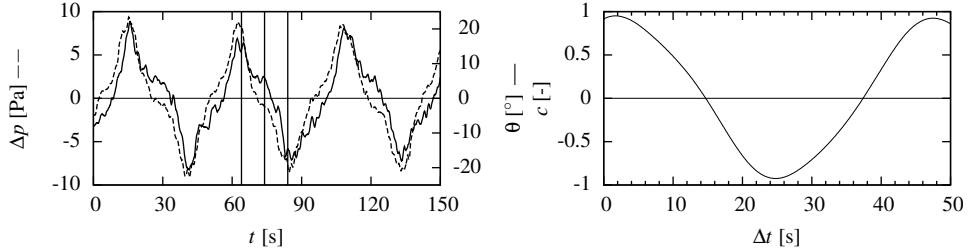


**Figure 4.6** (left) Time series of the pressure difference between monitoring point  $p_1$  and  $p_2$  (as defined in Figure 4.1) (dashed blue) and a time series of the jet angle  $\theta$  (solid red) for  $Re = 4700$ . The vertical lines indicate the time instances for the snap shots in Figure 4.2. (right) Cross correlation function between  $\Delta p$  and  $\theta$ .

follows the pressure difference with a small time delay of 2 s. At the extreme positions, other effects take over, and the phase difference is not clearly visible anymore. These observations and the found time delay were found to be rather insensitive to the choice of the location of probe-points  $p_1$  and  $p_2$ .

Next, in the second stage of the jet oscillation, the jet approaches the side wall and the recirculation zone can not shrink any further, because this would lead to a strongly non-circular recirculation zone with relatively high velocities, which becomes unphysical. At that moment, the maximum jet deflection  $\theta_{max}$  is reached. Now the driving mechanism in the increasing pressure deficit in the upper recirculation zone vanishes, and the driving motion for the jet deflection therefore also vanishes.

With reference to Figure 4.2(right) we can estimate  $\theta_{max}$ . In the extreme right position of the jet ( $\theta = -\theta_{max}$ ), a recirculation zone of diameter  $W/2$  is present in the upper right corner, and a second adjacent recirculation zone of diameter  $W$  lower in the cavity. Now, for the angle  $\theta$  between the vertical and the line connecting the nozzle exit with the tangent point of the two recirculation zones, we find from simple geometrical considerations<sup>1</sup>  $\tan(\theta) = \left(\frac{3}{2} + \sqrt{2}\right)^{-1}$ , or  $\theta \approx 19^\circ$ .

Indeed, in our simulations, we find a constant  $\theta_{max} = 18^\circ$  independent of  $Re$  for a wide range of  $W/d$ . In Figure 4.7 both a time series and a phase averaged jet angle are shown for Reynolds numbers between  $Re = 3150$  and  $Re = 7100$ . The jet angle amplitude is almost independent of  $Re$ . The oscillation frequency, however, differs significantly, with periods increasing roughly inversely proportional with  $Re$ , from  $\mathcal{T} = 31$  s to  $\mathcal{T} = 59$  s upon decreasing  $Re$  from 7100 to 3150. This is in accordance with the constant Strouhal number behavior as determined by Kalter et al.<sup>10</sup> In Figure 4.8,  $W/d$  is varied between 10 and 50. The frequency of oscillation increases with decreasing  $W/d$ , in correspondence with findings of Lawson and Davidson<sup>14</sup>. It should be noted that  $W/d = 10$  is the geometry ratio previously studied by Villermaux and Hopfinger<sup>31</sup>. The amplitude  $\theta_{max}$  of the oscillation is only weakly dependent on  $W/d$  for  $W/d \geq 20$ .

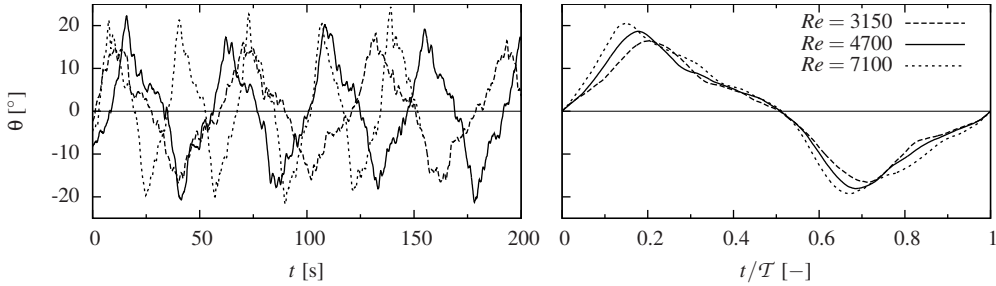


**Figure 4.7** (left) Time series of the jet angle  $\theta$  and (right) phase average jet angle profile normalized by the period  $\mathcal{T}$ , for  $Re = 3150$  (dashed red),  $Re = 4700$  (solid blue) and  $Re = 7100$  (long-dashed green) with period  $\mathcal{T} = 59$  s,  $\mathcal{T} = 46$  s and  $\mathcal{T} = 31$  s respectively.

Finally, the third and final stage starts when the jet oscillation has reached its maximum deflection angle and the jet impinges on the side wall. This causes a division of flow between an upper, strong recirculation zone and a downward directed flow along the wall. The downward flow along the right wall starts to feed a recirculation zone in the lower left part of the cavity. This new recirculation zone is visible in Figure 4.2(right). The diminishing flow rate in the upper recirculation zone results in a smaller pressure deficit in the centre of the upper recirculation zone. Simultaneously, the secondary recirculation zone lower in the cavity starts to grow in strength. Less fluid is fed to the recirculation zone in the upper right part of the cavity, which causes the pressure deficit inside the upper right recirculation zone to quickly decrease. The jet will not remain in its extreme position,  $-\theta_{max}$ , but will move downward and subsequently towards the left, with  $\theta$  returning to 0, as follows from Figure 4.6. The decay of the strong recirculation zone is associated with a delay time scale  $\tau$ , which plays a crucial

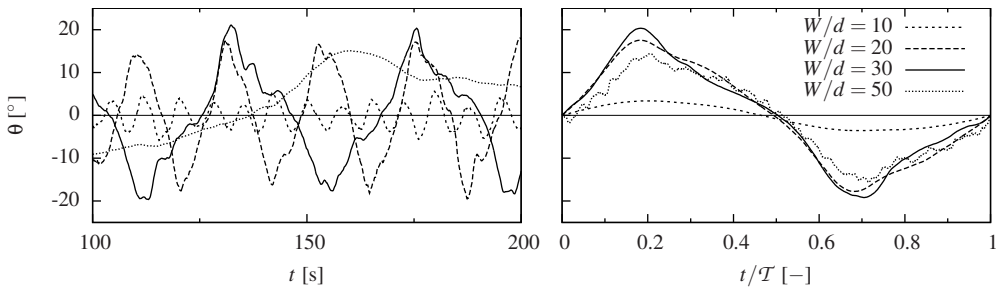


**Figure 4.8** (left) Time series of the jet angle  $\theta(t)$  and (right) phase average jet angle profile, with the time-axis scaled by the period  $\mathcal{T}$ , for  $Re = 4700$  and  $W/d = 10$  (dashed red),  $W/d = 20$  (long-dashed green),  $W/d = 30$  (solid blue) and  $W/d = 50$  (short-dashed turquoise), and  $\mathcal{T} = 7.5$  s,  $\mathcal{T} = 22$  s,  $\mathcal{T} = 43$  s and  $\mathcal{T} = 1.8 \times 10^2$  s respectively.

role in the self-sustained nature of the oscillation. As the jet crosses the vertical at  $\theta = 0$ , the first stage re-starts. This self-sustained oscillation repeats itself indefinitely.

#### 4.4.2 Model description

In this section, we propose a zero-dimensional model for the self-sustained jet oscillation in a confined cavity based on the relevant physical mechanisms. We start from the horizontal component of the Navier-Stokes equations,

$$\frac{\partial v_x}{\partial t} + v_x \frac{\partial v_x}{\partial x} + v_y \frac{\partial v_x}{\partial y} = -\frac{1}{\rho} \frac{\partial p}{\partial x} + \nu \frac{\partial^2 u_x}{\partial x^2} + \nu \frac{\partial^2 u_x}{\partial y^2}. \quad (4.2)$$

Neglecting the viscous terms in this equation due to the high Reynolds number of the flow, we show that on the left hand side of this equation, the third term is dominant. Firstly,  $v_x$  is estimated from the jet oscillation, i.e.  $v_x \sim -S \frac{\partial \theta}{\partial t} \sim -\frac{S \theta_{max}}{\mathcal{T}}$ , and  $v_y$  is estimated from  $v_y \sim v_{in}$ . An order of magnitude analysis leads to

$$\frac{\frac{\partial v_x}{\partial t}}{v_y \frac{\partial v_x}{\partial y}} \sim \frac{\frac{S \theta_{max}}{\mathcal{T}^2}}{v_{in} \frac{S \theta_{max}}{\mathcal{T} S}} \sim \frac{S}{v_{in} \mathcal{T}}, \quad \frac{v_x \frac{\partial v_x}{\partial x}}{v_y \frac{\partial v_x}{\partial y}} \sim \frac{\frac{S^2 \theta_{max}^2}{\mathcal{T}^2 W}}{v_{in} \frac{S \theta_{max}}{\mathcal{T} S}} \sim \frac{S^2 \theta_{max}}{v_{in} \mathcal{T} W}. \quad (4.3)$$

Observing from Figure 4.2 that  $S \sim W$  and using the observation that  $St = W/(v_{in} \mathcal{T}) \ll 1$ , we now find that

$$\frac{\frac{\partial v_x}{\partial t}}{v_y \frac{\partial v_x}{\partial y}} \sim St \ll 1, \quad \frac{v_x \frac{\partial v_x}{\partial x}}{v_y \frac{\partial v_x}{\partial y}} \sim St \theta_{max} \ll 1. \quad (4.4)$$

From Equation 4.2 two leading terms remain:

$$v_y \frac{\partial v_x}{\partial y} \sim -\frac{1}{\rho} \frac{dp}{dx}, \quad (4.5)$$

which can be rewritten using the above expressions for  $v_x$  and  $v_y$ , and recalling  $\Delta p = p_2 - p_1$ , to

$$\frac{d\theta}{dt} \propto \frac{1}{\rho v_{in} W} \Delta p. \quad (4.6)$$

From Figure 4.6 we observed that  $\theta$  and  $\Delta p$  are tightly coupled. Hence we may pose

$$\Delta p \propto \theta. \quad (4.7)$$

Now, combining equations 4.6 and 4.7, we find that, during the growing stage of the jet oscillation,

$$\frac{d\theta}{dt} = r\theta, \quad (4.8)$$

where  $r$  is the growth rate of the jet oscillation. This expression is not a sufficient description for the time evolution of the jet behaviour, as it does not incorporate the maximum achievable jet angle and consecutive decay of the upper recirculation zone.

The maximum achievable jet angle acts as a damping mechanism on the self-excited jet oscillation, as it prevents unlimited growth of the jet angle. Hence, we introduce an obstruction parameter,  $\mu$ , and introduce a damping term in Equation 4.8,

$$\frac{d}{dt}\theta = (r - \mu\theta^2)\theta. \quad (4.9)$$

The third order of the damping term in  $\theta$  is chosen as the lowest possible order which is (i) higher than the order of the leading forcing term, and (ii) able to maintain symmetry of the model equation. The equation now has three equilibrium points, namely  $\theta = 0$ , which is unstable, and  $\theta = \pm\sqrt{r/\mu}$ , which are stable equilibria. Thus, the value of the obstruction parameter  $\mu$  is related to the growth rate parameter  $r$  and to the maximum deflection angle  $\theta_{max}$  as  $\mu = r/\theta_{max}^2$ . Later we show that the inclusion of the feedback term in the model, as discussed below, leads to a small correction in  $\mu$ .

As described above, the delay time  $\tau$  is associated with the decay time of the strong recirculation zone, eventually restoring the jet angle  $\theta$ . This is represented in the model Equation 4.10 by the negative feedback term, with a feedback strength  $k$ , and  $k < r$ . The delay time  $\tau$  is of the order of the turnover time of the recirculation zone, which scales with  $W/v_{in}$ . Later we will show that it is also weakly dependent on  $Re$ .

This leads to the full model equation

$$\frac{d}{dt}\theta(t) = r\theta(t) - \mu\theta^3(t) - k\theta(t - \tau), \quad (4.10)$$

where  $r$ ,  $\mu$ ,  $k$  and  $\tau$  are the model parameters described above. This is an example of a retarded delay differential equation<sup>12</sup> and is also referred to as delayed-action oscillator. In this form it is used for example in the description of the El Niño oscillation.<sup>3,28</sup> The three terms on the right hand side of the equation can be associated with the three stages in the oscillating motion as described above.

## 4.5 Determination of model parameters and its implications

We now discuss how the four model parameters  $r$ ,  $\mu$ ,  $k$  and  $\tau$  in Equation 4.10 can be predicted *a priori*, as a function of  $Re$  and  $W/d$ . From LES simulations at given  $W/d$  and  $Re$ , we computationally determine the best fitting parameter set  $\{r, \mu, k, \tau\}$ , by applying the Nelder-Mead simplex method<sup>21</sup> on the phase-averaged jet angle. This procedure is further outlined in appendix 4.A.

Figure 4.9 shows the phase-averaged jet angle from LES, for different  $Re$  and  $W/d$ , in conjunction with the DDE model predictions, using the values of  $r$ ,  $\mu$ ,  $k$  and  $\tau$  as optimized and indicated for each separate case. The thus obtained solutions of the model equation are in good agreement with the jet angle from the LES simulation, except for the inflexion points

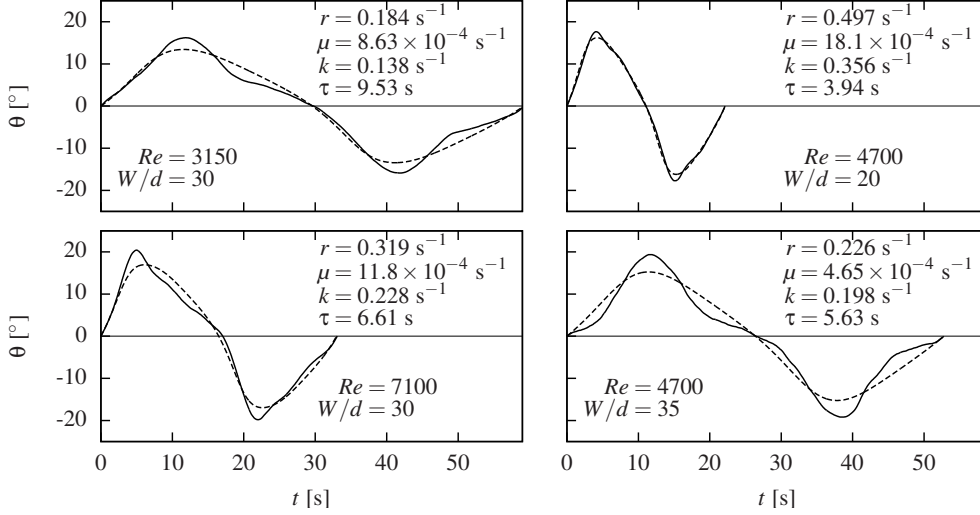


**Figure 4.9** Phase averaged jet angle profile from the LES simulations (solid red) and from the DDE model (dashed blue), for four cases with different Reynolds numbers and cavity widths. The model parameters  $r$ ,  $\mu$ ,  $k$  and  $\tau$  obtained from the fitting procedure are shown per figure.

observed in the LES simulation that are not reproduced by the DDE model and which are probably due to higher order non-linear effects not taken into account in the model.

#### 4.5.1 Reduced parameters

The non-linear delay model for a single jet in a confined cavity (Equation 4.10) contains four constants, viz.  $r$ ,  $\mu$ ,  $k$  and  $\tau$ . In terms of a dimensionless time  $t' = rt$  and a scaled jet angle  $\theta' = \sqrt{\mu/r}\theta$ , the behavior of the model, however, is determined by only two independent parameters,  $\alpha = k/r$  and  $\delta = r\tau$ :

$$\frac{d\theta'}{dt'} = \theta' - \theta'^3 - \alpha\theta'(t' - \delta). \quad (4.11)$$

Here  $\alpha$  denotes the relative strength of the feedback mechanism compared to the growth rate, and  $\delta$  denotes the dimensionless delay time. Thus, as an alternative to  $r$ ,  $\mu$ ,  $k$ ,  $\tau$ , the model Equation 4.10 can also be defined in terms of  $\alpha$ ,  $\delta$ ,  $\mu$ ,  $\tau$ . From a linear stability analysis of Equation 4.11, its neutral curve  $\delta_n$  can be derived,<sup>28</sup>

$$\delta_n(\alpha) = \arccos\left(\frac{3\alpha - 2}{\alpha}\right) (\alpha^2 - (3\alpha - 2)^2)^{-\frac{1}{2}}. \quad (4.12)$$

For  $\delta < \delta_n(\alpha)$ , the oscillations vanish. The behavior of Equation 4.11 for  $\alpha < 1$  is described by Suarez and Schopf<sup>28</sup>. They showed that the shape of the oscillation is sinusoidal close to

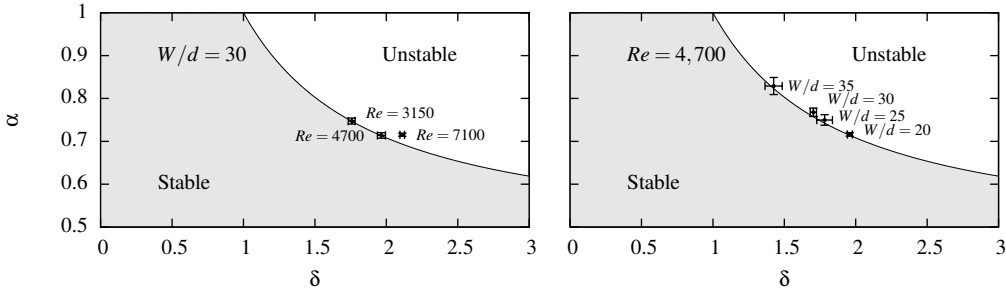


**Figure 4.10** The neutral curve (Equation 4.12) of the reduced model (Equation 4.11), where the shaded region depicts the region of stability, while the white region depicts the unstable modes. The parameter values for  $Re = 3150$  up to  $Re = 7100$  and  $W/d = 30$  (left) and for  $W/d = 20$  up to  $W/d = 50$  and  $Re = 4700$  (right) are depicted in this diagram. The error bars in these graphs indicate the accuracy in the fit, see appendix 4.A for details.

the neutral curve  $\delta = \delta_n(\alpha)$ , while for  $\delta \geq 10$ , the oscillation reaches a block wave with a period of oscillation of twice the delay time.

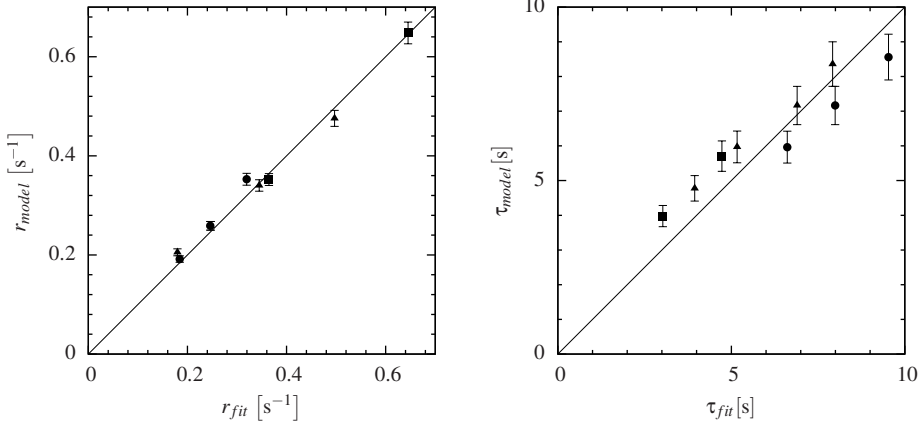
The jet oscillations studied in this paper, see Figures 4.7(right) and 4.8(right), are of a sinusoidal nature, leading to the expectation that apparently the parameters  $\alpha$  and  $\delta$  in Equation 4.11 should be close to the neutral curve. This is indeed the case. Combinations of  $\alpha$  and  $\delta$  far above the critical curve were not observed for any studied combination of  $W/d$  and  $Re$  and seem to be unphysical for the studied flows.

Figure 4.10 shows the neutral curve, Equation 4.12, in conjunction with the found optimal values for  $\alpha$  and  $\delta$  for different sets of  $Re$  and  $W/d$ . Indeed, the best fit parameters all reside on, or very close to, the neutral curve. In other words, the number of parameters in the model can be reduced by one, to  $\delta, \mu, \tau$ , by application of Equation 4.12 which relates  $\delta$  to  $\alpha$ . From Figure 4.10, it is also observed that  $\alpha$ , i.e. the relative strength of the feedback compared to the initial growth rate, decreases for increasing  $Re$ , whereas  $\alpha$  increases for increasing  $W/d$ .

The parameter set can be further reduced by using a relation between  $\mu$  and  $\theta_{max}$ . Without the feedback term it was derived that  $\theta_{max} = \sqrt{r/\mu}$ . By including the feedback term however, the maximum jet angle should be slightly corrected, as for  $\alpha$  and  $\delta$  close to the neutral curve, it was found that  $\theta'_{max} = \sqrt{2(1 - \alpha^2)}$ , and thus

$$\mu = \frac{2r(1 - \alpha^2)}{\theta_{max}^2}. \quad (4.13)$$

Herewith it is demonstrated that the parameter set  $\{r, \mu, k, \tau\}$  can be reduced to  $\{r, \tau\}$  by making use of relations 4.12 and 4.13 with  $\alpha = k/r$  and  $\delta = r\tau$ .



**Figure 4.11** Parity plot for  $r$  (left) and  $\tau$  (right) following from the fit (horizontal axis) and the model (vertical axis, equations 4.15), for different  $Re$  (red circles for  $W/d = 30$  and green squares for  $W/d = 20$ ) and  $W/d$  (blue triangles for  $Re = 4700$ ).

#### 4.5.2 Parameter estimation

From dimensional arguments  $r$  and  $\tau$  are expected to scale as

$$r = \kappa_1 \frac{v_{in}}{W} f \left( Re, \frac{W}{d}, \frac{H}{d}, \frac{d_n}{d}, \frac{T}{d} \right), \quad \tau = \kappa_2 \frac{W}{v_{in}} g \left( Re, \frac{W}{d}, \frac{H}{d}, \frac{d_n}{d}, \frac{T}{d} \right). \quad (4.14)$$

From our LES simulations for varying  $Re$  ( $1600 < Re < 7100$ ),  $W/d$  ( $20 \leq W/d < 50$ ),  $T/d$  ( $3 \leq T/d < 6$ ),  $H/d$  ( $70 \leq H/d \leq 100$ ) and  $d_n/d$  ( $10 \leq d_n/d \leq 25$ ), we find that  $f = f(Re, W/d)$  and  $g = g(Re, W/d)$ , both being independent of  $T/d$ ,  $H/d$  and  $d_n/d$  for the studied range.

From a consecutive fitting procedure of the parameters, we determined  $r$  and  $\tau$  as a function of  $v_{in}$ ,  $W$ ,  $Re$  and  $W/d$ , as

$$r = \kappa_1 \frac{v_{in}}{W} Re^{-\frac{1}{4}} \left( \frac{W}{d} \right)^{-\frac{1}{2}}, \quad \tau = \kappa_2 \frac{W}{v_{in}} Re^{\frac{5}{3}}, \quad (4.15)$$

with  $\kappa_1 = 5.9 \pm 0.2$  and  $\kappa_2 = 0.13 \pm 0.01$ .

Figure 4.11 compares the results of the fit with the model estimation for the parameters  $r$  and  $\tau$  (Equation 4.15), showing a good agreement of our model with the parameters obtained from the LES simulations.



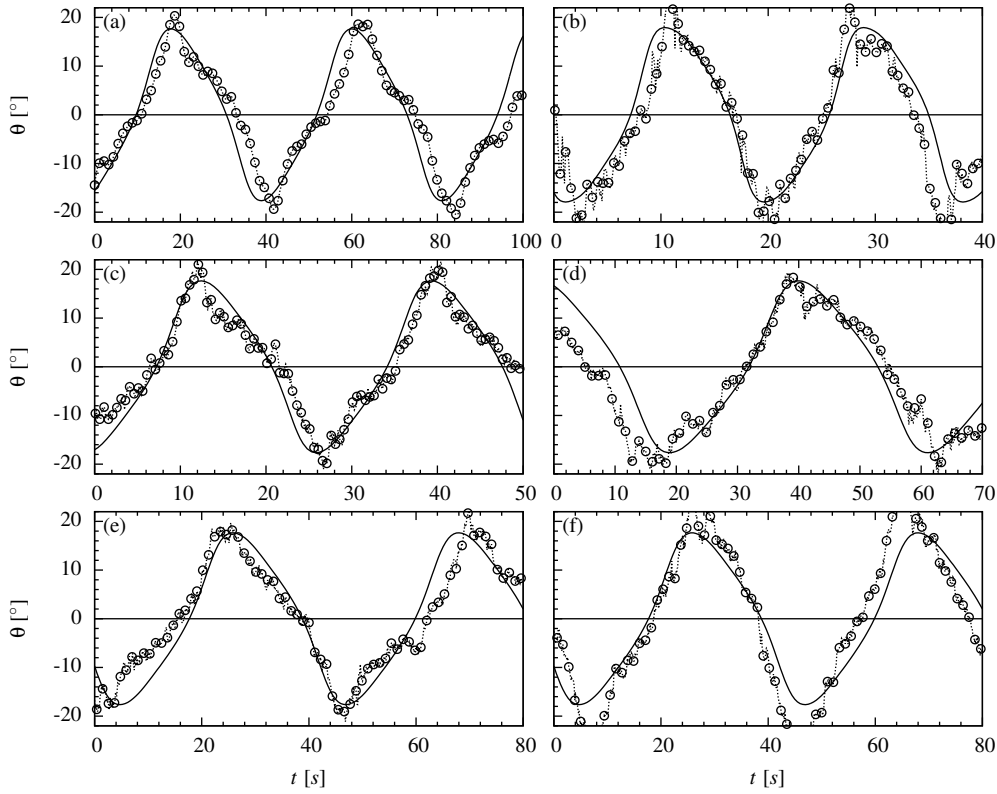


**Figure 4.12** Example model solutions (solid lines) and  $\theta$  obtained from the numerical simulations (symbols and dashed lines). Unless stated otherwise,  $T/d = 3.5$ ,  $d_n/d = 10$ ,  $H/d = 70$  (for  $W/d < 50$ ) and  $H/d = 2.5W/d$  (for  $W/d \geq 50$ ) and  $\nu = 1.0 \times 10^{-6} \text{ m}^2/\text{s}$  (a)  $Re = 4700$  and  $W/d = 30$ , (b)  $Re = 7100$  and  $W/d = 20$ , (c)  $Re = 4700$ ,  $W/d = 30$ ,  $\nu = 2.0 \times 10^{-6} \text{ m}^2/\text{s}$  and  $\nu_{in}$  changed accordingly to satisfy  $Re = 4700$ , (d)  $Re = 4700$ ,  $W/d = 30$ ,  $T/d = 5.0$ , (e)  $Re = 4700$ ,  $W/d = 30$ ,  $H/d = 100$ , (f)  $Re = 4700$ ,  $W/d = 30$ ,  $d_n/d = 25$ .

### 4.5.3 Model application

Validations of the presented model (Equation 4.10 with  $r$ ,  $\tau$ ,  $\mu$ ,  $k$  obtained from equations 4.12, 4.13 and 4.15), are shown in Figure 4.12 for  $Re = 4700$  and  $W/d = 30$ , and  $Re = 7100$  and  $W/d = 20$ . The figure demonstrates the applicability of the present model for the prediction of the jet angle oscillation in a confined cavity for liquids of different viscosity and the independence of the model constants on  $T/d$ ,  $H/d$  and  $d_n/d$  for the studied ranges.

Of course, the frequency of an oscillating jet in a confined cavity for all  $Re$  and  $W/d$  may simply be calculated from the observed constant Strouhal number,  $St = 0.011$ . However, for

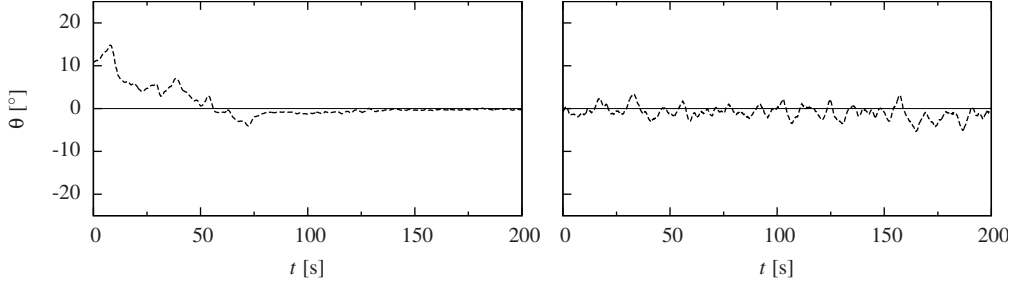


**Figure 4.13** The jet angle  $\theta(t)$  for (left)  $Re = 900$  and  $W/d = 30$ , initialized with the oscillating flow field for  $Re = 1600$  and (right)  $Re = 4700$  and  $W/d = 100$ , initialized with zero velocity in the domain.

sufficiently wide cavities, these oscillations are not present.<sup>13,18</sup> From Figure 4.10 it follows that the system is stable for  $\delta < 1$ . As  $\delta = r\tau$ , an approximate relation between the critical Reynolds number and the width to nozzle diameter ratio can be found:

$$Re_{crit} = \kappa_3 \left( \frac{W}{d} \right)^{\frac{18}{11}}, \quad (4.16)$$

with  $\kappa_3 = (\kappa_1 \kappa_2)^{-36/11} = 2.4 \pm 0.7$ . This implies that

1. for certain  $W/d$  there is a  $Re_{crit}$ , below which oscillations cease and
2. for certain  $Re$ , there is a  $(W/d)_{crit}$ , above which oscillations cease.

The ceasing of the oscillations is demonstrated in Figure 4.13, which shows the jet angle for  $Re = 900$  and  $W/d = 30$  and for  $Re = 4700$  and  $W/d = 100$ . According to the above  $Re_{crit}$ , the oscillations of the jet angle should vanish for these conditions, and indeed, no periodic jet oscillations are observed.

In table 4.1, we summarize, for the cases in Figures 4.12 and 4.13,  $r$ ,  $\tau$ ,  $Re_{crit}$ ,  $(W/d)_{crit}$  as well as frequencies following from  $St = 0.011$ , the LES simulation, the experiments by Kalter et al. and the DDE model. From this table, it also follows why the oscillations vanish. The growth rate of the supposed jet angle oscillation becomes very weak, such that a possible deflection of the jet does not get amplified significantly.

The stable and oscillating modes listed in table 4.1 are summarized in a flow stability diagram in Figure 4.14 in conjunction with the critical curve (Equation 4.16).

**Table 4.1** For given  $Re$  and  $W/d$ ,  $r$  and  $\tau$  (eq. 4.15) are calculated. Furthermore, using Equation 4.16,  $Re_{crit}$  is calculated based on  $W/d$ . The last four columns indicate the oscillation frequency, based on  $St = 0.011$ , the LES model, the experiments by Kalter et al.<sup>10</sup> and the zero-dimensional model respectively. Unless stated otherwise,  $H/d = 70$  (for  $W/d < 50$ ) and  $H/d = 2.5W/d$  (for  $W/d \geq 50$ ),  $d_n/d = 10$ ,  $T/d = 3.5$  and  $\nu = 1.27 \times 10^{-6} \text{ m}^2/\text{s}$ .

$Re$	$W/d$	$r \text{ [s}^{-1}\text{]}$	$\tau \text{ [s]}$	$Re_{crit}$	$f_{St} \text{ [Hz]}$	$f_{LES} \text{ [Hz]}$	$f_{exp} \text{ [Hz]}$	$f_{model} \text{ [Hz]}$
500	30	0.05	19.2	$\sim 900$	0.0023		no oscillations	$Re \leq Re_{crit}$
900	30	0.06	14.9	$\sim 900$	0.0042	no oscillations		$Re \leq Re_{crit}$
1600	30	0.11	11.6	$\sim 900$	0.0073	$0.0098 \pm 0.004$		0.0095
1600	50	0.09	11.8	$\sim 2000$	0.0044	no oscillations		$Re \leq Re_{crit}$
3150	20	0.35	5.71	$\sim 400$	0.022	$0.034 \pm 0.003$		0.032
3150	30	0.19	8.56	$\sim 900$	0.015	$0.017 \pm 0.001$	0.014	0.018
4700	20	0.48	4.75	$\sim 400$	0.033	$0.045 \pm 0.002$		0.042
4700	25	0.34	5.94	$\sim 600$	0.026	$0.032 \pm 0.002$		0.031
4700	30	0.26	7.11	$\sim 900$	0.022	$0.022 \pm 0.001$	0.022	0.024
4700	35	0.21	8.32	$\sim 1100$	0.019	$0.015 \pm 0.002$		0.019
4700	50	0.12	11.9	$\sim 2000$	0.013	$0.006 \pm 0.002$		0.011
4700	100	0.04	23.8	$\sim 6000$	0.0066	no oscillations		$Re \leq Re_{crit}$
7100	20	0.65	3.98	$\sim 400$	0.050	$0.059 \pm 0.005$		0.054
7100	30	0.35	5.98	$\sim 900$	0.033	$0.031 \pm 0.002$	0.035	0.031
10000	30	0.46	5.12	$\sim 900$	0.047		0.042	0.039
4700	30	0.41	4.55	$\sim 900$	0.034	$0.035 \pm 0.002$		0.037 <sup>1</sup>
4700	30	0.26	7.11	$\sim 900$	0.022	$0.020 \pm 0.003$		0.024 <sup>2</sup>
4700	30	0.26	7.11	$\sim 900$	0.022	$0.021 \pm 0.003$		0.024 <sup>3</sup>
4700	30	0.26	7.11	$\sim 900$	0.022	$0.024 \pm 0.004$		0.024 <sup>4</sup>

<sup>1</sup>  $\nu = 2.0 \times 10^{-6} \text{ m}^2/\text{s}$ ; <sup>2</sup>  $T/d = 5.0$ ; <sup>3</sup>  $H/d = 100$ ; <sup>4</sup>  $d_n/d = 25$

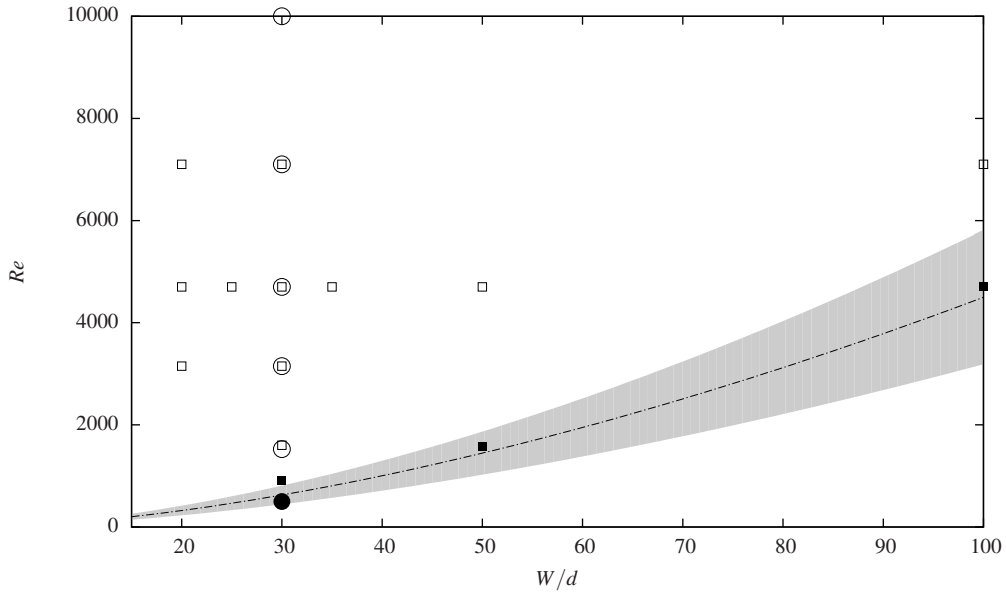


**Figure 4.14** Flow stability as a function of  $Re$  and  $W/d$  for simulations (squares) and experiments (circles). Oscillatory flows are indicated by open symbols, non-oscillating flow by closed symbols. The critical Reynolds number predicted by the DDE model, with its uncertainty, is depicted by the solid line and grey area respectively. Oscillatory flows are expected for  $Re > Re_{crit}$ . For all symbols  $T/d = 3.5$ ,  $d_n/d = 10$  and  $\nu = 1.27 \times 10^{-6} \text{ m}^2/\text{s}$ .

## 4.6 Conclusion

We studied the dynamics of the self-sustained oscillation of a turbulent jet in a confined cavity. We presented a zero-dimensional DDE-type model that describes the oscillation of the jet angle in such a system. The model includes the three consecutive phases of the jet oscillation, which are the pressure driven growth of the oscillation, the limited amplitude due to the confinement, and the delayed destruction of the pressure deficit in the recirculation zone by a feedback loop. These phases are described by their respective terms in a delay differential equation with four parameters. We showed that the dimensionless behavior of the model can be properly represented by just two parameters, which are the growth rate of the oscillation,  $r$ , and the delay time,  $\tau$ , for the destruction of the strong recirculation zone adjacent to the oscillating jet. Closed relations have been proposed for both parameters as a function of the jet Reynolds number  $Re$ , the inlet velocity  $v_{in}$ , the cavity width  $W$  and the cavity width to nozzle diameter ratio  $W/d$ . For the studied ranges ( $3 < T/d < 6$ ),  $70 < H/d < 100$ ,  $10 < d_n/d < 25$ ) both model parameters are independent of these geometry ratios.

The model displays the correct oscillation behavior of the jet across the domain for ranges of at least  $1600 < Re < 7100$  and  $20 \leq W/d < 50$  when these are compared with three dimensional Large Eddy Simulations. The model also describes that jet oscillations vanish for Reynolds numbers below a critical value, and  $W/d$  above a critical value, which both can be predicted a priori. As this model includes the prediction of stable modes, it can be of interest for all kinds of industrial applications where the stabilization of oscillating flows is relevant. This model also offers perspective for pressure dominated oscillations in multi-jet configurations and more irregular oscillations, by additionally introducing two oscillators and multiple delay terms, respectively.

## Acknowledgement

This work was supported by the Dutch Technology Foundation STW, Tata Steel, and ABB. We thank SURFsara for the support in using the Lisa Compute Cluster, project code MP-235-12. We thank Jasper Hollander for his assistance in the initial set-up of the numerical simulations.

## Bibliography

- [1] supplemental material at [...] for the geometrical derivation of the maximum jet angle, S. ().
- [2] Bouchet, G. and Climent, E. Unsteady behavior of a confined jet in a cavity at moderate Reynolds numbers. *Fluid Dynamics Research*, volume 44(2):p. 025505 (2012).
- [3] Boutle, I., Taylor, R. H. S., and Römer, R. A. El Niño and the delayed action oscillator. *American Journal of Physics*, volume 75(1):pp. 15–24 (2007).
- [4] Drikakis, D. Bifurcation phenomena in incompressible sudden expansion flows. *Physics of Fluids*, volume 9(1):pp. 76–87 (1997).
- [5] Duprat, C., Balarac, G., Métais, O., Congedo, P. M., and Brugière, O. A wall-layer model for large-eddy simulations of turbulent flows with/out pressure gradient. *Physics of Fluids*, volume 23(1):p. 015101 (2011).
- [6] Escudier, M. P., Oliveira, P. J., and Poole, R. J. Turbulent flow through a plane sudden expansion of modest aspect ratio. *Physics of Fluids*, volume 14(10):pp. 3641–3654 (2002).
- [7] Fearn, R. M., Mullin, T., and Cliffe, K. A. Nonlinear flow phenomena in a symmetric sudden expansion. *Journal of Fluid Mechanics*, volume 211:pp. 595–608 (1990).
- [8] Issa, R. I. Solution of the implicitly discretised fluid flow equations by operator-splitting. *Journal of Computational Physics*, volume 62(1):pp. 40–65 (1986).
- [9] Jones, W. P. Turbulence modelling and numerical solution methods for variable density and combusting. In Libby, P. A. and Williams, F. A., editors, *Turbulent Reacting Flows*, pp. 309–374. Academic Press Inc. (1994).
- [10] Kalter, R., Tummers, M. J., Kenjereš, S., Righolt, B. W., and Kleijn, C. R. Effects of electromagnetic forcing on self-sustained jet oscillations. *Physics of Fluids*, volume 26(6):p. 065101 (2014).
- [11] Kolšek, T., Jelić, N., and Duhovnik, J. Numerical study of flow asymmetry and self-sustained jet oscillations in geometrically symmetric cavities. *Applied Mathematical Modelling*, volume 31(10):pp. 2355–2373 (2007).

- [12] Lakshmanan, M. and Senthilkumar, D. V. *Dynamics of Nonlinear Time-Delay Systems*. Springer, Berlin, Heidelberg (2010).
- [13] Landel, J. R., Caulfield, C. P., and Woods, A. W. Meandering due to large eddies and the statistically self-similar dynamics of quasi-two-dimensional jets. *Journal of Fluid Mechanics*, volume 692:pp. 347–368 (2012).
- [14] Lawson, N. and Davidson, M. Self-Sustained Oscillation of a Submerged Jet in a Thin Rectangular Cavity. *Journal of Fluids and Structures*, volume 15(1):pp. 59–81 (2001).
- [15] Lilly, D. K. A proposed modification of the Germano subgrid-scale closure method. *Physics of Fluids A: Fluid Dynamics*, volume 4(3):p. 633 (1992).
- [16] Mackey, M. C. and Glass, L. Oscillation and chaos in physiological control systems. *Science*, volume 197(4300):pp. 287–289 (1977).
- [17] Martín-Alcántara, A., Sanmiguel-Rojas, E., Gutiérrez-Montes, C., and Martínez-Bazán, C. Drag reduction induced by the addition of a multi-cavity at the base of a bluff body. *Journal of Fluids and Structures*, volume 48:pp. 347–361 (2014).
- [18] Mataoui, A. and Schiestel, R. Unsteady phenomena of an oscillating turbulent jet flow inside a cavity: Effect of aspect ratio. *Journal of Fluids and Structures*, volume 25(1):pp. 60–79 (2009).
- [19] Maurel, A., Ern, P., Zielinska, B. J. A., and Wesfreid, J. E. Experimental study of self-sustained oscillations in a confined jet. *Physical Review E*, volume 54(4):pp. 3643–3651 (1996).
- [20] Molloy, N. A. and Taylor, P. L. Oscillatory Flow of a Jet into a Blind Cavity. *Nature*, volume 224(5225):pp. 1192–1194 (1969).
- [21] Nelder, J. A. and Mead, R. A Simplex Method for Function Minimization. *The Computer Journal*, volume 7(4):pp. 308–313 (1965).
- [22] Powell, A. On the Edgetone. *The Journal of the Acoustical Society of America*, volume 33(4):pp. 395–409 (1961).
- [23] Rockwell, D. and Naudascher, E. Self-Sustained Oscillations of Impinging Free Shear Layers. *Annual Review of Fluid Mechanics*, volume 11(1):pp. 67–94 (1979).
- [24] Rowley, C. W., Colonius, T., and Basu, A. J. On self-sustained oscillations in two-dimensional compressible flow over rectangular cavities. *Journal of Fluid Mechanics*, volume 455:pp. 315–346 (2002).
- [25] Shakouchi, T. New fluidic oscillator, flowmeter, without control port and feedback loop. *Journal of Dynamic Systems, Measurement and Control, Transactions of the ASME*, volume 111(3):pp. 535–539 (1989).
- [26] Shampine, L. F. and Thompson, S. Solving DDEs in Matlab. *Applied Numerical Mathematics*, volume 37(4):pp. 441–458 (2001).
- [27] Spalding, D. B. A single formula for the law of the wall. *Journal of Applied Mechanics*, volume 28:pp. 455–458 (1961).
- [28] Suarez, M. and Schopf, P. A delayed action oscillator for ENSO. *Journal of the Atmospheric Sciences*, volume 45(21):pp. 3283–3287 (1988).
- [29] Szydłowski, M., Krawiec, A., and Tobola, J. Nonlinear oscillations in business cycle model with time lags. *Chaos, solitons and fractals*, volume 12(3):pp. 505–517 (2001).
- [30] Villiermaux, E. Memory-Induced Low Frequency Oscillations in Closed Convection Boxes. *Physical Review Letters*, volume 75(25):pp. 4618–4621 (1995).
- [31] Villiermaux, E. and Hopfinger, E. Self-sustained oscillations of a confined jet: a case study for the non-linear delayed saturation model. *Physica D: Nonlinear Phenomena*, volume 72(3):pp. 230–243 (1994).
- [32] de Villiers, E. *The Potential of Large Eddy Simulation for the Modeling of Wall Bounded Flows*. PhD thesis, Imperial College, London (2006).
- [33] Vuorinen, V., Keskinen, J. P., Duwig, C., and Boersma, B. J. On the implementation of low-dissipative Runge-Kutta projection methods for time dependent flows using OpenFOAM. *Computers & Fluids*,

volume 93:pp. 153–163 (2014).

- [34] Weller, H. G., Tabor, G., Jasak, H., and Fureby, C. A tensorial approach to computational continuum mechanics using object-oriented techniques. *Computers in Physics*, volume 12(6):pp. 620–631 (1998).
- [35] Zang, Y., Street, R. L., and Koseff, J. R. A dynamic mixed subgrid-scale model and its application to turbulent recirculating flows. *Physics of Fluids A: Fluid Dynamics*, volume 5(12):pp. 3186–3196 (1993).

## 4.A A posteriori determination of the model parameters

The proposed model (Equation 4.10) for the jet oscillation comprises four unknowns, the growth factor  $r$ , the obstruction factor  $\mu$ , the delay time  $\tau$  and the delay strength  $k$ . These parameters can be obtained from fitting the solution of Equation 4.10 with a realization of the jet angle as a function of time. The fitting procedure for obtaining  $r$ ,  $\mu$ ,  $k$  and  $\tau$  is as follows and is calculated using MATLAB-R2013b.

1. Calculation of the phase average of  $\theta(t)$ .
2. Loop over different sets  $\{r, \mu, k, \tau\}$  of initial conditions.
  - (a) Calculate phase of periodic solution by solving Equation 4.10 for one or more sets of  $\{r, \mu, k, \tau\}$  using Matlab's `dde23` routine.<sup>26</sup> This routine is able to solve (systems of) non-linear differential delay equations of the form  $y'(t) = f(t, y(t), y(t - \tau))$ .
  - (b) Calculate the value of the cost function (Equation 4.17) for the solution.
  - (c) Apply the Nelder-Mead Simplex Method<sup>21</sup> on the parameters and repeat from step (a) until convergence is reached.

The determination of the parameters includes a loop over several sets of initial conditions, since the minimum found by the Nelder-Mead method is not necessarily a global minimum. From 10 different initial values, we select the solution with the lowest value of the cost function.

### 4.A.1 Phase average

The phase average  $\tilde{\theta}(t)$  is calculated from the time signal  $\theta(t)$  by rescaling each period, defined from positive zero-crossing to the next positive zero-crossing, to the dominant period, and subsequent averaging of the phases, finally the phase average is rescaled to the mean peak value. Thus

1. Determine  $t_i$ , the  $i$ -th zero-crossing (where  $\theta(t = t_i) = 0$ ).
2. Define the  $i$ -th phase,  $\theta_i(t)$  from  $\theta(t)$  between  $t_{i-1} < t < t_i$ .

3. Define the stretched phase  $\theta_i^*(t') = \theta_i \left( \frac{t-t_{i-1}}{\mathcal{T}_i} \right)$  with  $\mathcal{T}_i = t_i - t_{i-1}$ .
4. Calculate the phase average  $\tilde{\theta}^*(t') = \frac{1}{N} \sum_{i=1}^N \theta_i^*(t')$  and the mean amplitude  $\overline{\theta^*} = \frac{1}{N} \sum_{i=1}^N \max \theta_i^*$ .
5. Rescale the phase average  $\tilde{\theta}(t) = \tilde{\theta}^*(t/\mathcal{T}) \frac{\overline{\theta^*}}{\max \tilde{\theta}^*}$ .

#### 4.A.2 Cost function

The cost function that is minimized in the Nelder-Mead method is defined as

$$f(\theta, \tilde{\theta}) = m_1 m_2 m_3 \frac{\int_0^{\mathcal{T}_{\tilde{\theta}}} (\tilde{\theta} - \theta)^2 dt}{\int_0^{\mathcal{T}_{\tilde{\theta}}} \tilde{\theta}^2 dt}, \quad (4.17)$$

which is the normalized root-mean-square distance between the phase-averaged  $\tilde{\theta}$  and the calculated  $\theta$ , multiplied by additional multipliers,  $m_1$ ,  $m_2$  and  $m_3$  in order to improve the convergence rate of the algorithm, i.e.

- if the oscillation period  $\mathcal{T}_{\theta}$  is different from intended period:  $\mathcal{T}_{\tilde{\theta}}$ .  $m_1 = 1 + 10 \left( \max \left( \frac{\mathcal{T}_{\theta}}{\mathcal{T}_{\tilde{\theta}}}, \frac{\mathcal{T}_{\tilde{\theta}}}{\mathcal{T}_{\theta}} \right) - 1 \right)$
- if any of  $r, \mu, k, \delta - 1$  or  $\delta - \delta_n(\alpha)$  is negative:  $m_2 = \prod_{q \in \{r, k, \mu, \delta, \delta - \delta_n(\alpha)\}} 1 - 100 \min(0, q)$
- if  $\alpha > 1$ :  $m_3 = 1 + 100(\max(\alpha, 1) - 1)$ .

#### 4.A.3 Error estimation

In order to quantify the error in our fitting procedure, we use a bootstrapping of resampling residuals. If we denote the original phase-averaged signal by  $\theta_i$  and the fit by  $\theta_i^*$ , then the residual is defined as  $\varepsilon_i = \theta_i - \theta_i^*$ . Now, the fitting procedure is repeatedly executed on  $\hat{\theta}_i = \theta_i^* + \varepsilon_j$ . The error in  $r, \mu, k$  and  $\tau$  is obtained as the standard deviation of the resulting sets of parameter values. The error in  $\alpha$  and  $\delta$  is then straightforwardly obtained.

## 4.B Derivation of the maximum jet angle

In this appendix, we derive the maximum jet angle for an oscillating jet in a confined cavity. When the jet is in an extreme right position, figure 4.15 is a schematic representation of the



two recirculation zones: a recirculation zone with diameter  $W/2$  in the upper right and a second adjacent recirculation zone of diameter  $W$  lower in the cavity.

The maximum jet angle is indicated with  $\alpha$ , and can be calculated from  $(x_1, y_1)$ , which is the tangent point of both circles, i.e.

$$\tan \alpha = \frac{|x_1|}{|y_1|} \quad (4.18)$$

Based on similar triangles (identified by the angle  $\gamma$ ), it is found that

$$\sin \gamma = \frac{x_1}{W/2} = \frac{W/4}{3W/4} \rightarrow x_1 = \frac{W}{6}. \quad (4.19)$$

Now, the circle in the upper left has center  $(\frac{1}{4}, -\frac{1}{4})$  and radius  $W/4$ , hence

$$\left(x - \frac{W}{4}\right)^2 + \left(y + \frac{W}{4}\right)^2 = \left(\frac{W}{4}\right)^2 \quad (4.20)$$

As  $(x_1, y_1)$  resides on this circle, and  $x_1$  is known, we find

$$y_1 = -\frac{W}{4} \pm \frac{W}{6}\sqrt{2}, \quad (4.21)$$

and thus

$$\tan \alpha = \frac{\frac{1}{6}}{\frac{1}{4} + \frac{1}{6}\sqrt{2}} = \frac{1}{\frac{3}{2} + \sqrt{2}}, \quad (4.22)$$

which has been used in the paper.

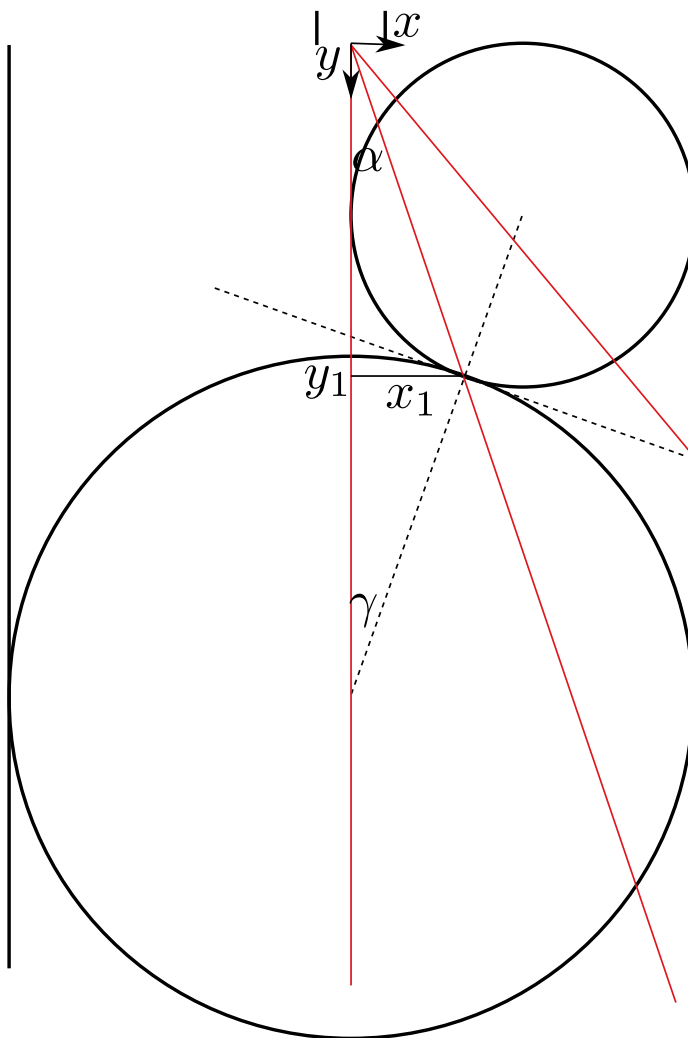


**Figure 4.15** Schematic representation of two recirculation zones of diameter  $W$  and  $W/2$ . The origin is located at the nozzle exit, and the maximum jet angle,  $\alpha$  is observed as the angle between the vertical and the line connecting the nozzle exit with the tangent point of the two circles.



# 5. Electromagnetic control of an oscillating turbulent jet in a confined cavity<sup>§</sup>

Control of self-sustained jet oscillations in confined cavities is of importance for many industrial applications. It has been shown that the mechanism underlying these oscillations consists of three stages: (i) growth of the oscillation, (ii) amplitude limitation and (iii) delayed destruction of the recirculation zone bounding the jet. It has also been shown that oscillations may be enhanced or suppressed by applying (e.g. electromagnetic) body forces.

In the current paper we study the influence of electromagnetic forces oriented aligned with or opposite to the direction of the jet on the oscillation mechanism. The influence of the forcing is found to depend on the Stuart number  $N$  in relation to a critical Stuart number  $N_{crit}$ . We demonstrate that for  $|N| < N_{crit}$ , the oscillation mechanism is essentially unaltered, with moderate modifications in the jet oscillation amplitude and frequency compared to  $N = 0$ . For  $N > N_{crit}$ , electromagnetic forcing leads to total suppression of the self-sustained oscillations. For  $N < N_{crit}$ , electromagnetic forces dominate over inertia and lead to strongly enhanced oscillations, which for  $N \ll -N_{crit}$  become irregular.

As was earlier demonstrated for  $N = 0$ , the present paper shows that for  $-6N_{crit} < N < N_{crit}$  the oscillatory behaviour, i.e. frequencies, oscillation amplitudes and wave shapes, can be described quantitatively with a zero-dimensional model of the delay differential equation (DDE) type, with model constants that can be *a priori* determined from the Reynolds and Stuart number and geometric ratios.

---

<sup>§</sup>Submitted as: Righolt, B. W., Kenjereš, S., Kalter, R., Tummers, M. J., and Kleijn, C. R., Electromagnetic control of an oscillating turbulent jet in a confined cavity.

## 5.1 Introduction

In continuous steel casting, in which liquid steel from a tundish is injected into a thin mould through an injection tube with tailored nozzle configuration,<sup>1,5</sup> an even distribution of heat is important in order to achieve uniform solidification and high quality steel.<sup>27,41</sup> Flow turbulence and large scale self-sustained flow oscillations<sup>12,13</sup> may have a large detrimental impact on the temperature distribution and steel quality.<sup>11</sup> Both can be well controlled by means of an electromagnetic brake (EMBr).<sup>6,7,14</sup>

Electromagnetic forcing of conductive fluids is achieved by the simultaneous application of (induced or externally supplied) electric currents and external magnetic fields. This forcing can enhance or suppress self-sustained jet oscillations,<sup>13</sup> enhance wall-heat transfer by increased turbulent mixing,<sup>15,16</sup> control flows near boundaries,<sup>3,29</sup> in order to reduce drag,<sup>26,30,31</sup> or to control the boundary layer thickness,<sup>8,21</sup> which influences flow separation.<sup>4,37</sup>

Although in many industrial applications complicated nozzle configurations with multiple injected jets are commonly used,<sup>1,5</sup> most of the relevant mechanisms determining flow stability are also present, and can be studied more generically, in a single jet configuration.<sup>13,33</sup> A single jet injected into a thin confined cavity exhibits self-sustained oscillations above a critical Reynolds number, depending on the width to nozzle diameter ratio.<sup>28</sup> These oscillations are found in a large range of jet Reynolds numbers, i.e.  $100 < Re < 170,000$ .<sup>2,13,19,23,24,34</sup> For given jet Reynolds number, increasing the cavity width leads to a decreasing oscillation frequency,<sup>20</sup> until the oscillation vanishes.<sup>22</sup>

In this paper we study the influence of electromagnetic body forces on single jet oscillations in a confined cavity. We impose the Lorentz force as a body force to enhance and suppress these oscillations. The objective of this paper is to (i) study the fundamental flow regimes introduced by imposing an EMBr on a single jet oscillation, (ii) investigate the similarities between the self-sustained jet oscillation mechanism with and without application of an EMBr, (iii) demonstrate that flow oscillations in thin cavities in the presence of EMBr forcing can be described by a zero-dimensional model of the Delay Differential Equation (DDE) type.

The paper is outlined as follows. The electromagnetically controlled jet configuration, a description of the electromagnetic forcing and the numerical methods used to simulate these are given in section 5.2, the physical mechanisms underneath the self-sustained oscillation in the presence of an EMBr are discussed in section 5.3. Section 5.4 describes a zero-dimensional model for electromagnetically controlled single jet oscillations in a confined cavity, and section 5.5 discusses the details of the model parameters and demonstrates the applicability of the model.

## 5.2 Problem definition and methods

### 5.2.1 Description of the set-up

Figure 5.1 depicts the configuration of a thin liquid filled cavity that we study in this paper. The cavity has dimensions  $H \times W \times T = 0.7 \times 0.3 \times 0.035 \text{ m}^3$  and was previously studied experimentally using planar particle imaging velocimetry (PIV)<sup>13</sup>, as well as numerically for varying width  $W$  using Large Eddy Simulations (LES). In<sup>28</sup> we also proposed a zero-dimensional model that predicts the amplitude and frequency of self-sustained jet oscillations in thin liquid filled cavities as a function of the jet Reynolds number and geometric ratios. A square nozzle of size  $d = 0.01 \text{ m}$  is submerged to a depth  $d_n = 0.1 \text{ m}$  underneath the free liquid surface and injects the fluid with a velocity  $v_{in}$  into the cavity. The electrically conducting fluid in the domain has density  $\rho = 1.1 \times 10^3 \text{ kgm}^{-3}$ , viscosity  $\nu = 1.27 \times 10^{-6} \text{ m}^2\text{s}^{-1}$  and conductivity  $\sigma = 7.1 \text{ Sm}^{-1}$ . These properties correspond to the working fluid used in the experiments of the previous studies.<sup>13</sup>

In the present work, we apply electromagnetic forcing as a body force for the control of the jet motion. We follow the design by Kalter et al.<sup>13</sup> and place two electrodes on opposite sides of the cavity, at a distance  $L$  below the nozzle exit with a potential difference  $\Delta\phi = \phi_1 - \phi_2$ . These electrodes are centered in the  $z$ -direction and have an area of  $A = 0.03 \times 0.03 \text{ m}^2$ . A direct current  $I$  flows either from left to right ( $I > 0$ ) or from right to left ( $I < 0$ ) between both electrodes. Furthermore, we place three magnets in the top of the domain, just underneath the nozzle exit against the outside of the back wall. The magnets are aligned with their centers at  $y = -0.15 \text{ m}$  and  $z = -0.045 \text{ m}$  and separated by a distance  $D = 0.08 \text{ m}$ . The poles of the magnets are facing in alternating direction. The directions of the resulting Lorentz forces are also depicted in Figure 5.1 and can be flipped by changing the direction of the electrical current. Later we will show that this leads to an enhancement or suppression of the oscillations.

In Figure 5.1(left) we indicate the jet angle  $\theta$ , which is defined from a least squares fit of a line through the points  $(x_i, y_i)$  defined by  $x_i = \max_x(|v(y_i)|)$  and  $(-d_n - S) < y_i < (-d_n)$ , where we choose  $S = W$ . Furthermore, the two monitoring points,  $p_1$  and  $p_2$  are defined on opposite sides of the jet.<sup>28</sup>

### 5.2.2 Dimensionless numbers

In this work we define the Reynolds number,  $Re$ , the Stuart number,  $N$ , and the Strouhal number,  $St$ , as

$$Re = \frac{v_{in}d}{\nu}, \quad N = \frac{B_{ref}dI}{\rho A v_{in}^2}, \quad St = \frac{fW}{v_{in}}, \quad (5.1)$$

here,  $B_{ref}$  is a reference magnetic field strength, that we will define later.  $f$  is the frequency of the long term self-sustained oscillations. Note that  $N$  takes the sign of  $I$ , thus  $N > 0$  for

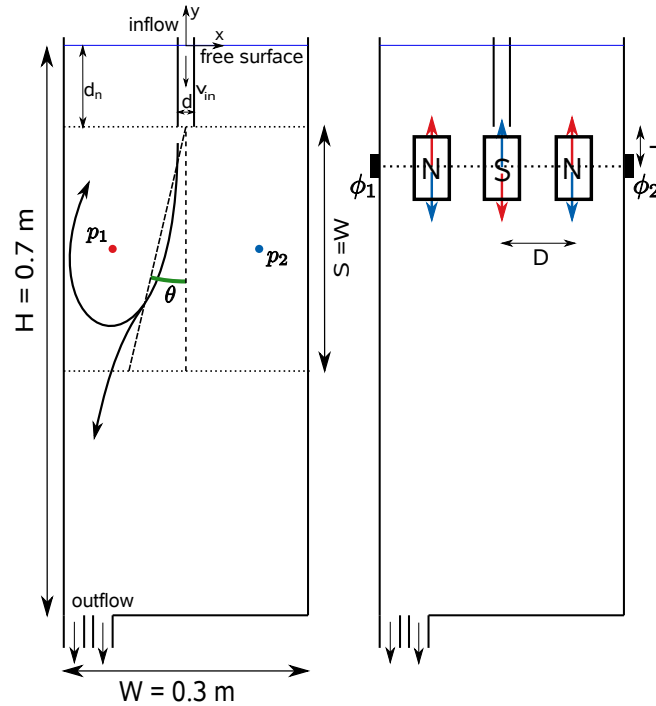


**Figure 5.1** The  $z = 0$ -plane of the configuration of a single jet in a confined geometry with electromagnetic forcing. The cavity dimension is  $H \times W \times T = 0.7 \times 0.3 \times 0.035 \text{ m}^3$  and a vertically oriented square nozzle with inner diameter  $d = 0.01 \text{ m}$  is submerged by  $d_n = 0.1 \text{ m}$  below the free liquid surface. (left) The definition of the jet angle  $\theta$ , defined in between  $y = -d_n$  and  $y = -d_n - S$  and the monitoring positions  $p_1$  and  $p_2$ , located at  $(\pm 0.092 \text{ m}, 0.4 \text{ m}, 0 \text{ m})$ , are indicated. (right) The locations of the magnets are indicated by rectangles with their respective orientation indicated with either  $N$  or  $S$ . Electrodes on both sides, indicated with  $\phi_1$  and  $\phi_2$ , generate a current through the system. The Lorentz forces are indicated by the red arrows for  $I < 0$  and by the blue arrows for  $I > 0$ .

$I > 0$  (which is the oscillation suppressing configuration) and  $N < 0$  for  $I < 0$  (which is the oscillation enhancing configuration).

### 5.2.3 Magnetic field calculation

The imposed magnetic field was modelled based on the  $z$ -component of the magnetic field as measured by Kalter et al.<sup>13</sup>. We fit an analytical expression for the magnetic field of block magnets<sup>36</sup> to the reported  $z$ -component of the magnetic field, as indicated in Figure 5.2(bottom). Figure 5.2(top) shows the computationally imposed magnetic field in the  $z = 0$ -plane, indicating its three-dimensional character. The reference magnetic field is defined as

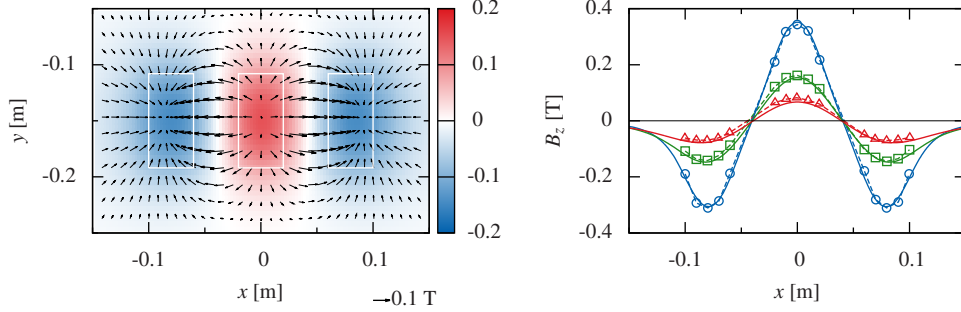


**Figure 5.2** (top) Contours of the  $z$ -component of the imposed magnetic field and arrows of  $x$  and  $y$  components of the magnetic field in the  $z = 0$ -plane, white rectangles indicate the positions of the three magnets. (bottom) The  $z$ -component of the magnetic field for the numerical simulations (solid line) and experiments<sup>13</sup> (symbols) at  $y = -0.15$  m for three  $z$ -positions in the cavity: close to the back wall ( $z/T = -1/2$ , blue, circles), in the center of the domain ( $z/T = 0$ , green, squares) and close to the front wall ( $z/T = 1/2$ , red, triangles).

the magnetic field strength in this plane in the center of the central magnet, thus  $B_{ref} = 0.15$  T. The magnitude of the  $x$  and  $y$  components of the magnetic field in the  $z = 0$ -plane is of the same order of magnitude as the  $z$  component of the magnetic field. The imposed electric current leads to an electric potential as shown in Figure 5.3(top) and Lorentz forces as shown in Figure 5.3(bottom) for  $I > 0$ . For  $I < 0$ , the electrical potential and consequently the Lorentz force are reversed.

## 5.2.4 Flow simulations

The LES filtered, single phase, incompressible Navier-Stokes equations are solved in this study:

$$\begin{aligned} \frac{\partial v_i}{\partial t} + v_j \frac{\partial v_i}{\partial x_j} \\ = -\frac{1}{\rho} \frac{\partial p}{\partial x_i} + \frac{\partial}{\partial x_j} \left[ (\nu + \nu_{SGS}) \left( \frac{\partial v_i}{\partial x_j} + \frac{\partial v_j}{\partial x_i} \right) \right] + f_i. \end{aligned} \quad (5.2)$$

Here  $v_i$  is the velocity,  $\rho$  the material density,  $\nu$  the laminar viscosity,  $\nu_{SGS}$  the sub-grid-scale viscosity from the LES model,  $p$  the pressure and  $f_i$  the Lorentz force. The Lorentz force is calculated from the current  $j_i$  and magnetic field  $b_i$  as<sup>17</sup>

$$f_i = \epsilon_{ijk} j_j b_k \quad \text{with } j_i = \frac{\sigma}{\rho} \left( -\frac{\partial \phi}{\partial x_i} + \epsilon_{ijk} u_j b_k \right), \quad (5.3)$$



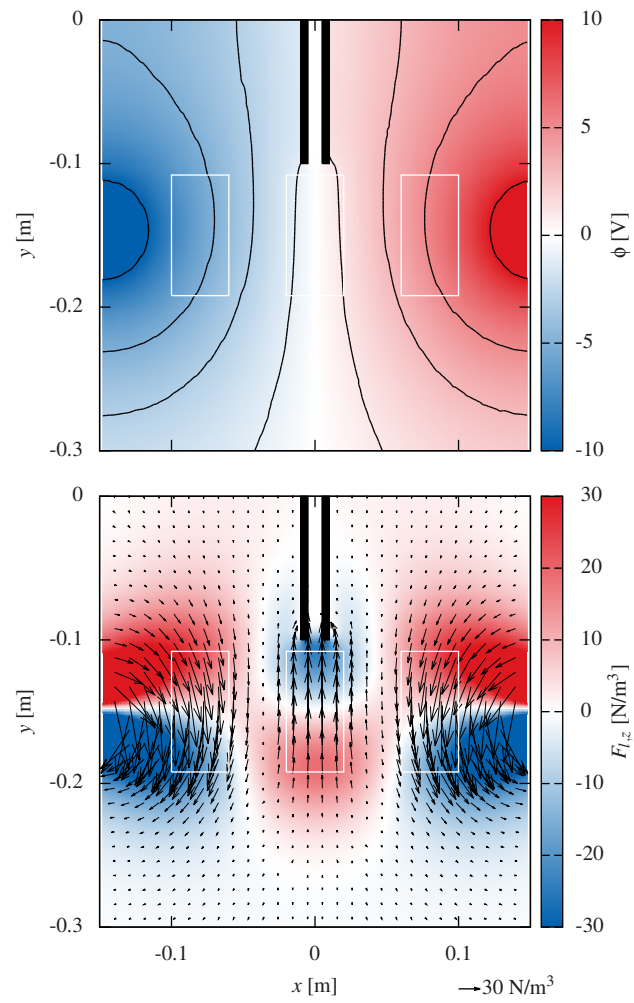


**Figure 5.3** (top) Contours of the electric potential, when a current  $I = 4$  A is directed from left to right. (bottom) Contours of the  $z$ -component of the corresponding Lorentz force and vectors of the  $x$  and  $y$  components in the  $z = 0$ -plane. The position of the magnets is indicated by white rectangles, and the position of the nozzle with black rectangles.

where  $\sigma$  is the electrical conductivity of the fluid and  $\phi$  is the electric potential, which is obtained from solving the Poisson equation

$$\frac{\partial^2 \phi}{\partial x_i^2} = \frac{\partial}{\partial x_i} (\epsilon_{ijk} u_j b_k), \quad (5.4)$$

We use the open source code OpenFOAM 2.1<sup>38</sup> based on the finite volume method to solve the discretized equations using the PISO scheme.<sup>9</sup> As a sub-grid-scale LES model we use the dynamic Smagorinsky model, which is effective in modelling the subgrid scales in these one-way coupled MHD flows.<sup>18</sup> The discretization of the equations and the wall treatment are in line with our previous publication.<sup>28</sup>

### 5.2.5 Validation

The numerical model is validated against experiments<sup>13</sup> for a jet of  $Re = 4,700$  and electromagnetic forcing with  $N = 0.017$  ( $I = 4$  A) in the oscillation suppressing configuration. Figures 5.4 and 5.5 show computed time averaged velocities compared to experimental data. The comparisons show a good agreement in the mean velocity between the numerical and experimental results. It is noted that the simulated and measured flow field are not fully symmetric due to the asymmetry in the outflow in the bottom of the domain (see Figure 5.1). The numerical simulations also show a good agreement in the oscillation frequency for various  $N$ , as we show in Figure 5.9, which also shows the  $N - St$  relation obtained from the experiments.

## 5.3 Influence of electromagnetic forcing on self-sustained oscillations

This section described the influence of the electromagnetic force on the mean velocity, oscillation frequency, the pressure difference across the jet, the amplitude of the jet angle oscillation, and the flow regimes.

### 5.3.1 Mean velocity

For  $Re = 4,700$ , we performed numerical simulations for various  $-0.075 < N < 0.015$ . Figure 5.6 shows the corresponding mean velocity vector fields, which demonstrates that the velocity field is strongly dependent on  $N$ , with the jet and recirculation zone strength increasing for negative  $N$  and decreasing for positive  $N$ .

The scaling of the jet velocity with  $N$  can be determined from a vertical momentum balance when considering a control volume of width  $\Delta X$  centered around the magnet below the jet

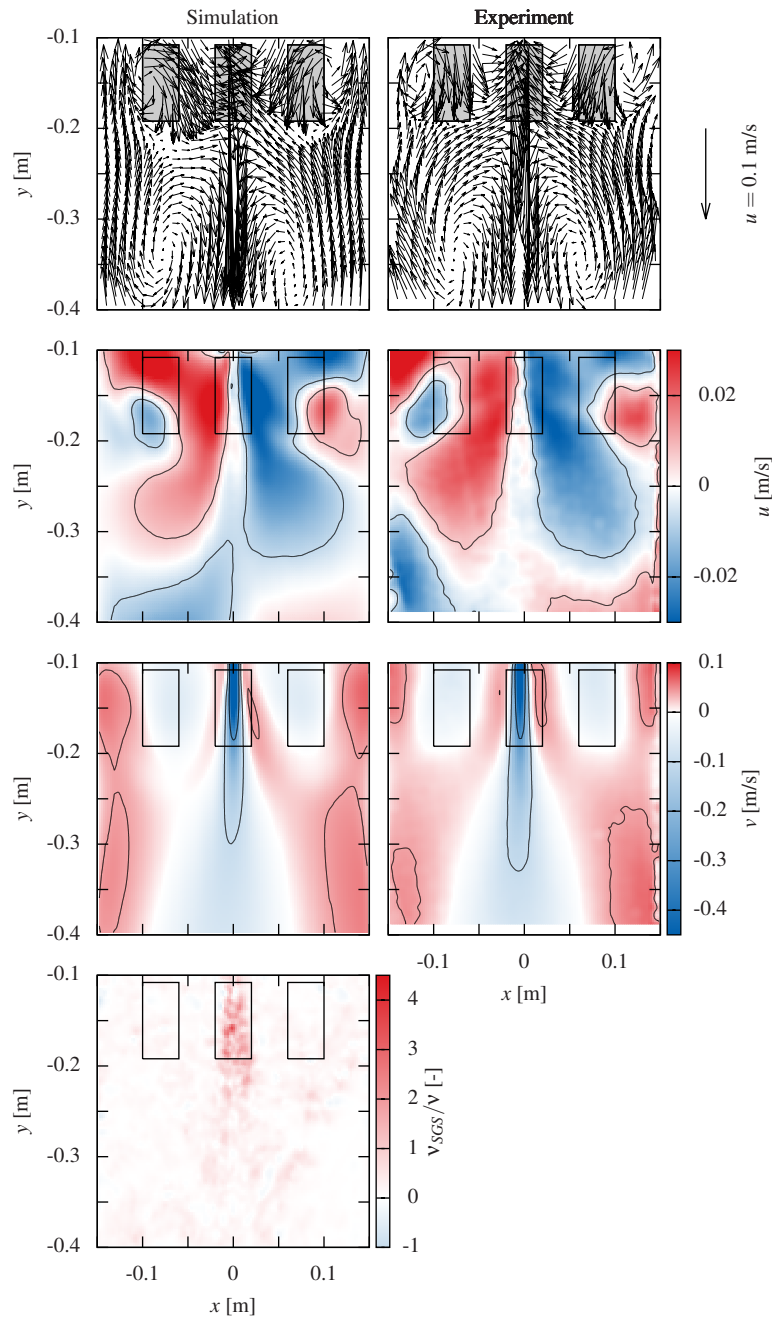


**Figure 5.4** For  $Re = 4,700$  and  $N = 0.017$  in the  $z = 0$ -plane, simulation (left) and experiment (right), from top to bottom: Vector fields of the mean velocity, contours of the horizontal mean velocity, contours of the vertical mean velocity and contours of the scaled instantaneous sub-grid-scale viscosity  $\nu_{SGS}/\nu$ . The black rectangles indicate the position of the magnets.

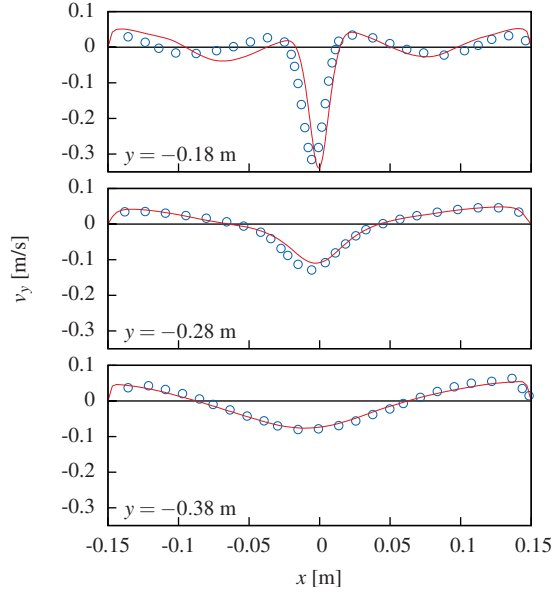


**Figure 5.5** The time averaged vertical velocity component for  $y = -0.18$  m,  $y = -0.28$  m and  $y = -0.38$  m, for  $Re = 4,700$  in the oscillation suppressing ( $N = 0.017$ ) configuration for both the numerical simulation (red solid line) and the experiment<sup>13</sup> (symbols).

exit. This control volume is schematically depicted in Figure 5.7. The average strength of the vertical component of the Lorentz force in this control volume is denoted by  $F_L$ . The vertical momentum balance then leads to

$$-\rho d^2 v_{in}^2 + \rho \Delta X T v_{jet}^2 + F_L = 0. \quad (5.5)$$

The strength of the Lorentz force scales linearly with the current density ( $I/\text{area}$ ) and the magnetic field strength, hence we know that

$$F_L \propto \frac{I B_{ref}}{\text{area}}. \quad (5.6)$$

By rearranging Equation 5.5, using the definition of  $N$  (Equation 5.1) and the above scaling of  $F_L$ , we obtain

$$\frac{v_{jet}^2}{v_{in}^2} \propto \frac{d^2}{T \Delta X} (1 - cN), \quad (5.7)$$

where  $c$  is a positive constant which is solely dependent on geometrical properties of the present configuration. We can now conclude that the square of the velocity in the jet is linearly dependent on  $N$ , increasing for  $N < 0$  and decreasing for  $N > 0$ . This is confirmed by our numerical simulations, as shown in Figure 5.8.

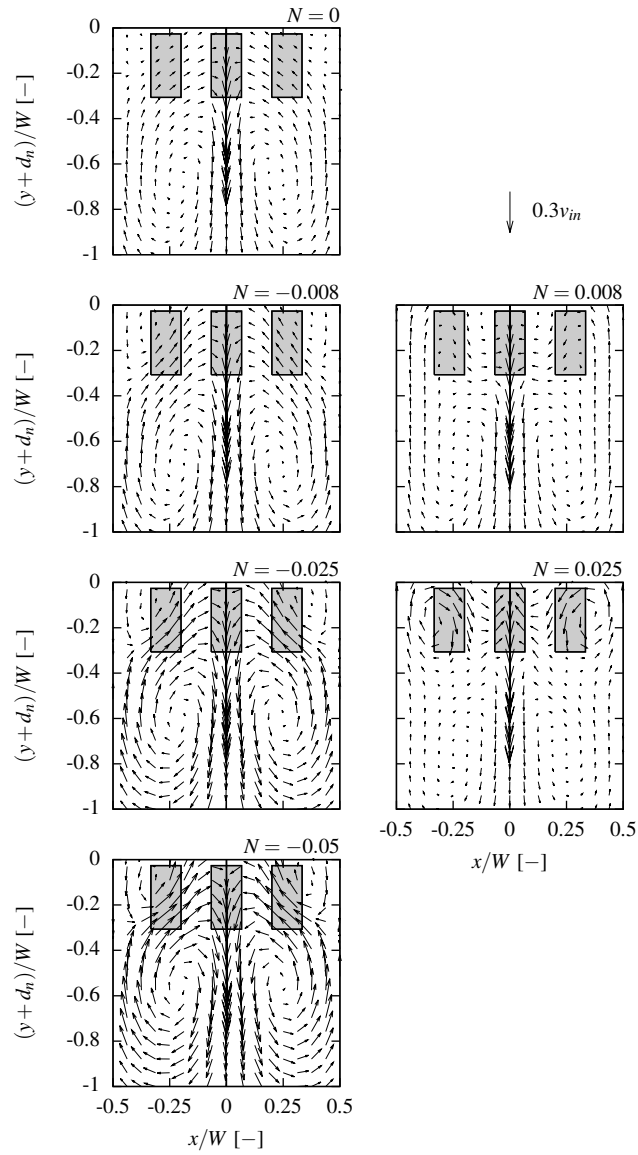


**Figure 5.6** Vector field of the mean velocity for  $Re = 4,700$  and Stuart numbers in the range  $-0.05 \leq N \leq 0.025$ . The positions of the magnets are indicated by gray rectangles.

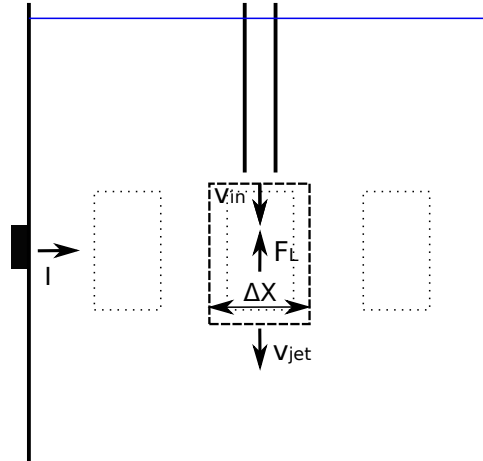


**Figure 5.7** The Lorentz force  $F_L$  is active in a control volume of width  $\Delta X$ , thickness  $T$  and certain height. The control volume is used for deriving the scaling relation of  $v_{jet}/v_{in}$  as a function of  $N$ .

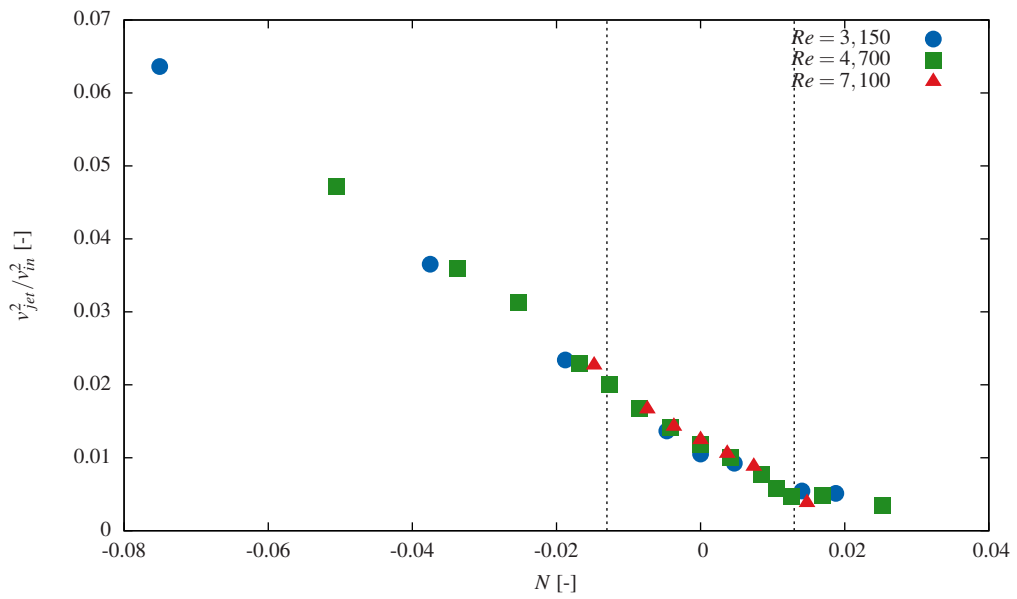


**Figure 5.8** The square of the mean jet velocity (calculated through an area of size  $D \times T$  located at  $y = -0.19$  m), normalized by the inlet velocity  $v_{in}$  as a function of  $N$ . The vertical dashed lines indicate  $N = \pm N_{crit}$ .

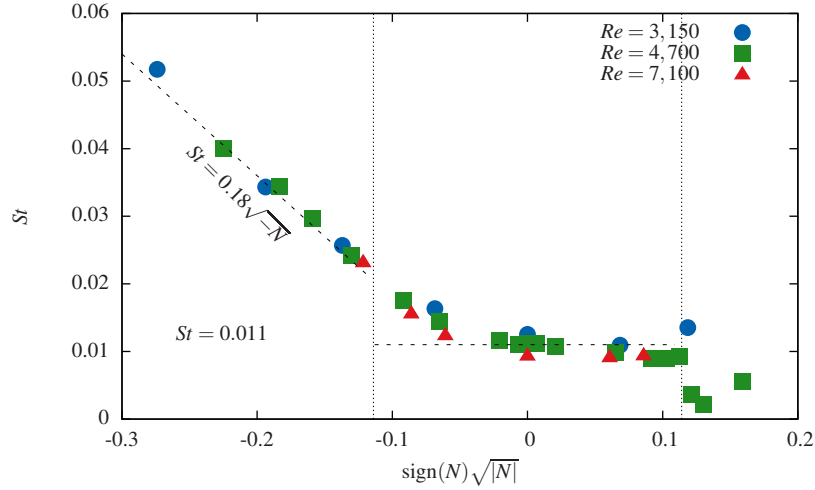


**Figure 5.9**  $St$  as a function of  $N$  for the oscillation suppressing ( $N > 0$ ) and enhancing ( $N < 0$ ) configuration for  $Re = 3,150$  (blue circles),  $Re = 4,700$  (green squares) and  $Re = 7,100$  (red triangles). The dashed lines indicate the lines  $St = 0.011$  and  $St = 0.18\sqrt{-N}$  and the vertical lines indicate  $N = \pm N_{crit}$ .

### 5.3.2 Oscillation frequency

Without electromagnetic forcing ( $N = 0$ ), it is shown in<sup>13,28</sup> that the jet oscillates with a constant Strouhal number  $St = 0.011$ , and thus that  $f \sim v_{in} \sim v_{jet}$  for fixed  $W$ .

For  $N > 0$ , the Lorentz force in the jet opposes the inflowing jet, leading to a lower jet velocity. For small, but positive  $N$ , the electromagnetic braking is weak, and we confirm that remains  $St = 0.011$ , as shown in Figure 5.9. The oscillation frequency does not change until  $N > N_{crit}$ , when the electromagnetic force becomes dominant over the inertial force and the oscillations are completely suppressed.

For  $N < 0$ , the Lorentz force is directed in the same direction as the inflowing jet, leading to increased  $v_{jet}$  at fixed  $v_{in}$ . From Equation 5.7 and  $f \sim v_{jet}$  it may be expected that for large negative  $N$ ,  $St \propto \sqrt{-N}$ . This is indeed observed in the present numerical simulations (see Figure 5.9) irrespective of  $Re$  in the range  $3,150 \leq Re \leq 7,100$ , showing good agreement with the experimentally observed proportionality of  $St$  with  $\sqrt{-N}$ .\*

\*Please note that in Kalter et al., the definition of the Stuart number and the calculation, are incorrect by a constant factor 3.15. Here, we use the correct values.

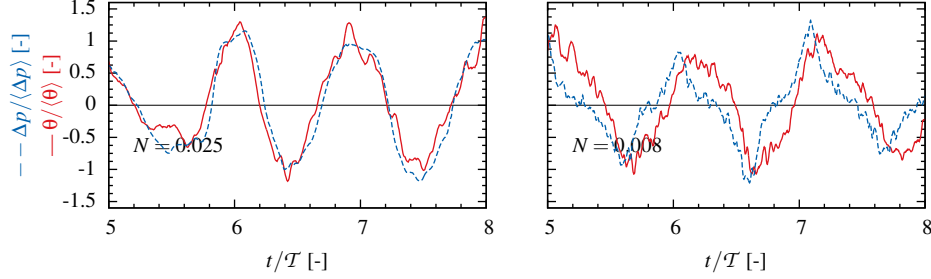


**Figure 5.10** The pressure difference  $\Delta p$  normalized by  $\langle \Delta p \rangle$  and the jet angle  $\theta$  normalized with  $\langle \theta \rangle$ , as a function of the time normalized with the period  $\mathcal{T}$  for  $N = -0.025$  (top,  $\mathcal{T} = 17$  s,  $\langle \Delta p \rangle = 33$  Pa,  $\langle \theta \rangle = 26^\circ$ ) and  $N = 0.008$  (bottom,  $\mathcal{T} = 52$  s,  $\langle \Delta p \rangle = 10$  Pa,  $\langle \theta \rangle = 30^\circ$ ) and  $Re = 4,700$ .

### 5.3.3 Pressure oscillations

We define the pressure difference across the jet as  $\Delta p = p_2 - p_1$  (see Figure 5.1). In our earlier paper<sup>28</sup> we have shown that the proportionality of  $\Delta p$  and  $\theta$  is a key property of the self-sustained jet oscillation.<sup>28</sup> We confirm with Figure 5.10 that this proportionality remains present for  $N \neq 0$ . The pressure difference between the center and the edge of a recirculation zone is proportional to the square of the tangential velocity near its edge.<sup>12</sup> As the square of the jet velocity is linearly dependent on  $N$  (see Equation 5.7) we also expect the amplitude of the pressure oscillation,  $\langle \Delta p \rangle$ , to be linearly dependent on  $N$ . This is confirmed by our numerical simulations, as shown Figure 5.11. This observation is independent of  $Re$ .

### 5.3.4 Jet angle amplitude

The amplitude of the jet angle oscillation,  $\langle \theta \rangle$ , is also dependent on  $N$ , as we show in Figure 5.12. For  $N = 0$ ,  $\langle \theta \rangle$  is the largest ( $\langle \theta \rangle = 18^\circ$ ), and can be obtained from geometrical considerations.<sup>28</sup>

In the oscillation suppressing configuration ( $N > 0$ ), the oscillations vanish for  $N > N_{crit}$ , whereas in the oscillation enhancing configuration ( $N < 0$ ),  $\langle \theta \rangle$  reaches a constant value, i.e.,  $\langle \theta \rangle = 12.5^\circ$  for  $N < -N_{crit}$ . For  $|N| < N_{crit}$ ,  $\langle \theta \rangle$  roughly diminishes quadratically with  $N$ , i.e.:

$$\langle \theta \rangle = \theta_{max} - \beta \left( \frac{N}{N_{crit}} \right)^2, \quad (5.8)$$

with  $\theta_{max} = 18^\circ$  and  $\beta = 5.5^\circ$ . We determined  $N_{crit} = 0.013$ . Both functions for  $\langle \theta \rangle$  are indicated in Figure 5.12.

The physical reasoning behind this behavior of  $\langle \theta \rangle$  becomes apparent from Figure 5.6. In the oscillation suppressing configuration ( $N > 0$ ), the flow is pushed downward by the magnets in the corners. This prevents the growth of the recirculation zones and hence limits



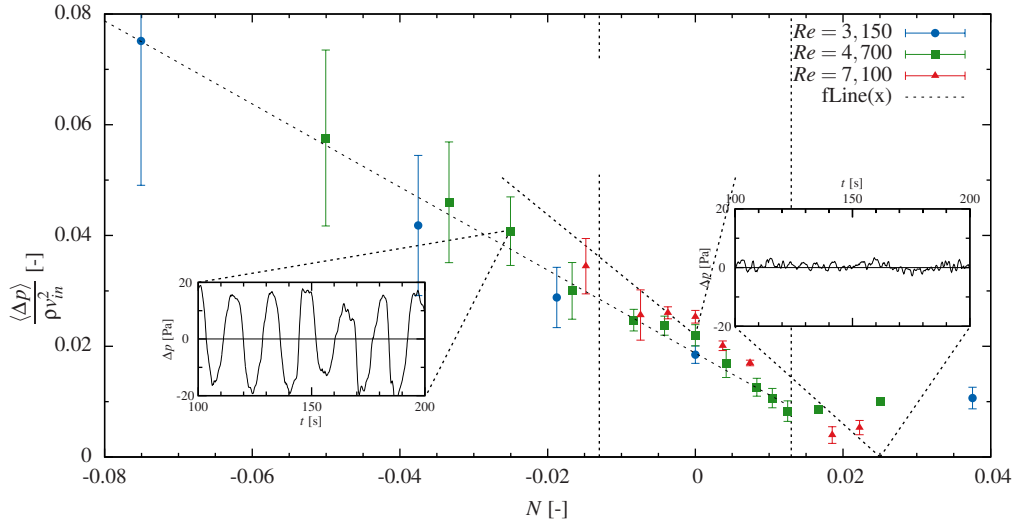


**Figure 5.11** The amplitude  $\langle \Delta p \rangle$  of the pressure oscillations, normalized by the energy  $\rho v_{in}^2$  as a function of  $N$  for  $Re = 3,150$  (blue circles),  $Re = 4,700$  (green squares) and  $Re = 7,100$  (red triangles). The insets show the instantaneous  $\Delta p$  for  $N = -0.025$ ,  $N = 0$  and  $N = 0.025$ . The vertical dashed lines indicate  $\pm N_{crit}$ . The error bars indicate the standard deviation of the calculated  $\langle \Delta p \rangle$ .

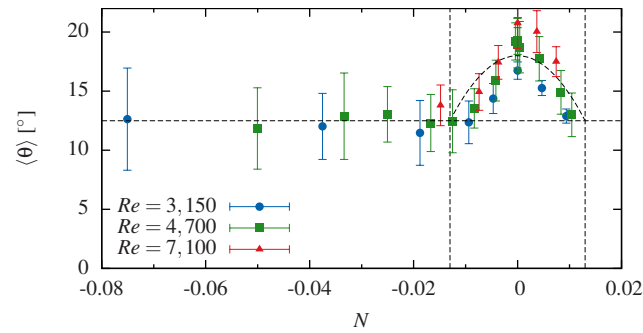


**Figure 5.12** The amplitude  $\langle \theta \rangle$  of the jet angle oscillation as a function of  $N$ , with  $\langle \theta \rangle = \theta_{max} - \beta(N/N_{crit})^2$  with  $\theta_{max} = 18^\circ$  and  $\beta = 5.5^\circ$ , for  $|N| < N_{crit} = 0.013$ .  $\langle \theta \rangle = 12.5^\circ$  for  $N < -N_{crit}$ , and  $\langle \theta \rangle = 0$  for  $N > N_{crit}$ .

$\langle \theta \rangle$ . Conversely, in the oscillation enhancing configuration ( $N < 0$ ), the recirculation zone gets elongated (see Figure 5.6 for  $N = -0.008$ ), which also leads to a reduced jet angle. Increasing the current further ( $N < -N_{crit}$ ), leads to the flow mainly being driven by the electromagnetic forcing, a approximately constant flow profile and hence constant  $\langle \theta \rangle$ .

### 5.3.5 Flow regimes

We can now conclude that for varying  $N$ , three regimes can be distinguished, independent of  $Re$  and separated by  $N_{crit} = 0.013$ :

- For  $N > N_{crit}$ , oscillations are suppressed.
- For  $-N_{crit} < N < N_{crit}$ , self-sustained oscillations by the jet are dominant.  $St$  remains constant and has the same value as for  $N = 0$ . However, the jet amplitude decreases quadratically with  $|N|$ .
- For  $N < -N_{crit}$ , the Lorentz forces are dominant and control the oscillations in the domain.

## 5.4 Zero-dimensional model of the jet oscillation

In this section, we describe a zero-dimensional DDE-type model, which quantitatively describes single jet oscillations, then we show how it can be applied to electromagnetically forced single jet oscillations. Such a quantitative description can be used to predict the frequency and waveform of jet oscillations, and is an alternative for experiments of full three-dimensional numerical simulations.

### 5.4.1 Unforced flow ( $N = 0$ )

As we have shown earlier, the self-sustained oscillation of the jet, in the absence of electromagnetic forcing, can be explained from the transient behaviour of  $\Delta p$  and  $\theta$ .<sup>28</sup> When the jet is slightly oriented to one side (say, the right,  $\theta < 0$ ), the recirculation zone on the right will be stronger, i.e., it has a smaller diameter and higher velocities. This leads to a larger pressure deficit in the recirculation zone, deflecting the jet even further. The jet angle will subsequently reach an extreme, as the jet impinges on the side wall and the recirculation zone can not shrink any further. Subsequently, the fluid escapes the strong recirculation zone on the right and feeds the recirculation zone on the left. The pressure deficit in the recirculation zone on the right diminishes, and the jet angle will deflect to the left.

In<sup>28</sup> we showed, from a horizontal momentum balance, that the growth of the jet angle during the initial stage of the oscillation is proportional to the horizontal pressure difference over the

jet

$$\frac{d\theta}{dt} \propto \Delta p \quad (5.9)$$

Furthermore, we have shown that  $\Delta p \sim \theta$ , and hence

$$\frac{d\theta}{dt} = r\theta, \quad (5.10)$$

where  $r$  is the growth rate of the oscillation.

The maximum jet angle,  $\langle\theta\rangle$ , that can be reached is constrained by the geometry. This acts as a damping term on the oscillation, hence

$$\frac{d\theta}{dt} = (r - \mu\theta^2) \theta, \quad (5.11)$$

where  $\mu$  is the obstruction parameter, related to  $\langle\theta\rangle$ .

In the last stage of the oscillation, the strong recirculation quickly decays in a timescale  $\tau$ , which is of the order of the turnover time of the recirculation zone. This leads to the full model equation<sup>28</sup>

$$\frac{d}{dt}\theta(t) = r\theta(t) - \mu\theta^3(t) - k\theta(t - \tau), \quad (5.12)$$

where  $k$  is the decay rate for the destruction of the strong recirculation zone. Equation 4.10 is a zero-dimensional model, which is of the Delay Differential Equation (DDE) type. Its model constants can be determined *a priori* as a function of inflow parameters and geometry only.<sup>28</sup>

## 5.4.2 Electromagnetically forced flow ( $N \neq 0$ )

Here we argue that the general shape of model equation 5.12 remains valid for  $N \neq 0$ , but with modified model parameters that will now also depend on  $N$ . We will discuss the influence of  $N \neq 0$  on each of the three right-hand terms in Equation 5.12, viz. (i) the growth term, (ii) the damping term, and (iii) the delayed decay term.

(i) Equation 5.9 remains true for  $N \neq 0$  as the imposed Lorentz force in the present configuration is dominantly vertical (see Figure 5.3). Furthermore, from Figure 5.10 we conclude that  $\Delta p$  and  $\theta$  remain proportional. Therefore, Equation 5.10 remains valid as well for  $N \neq 0$ . Thus, the form of the growth term in Equation 5.12 remains unchanged. The constant of proportionality, the growth rate  $r$ , is however influenced by the Lorentz force, as  $\Delta p$  is highly dependent on the electromagnetic forcing. We have shown in Figure 5.11 that  $\langle\Delta p\rangle$  depends linearly on  $N$ . Due to this dependence, we also expect  $r$  to be linearly dependent on  $N$ .

(ii) For each value of  $N$ , we find a specific value for the maximum jet deflection angle  $\langle\theta\rangle$ . For  $N = 0$ , only the geometry obstructs the motion of the jet angle, leading to  $\langle\theta\rangle = 18^\circ$ .<sup>28</sup> In Figure 5.12 above, we have shown that the maximum jet angle depends quadratically on

$N$  for  $|N| < N_{crit}$ . For  $N > N_{crit}$  the oscillations vanish, and thus  $\langle \theta \rangle = 0$ , whereas for  $N < -N_{crit}$ , we have shown that the oscillation is enhanced mainly by the electromagnetic forcing and the maximum jet angle is constant,  $\langle \theta \rangle = 12.5^\circ$ . For each  $N$ , the maximum jet deflection can be accounted for through a damping term of the form of the second right-hand term in Equation 4.10, with the model constant  $\mu$  now being a function of  $N$ .

(iii) Since, for  $|N| < N_{crit}$  the flow is dominated by inertial forces, the description of the oscillation by means of the delayed feedback mechanism<sup>28</sup> still holds, with the model constant being slightly dependent on  $N$ .

For  $N < -N_{crit}$ , the electromagnetic forcing has a larger influence on the delay time. The velocities in the domain quickly increase with decreasing  $N$ , leading to a shorter delay time  $\tau$  and larger influence of the feedback induced destruction of the recirculation zone pressure minimum. We therefore expect both model constants  $k$  and  $\tau$  in the delayed decay term to strongly depend on  $N$  for  $N < -N_{crit}$ .

## 5.5 Determination of the model parameters and its implications

For  $N = 0$ , the self-sustained jet oscillations in a thin, confined cavity can be described by Equation 5.12, which contains four model parameters,  $r$ ,  $\mu$ ,  $k$  and  $\tau$ . These parameters can be determined *a priori* based on  $Re$ ,  $W/d$ ,  $v_{in}$  and  $W$ .<sup>28</sup> In this section we will demonstrate that the electromagnetic forcing can be incorporated with one additional parameter, viz.  $N$ .

### 5.5.1 Non-dimensional model

Model Equation 5.12 can be written in terms of the dimensionless time  $t' = rt$  and jet angle  $\theta' = \sqrt{\mu/r}\theta$ :<sup>28</sup>

$$\frac{d\theta'}{dt'} = \theta' - \theta'^3 - \alpha\theta'(t' - \delta). \quad (5.13)$$

The variables  $\alpha = k/r$  and  $\delta = r\tau$  denote the relative strength of the feedback mechanism compared to the growth rate and the dimensionless delay time respectively. The neutral curve, obtained from a linear stability analysis, is<sup>28,32</sup>

$$\delta_n(\alpha) = \arccos\left(\frac{3\alpha - 2}{\alpha}\right) (\alpha^2 - (3\alpha - 2)^2)^{-\frac{1}{2}}. \quad (5.14)$$

This critical curve separates the stable and oscillatory regimes of the model Equation 5.13. For  $\delta < \delta_n(\alpha)$ , all modes are stable and no oscillations will be present. For  $\delta > \delta_n(\alpha)$ , oscillatory modes will be sinusoidal of shape close to the neutral curve and approach block-waves for  $\delta \geq 10$ .

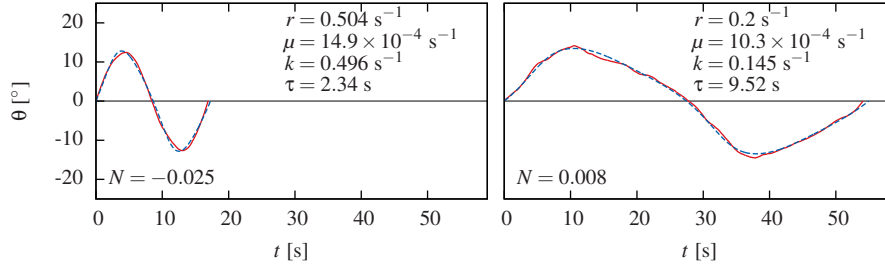


**Figure 5.13** The phase averaged jet angle amplitude (solid red line) in conjunction with the model fit (dashed blue line), for  $Re = 4,700$  and for  $N = -0.025$  (top) and  $N = 0.008$  (bottom).

## 5.5.2 Parameter fitting

From our numerical simulations for varying  $N$ , we calculate  $\theta(t)$  and the phase average jet angle amplitude. From a fitting procedure we determine the best fitting parameter set  $r, \mu, k, \tau$  following the method outlined in.<sup>28</sup>

In Figure 5.13 we show the phase averaged jet angle amplitude together with the solution of the DDE model for the fitted parameter set, for both  $N = -0.025$  and  $N = 0.008$ . This figure shows the good agreement between the zero-dimensional model solution and the actual jet angle profile obtained from the LES simulations.

For  $N > N_{crit}$  no oscillations are present, hence we cannot calculate a phase average, nor determine  $\alpha$  and  $\delta$  from the numerical simulations. However, for  $N < N_{crit} = 0.013$  we determine the parameters  $\alpha$  and  $\delta$  for  $-5N_{crit} \leq N \leq N_{crit}$ ,  $3,150 \leq Re \leq 7,100$  and  $W/d = 30$ .

We show the fitted parameters  $\alpha$  and  $\delta$  for this parameter set and the neutral curve  $\delta_n$  (Equation 5.14) in Figure 5.14. From this stability diagram a clear distinction between the inertial dominated and electromagnetically dominated regimes becomes apparent. For  $|N| < N_{crit}$  the jet oscillation itself is dominant, and we showed in our previous publication<sup>28</sup>, that the parameters describing these oscillation are close to the neutral curve. And indeed, this is observed in Figure 5.14. For  $N < -N_{crit}$ , the parameters cluster together close to  $(\delta, \alpha) = (1, 1)$ . In other words, for  $N < -N_{crit}$  the normalized behavior of the system does not change. Although the parameters  $\alpha$  and  $\delta$  sparsely change over a variation in  $N$ , the underlying variables  $r, \mu, k$  and  $\tau$ , will change significantly as we will later show.

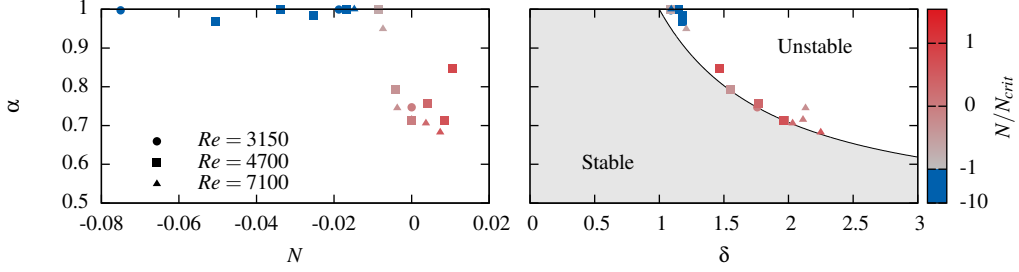


**Figure 5.14** For  $-0.08 \leq N \leq 0.02$  (color of symbols) and  $3, 150 \leq Re \leq 7, 100$  (symbol type) (left)  $\alpha$  as a function of  $N$  and (right) the neutral curve (Equation 5.14, solid line), with the shaded and non-shaded area denoting the regions of stable and oscillatory modes, respectively. The parameter values  $(\delta, \alpha)$  are indicated in the diagram, where the colors indicate  $|N| < N_{crit}$  (grey-red) and  $N < -N_{crit}$  (blue) as well.

### 5.5.3 Parameter estimation

Without forcing the model parameters  $r$  and  $\tau$  were found to be given by<sup>28</sup>

$$r = \kappa_1 \frac{v_{in}}{W} Re^{-\frac{1}{4}} \left( \frac{W}{d} \right)^{-\frac{1}{2}}, \quad \tau = \kappa_2 \frac{W}{v_{in}} Re^{\frac{5}{9}}, \quad (5.15)$$

with  $\kappa_1 = 5.9$  and  $\kappa_2 = 0.13$ .

In Section 5.4.2 we anticipated that  $r$  decreases linearly with  $N$ . For  $N = 0$ , the present model should reduce to the unforced model, hence we may pose

$$\kappa_1(N) = \kappa_1 \left( 1 - \lambda_1 \frac{N}{N_{crit}} \right), \quad (5.16)$$

which thus consists of a contribution by the inertial force and a contribution by the magnetic force. From our numerical simulations and fitted model parameters, we determine that  $\lambda_1 = 0.49 \pm 0.02$ .

For the delay time  $\tau$  such a unified approach across both the inertially dominated and electromagnetically dominated regimes is not possible. For  $-N_{crit} < N < 0$  we expect a smaller delay time, since fluid is accelerated in the recirculation zone, and for  $0 < N < N_{crit}$  the fluid is decelerated and we expect the delay time to increase. Hence, for  $|N| < N_{crit}$

$$\kappa_2(N) = \kappa_2 \left( 1 + \lambda_2 \frac{N}{N_{crit}} \right). \quad (5.17)$$

From our numerical simulations and fitted parameters we find that  $\lambda_2 = 0.58 \pm 0.09$ .

For  $N < -N_{crit}$  we use the above observation that  $\delta$  remains close to constant, and hence

we define

$$\tau = \frac{\delta_{min}}{r}, \quad (5.18)$$

with  $\delta_{min} = 1.13$  the average value for  $\delta$  observed in our simulations. Hence, with  $r$  from Equations 5.15 and 5.16,  $\tau$  can be determined.

For given  $N$  we now determine  $k$  from  $r$ ,  $\tau$  and  $\delta$ . For  $|N| < N_{crit}$ , the pair  $(\alpha, \delta)$  resides close to the neutral curve  $\delta_n(\alpha)$  (Equation 5.14), which thus determines  $\alpha$ . For  $N < -N_{crit}$ , we use the above observation from Figure 5.14 that  $\alpha \approx 0.99$ . From  $\alpha$  we determine  $k = \alpha r$ .

$\mu$  follows from the amplitude  $\langle \theta' \rangle$  of the dimensionless form of the DDE model equation (Equation 5.13)<sup>28</sup> and the behavior of  $\langle \theta \rangle$ . For  $N = 0$  we found  $\langle \theta' \rangle = \sqrt{2(1 - \alpha^2)}$ . This also holds for  $|N| < N_{crit}$ . For  $N < -N_{crit}$ , the parameters are no longer distributed along the neutral curve, but given by  $\alpha \approx 0.99$  and  $\delta = 1.13$  above. For this regime we find  $\langle \theta' \rangle = \gamma = 0.61$ .

$$\mu = \begin{cases} \frac{2r(1 - \alpha^2)}{\langle \theta \rangle^2} & \text{if } |N| < N_{crit} \\ \frac{\gamma^2 r}{\langle \theta \rangle^2} & \text{if } N < -N_{crit} \end{cases}, \quad (5.19)$$

Now, for given  $N$ , the model parameters  $r$ ,  $\mu$ ,  $k$  and  $\tau$  can be determined from Equations 5.15 and 5.16, Equation 5.19,  $k = \alpha r$  and Equations 5.15, 5.17 and 5.18, respectively

#### 5.5.4 Model application

Figure 5.15 compares the parameters obtained from the model presented in Equations 5.15-5.19 with the parameters obtained from the fit of the phased-average jet oscillation profiles from the numerical simulations. With this figure we confirm that the present model gives the correct model parameters to determine the jet oscillation properties.

In table 5.1 we compare the frequencies obtained from the LES simulations and the presented zero-dimensional model. The table demonstrates that our model correctly predicts the single jet oscillation frequency along the range  $-6N_{crit} \leq N \leq N_{crit}$ , as is also indicated with Figure 5.16. The deviation is only larger than 10% for the most extreme cases ( $N = N_{crit}$  and  $N = -6N_{crit}$ ), where the first is close to being damped and the latter enhanced, to such an extent that the oscillations become irregular.

In Figure 4.12 we show the numerically obtained jet angle profile and the jet angle profile obtained from the model for several combinations of  $Re$  and  $N$ . The figure demonstrates that the zero-dimensional DDE-type model can successfully be applied on the electromagnetic forcing of a self-sustained oscillating jet, both in the inertia, as in the electromagnetic force dominant regimes. For larger negative  $N$  ( $N = -0.075$ , bottom right in figure 4.12), the forced flow shows irregular behavior, which is observed from the significant variation in period and amplitude during the oscillation. This phenomenon due to the strong amplification

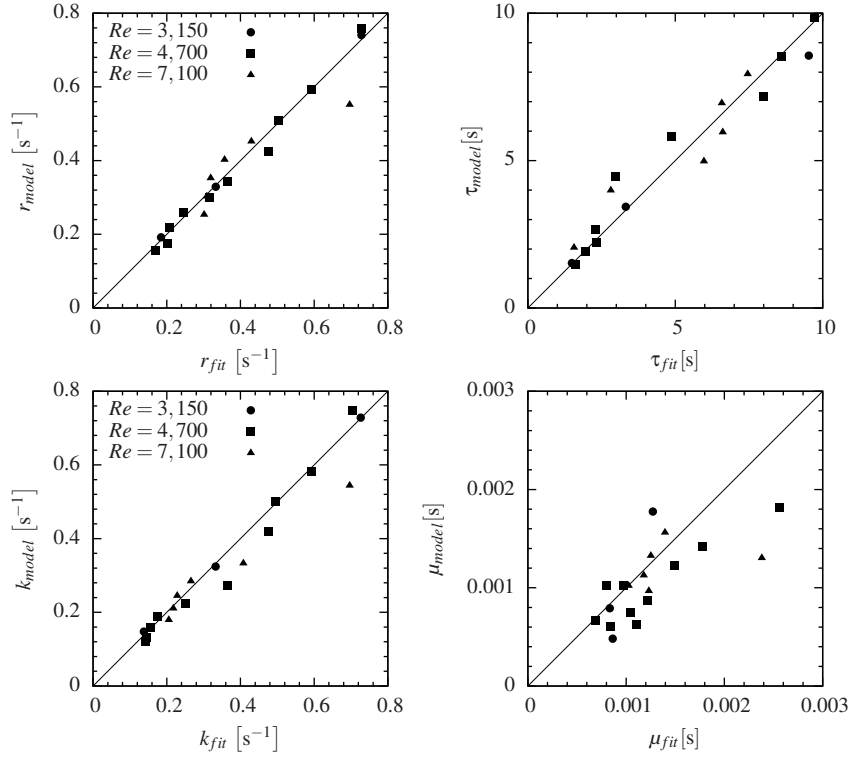


**Figure 5.15** Parity plot for  $r$  (top left),  $\tau$  (top right),  $k$  (bottom left) and  $\mu$  (bottom right) showing the fitted parameter value (horizontal axis) compared to the parameter value obtained from the model (Equations 5.15-5.19).

of the oscillation for large negative  $N$  is not described by the present model. For the other  $N$  however, the presented model shows a good agreement in profile shape and frequency.

## 5.6 Conclusion

We studied the effect of an electromagnetic body force on self-sustained jet oscillations in a confined cavity. Three flow regimes can be distinguished, that are separated by the critical Stuart number  $N_{crit}$ : 1) for  $N > N_{crit}$ , all inertia induced large scale oscillations are suppressed by electromagnetic body forces, 2) for  $|N| < N_{crit}$ , the jet inertia is dominant compared to the electromagnetic force, but the latter influences the jet oscillation in amplitude and frequency, 3) for  $N < -N_{crit}$ , the electromagnetic forces dominate the flow and control the flow oscillations. For the configuration studied in this paper we found  $N_{crit} = 0.013$ .



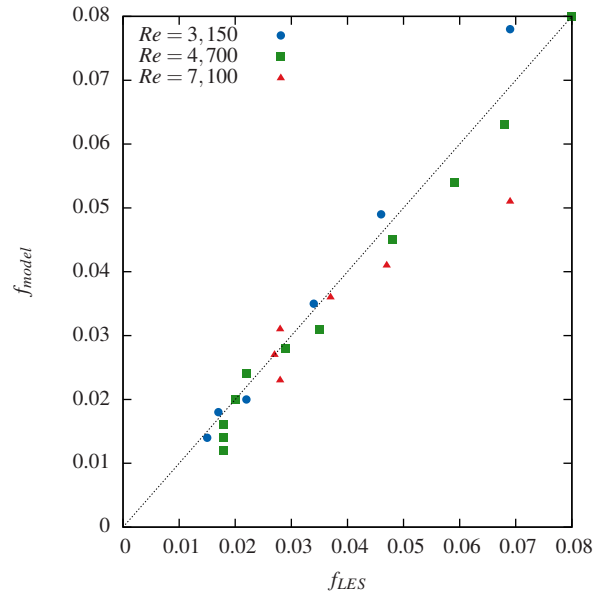


**Figure 5.16** Parity plot for the frequency showing the oscillation frequency obtained from the numerical simulations (horizontal axis) compared to the oscillation frequency obtained from the zero-dimensional model (vertical axis).

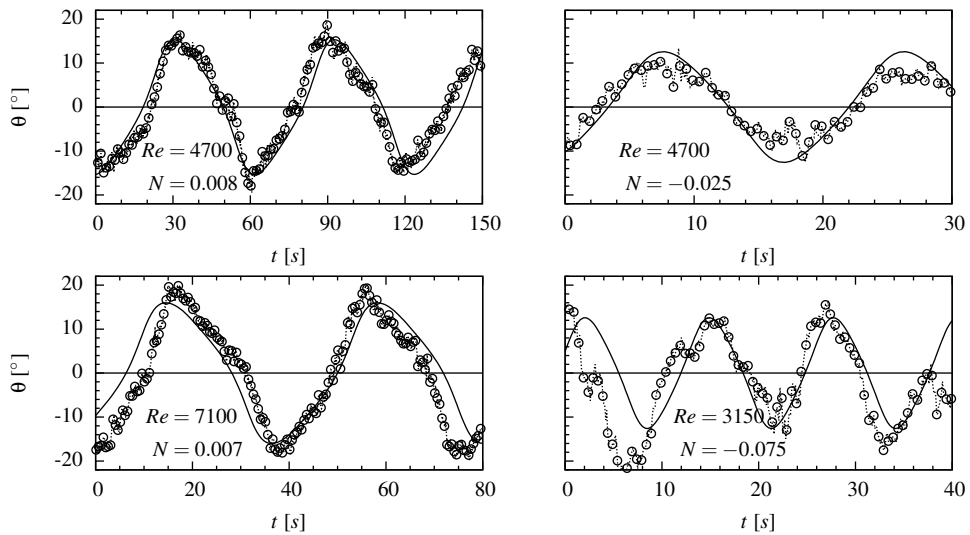


**Figure 5.17** Example model solution (solid line) and the numerical solution (symbols and dashed line) for several combinations of  $Re$  and  $N$ , as indicated in the graphs.

**Table 5.1** This table compares the oscillation frequency obtained from the LES simulations and the zero-dimensional model equation as a function of  $Re$  and  $N$ .

$Re$	$N$	$f_{LES}$ [Hz]	$f_{model}$ [Hz]
3150	-0.075	0.069	0.078
3150	-0.038	0.046	0.049
3150	-0.019	0.034	0.035
3150	-0.005	0.022	0.020
3150	0	0.017	0.018
3150	0.005	0.015	0.014
3150	0.014	—	—
4700	-0.051	0.080	0.080
4700	-0.034	0.068	0.063
4700	-0.026	0.059	0.054
4700	-0.017	0.048	0.045
4700	-0.009	0.035	0.031
4700	-0.004	0.029	0.028
4700	0	0.022	0.024
4700	0.004	0.020	0.020
4700	0.009	0.018	0.016
4700	0.011	0.018	0.014
4700	0.013	0.018	0.012
4700	0.015	—	—
7100	-0.015	0.069	0.051
7100	-0.007	0.047	0.041
7100	-0.004	0.037	0.036
7100	0.0	0.028	0.031
7100	0.004	0.027	0.027
7100	0.007	0.028	0.023

We incorporated the effect of the electromagnetic forcing in a zero-dimensional DDE-type model that describes the jet oscillation. The additional Lorentz force is included in the model by the additional dependence on  $N$ . We have shown that this newly defined model correctly represents the jet oscillation for the Reynolds number  $3150 \leq Re \leq 7100$  and  $-6N_{crit} \leq N \leq N_{crit}$ .

Although this paper only addresses a specific configuration of electromagnetic forcing, we believe that the method can also be applied on different EMBr configurations and even different types of body forces. This means that one can expect to find three regimes, a jet inertia dominated regime, an oscillation enhancing regime and an oscillation suppressing regime. The effect of these forces on the zero-dimensional model for the jet oscillation will be dependent on a dimensionless number describing the ratio of the imposed force and the inertial force.

For large negative  $N$  the oscillations are more irregular with respect to the deviation in the amplitude between periods. The currently presented model does not include this irregularity in the oscillation.

The forced single jet oscillation model also has potential for other types of forced single jet flows, such as jets with a different density, or by application of acoustic forcing.<sup>10,25,35,39,40</sup>

## Bibliography

- [1] Arcos-Gutierrez, H., Barrera-Cardiel, G., Barreto, J. d. J., and Garcia-Hernandez, S. Numerical Study of Internal SEN Design Effects on Jet Oscillations in a Funnel Thin Slab Caster. *ISIJ International*, volume 54(6):pp. 1304–1313 (2014).
- [2] Bouchet, G. and Climent, E. Unsteady behavior of a confined jet in a cavity at moderate Reynolds numbers. *Fluid Dynamics Research*, volume 44(2):p. 025505 (2012).
- [3] Breuer, K., Park, J., and Henoeh, C. Actuation and control of a turbulent channel flow using Lorentz forces. *Physics of Fluids*, volume 16(4):pp. 897–907 (2004).
- [4] Dattarajan, S. and Johari, H. Control of a separating boundary layer with Lorentz force actuators. *Physics of Fluids*, volume 20(4) (2008).
- [5] Garcia-Hernandez, S., Morales, R., De Jess Barreto, J., and Morales-Higa, K. Numerical optimization of nozzle ports to improve the fluidynamics by controlling backflow in a continuous casting slab mold. *ISIJ International*, volume 53(10):pp. 1794–1802 (2013).
- [6] Ha, M. Y., Lee, H. G., and Seong, S. H. Numerical simulation of three-dimensional flow, heat transfer, and solidification of steel in continuous casting mold with electromagnetic brake. *Journal of Materials Processing Technology*, volume 133(3):pp. 322–339 (2003).
- [7] Haiqi, Y., Baofeng, W., Huiqin, L., and Jianchao, L. Influence of electromagnetic brake on flow field of liquid steel in the slab continuous casting mold. *Journal of Materials Processing Technology*, volume 202(1-3):pp. 179–187 (2008).
- [8] Henoeh, C. and Stace, J. Experimental investigation of a salt water turbulent boundary layer modified by an applied streamwise magnetohydrodynamic body force. *Physics of Fluids*, volume 7(6):pp. 1371–1383 (1995).
- [9] Issa, R. I. Solution of the implicitly discretised fluid flow equations by operator-splitting. *Journal of Computational Physics*, volume 62(1):pp. 40–65 (1986).
- [10] Juniper, M., Li, L., and Nichols, J. Forcing of self-excited round jet diffusion flames. *Proceedings of the Combustion Institute*, volume 32 I:pp. 1191–1198 (2009).
- [11] Kalter, R., Righolt, B. W., Kenjereš, S., Kleijn, C. R., and Tummers, M. J. Experimental Modeling of Heat Transfer in a Continuous Casting Mould Model. p. V01CT16A005. ASME (2014).
- [12] Kalter, R., Tummers, M., Kenjereš, S., Righolt, B., and Kleijn, C. Oscillations of the fluid flow and the free surface in a cavity with a submerged bifurcated nozzle. *International Journal of Heat and Fluid Flow*, volume 44:pp. 365–374 (2013).
- [13] Kalter, R., Tummers, M. J., Kenjereš, S., Righolt, B. W., and Kleijn, C. R. Effects of electromagnetic forcing on self-sustained jet oscillations. *Physics of Fluids*, volume 26(6):p. 065101 (2014).
- [14] Kalter, R., Tummers, M. J., Kenjereš, S., Righolt, B. W., and Kleijn, C. R. Electromagnetic flow control of a bifurcated jet in a rectangular cavity. *International Journal of Heat and Fluid Flow*, volume 47:pp. 113–122 (2014).
- [15] Kenjereš, S. Electromagnetic enhancement of turbulent heat transfer. *Physical Review E*, volume 78(6):p. 066309 (2008).

- [16] Kenjereš, S. Large eddy simulations of targeted electromagnetic control of buoyancy-driven turbulent flow in a slender enclosure. *Theor. Comput. Fluid Dyn.*, volume 23(6):pp. 471–489 (2009).
- [17] Kenjereš, S. and Hanjalić, K. On the implementation of effects of Lorentz force in turbulence closure models. *International Journal of Heat and Fluid Flow*, volume 21(3):pp. 329–337 (2000).
- [18] Knaepen, B. and Moin, P. Large-eddy simulation of conductive flows at low magnetic Reynolds number. *Physics of Fluids*, volume 16(5):p. 1255 (2004).
- [19] Kolšek, T., Jelić, N., and Duhovnik, J. Numerical study of flow asymmetry and self-sustained jet oscillations in geometrically symmetric cavities. *Applied Mathematical Modelling*, volume 31(10):pp. 2355–2373 (2007).
- [20] Lawson, N. and Davidson, M. Self-Sustained Oscillation of a Submerged Jet in a Thin Rectangular Cavity. *Journal of Fluids and Structures*, volume 15(1):pp. 59–81 (2001).
- [21] Lee, C. and Kim, J. Control of the viscous sublayer for drag reduction. *Physics of Fluids*, volume 14(7):pp. 2523–2529 (2002).
- [22] Mataoui, A. and Schiestel, R. Unsteady phenomena of an oscillating turbulent jet flow inside a cavity: Effect of aspect ratio. *Journal of Fluids and Structures*, volume 25(1):pp. 60–79 (2009).
- [23] Maurel, A., Ern, P., Zielinska, B. J. A., and Wesfreid, J. E. Experimental study of self-sustained oscillations in a confined jet. *Physical Review E*, volume 54(4):pp. 3643–3651 (1996).
- [24] Molloy, N. A. and Taylor, P. L. Oscillatory Flow of a Jet into a Blind Cavity. *Nature*, volume 224(5225):pp. 1192–1194 (1969).
- [25] Monkewitz, P. A., Bechert, D. W., Barsikow, B., and Lehmann, B. Self-excited oscillations and mixing in a heated round jet. *Journal of Fluid Mechanics*, volume 213:pp. 611–639 (1990).
- [26] Pang, J. and Choi, K.-S. Turbulent drag reduction by Lorentz force oscillation. *Physics of Fluids*, volume 16(5):pp. L35–L38 (2004).
- [27] Peng, X., Zhou, J., and Qin, Y. Improvement of the temperature distribution in continuous casting moulds through the rearrangement of the cooling water slots. *Journal of Materials Processing Technology*, volume 167(2-3):pp. 508–514 (2005).
- [28] Righolt, B. W., Kenjereš, S., Kalter, R., Tummers, M. J., and Kleijn, C. R. Dynamics of an oscillating turbulent jet in a confined cavity. *Physics of Fluids*, volume 27:p. 095107 (2015).
- [29] Rossi, L. and Thibault, J.-P. Investigation of wall normal electromagnetic actuator for seawater flow control. *Journal of Turbulence*, volume 3:p. N5 (2002).
- [30] Shatrov, V. and Gerbeth, G. Electromagnetic flow control leading to a strong drag reduction of a sphere. *Fluid Dynamics Research*, volume 36(3):p. 153 (2005).
- [31] Shatrov, V. and Gerbeth, G. Magnetohydrodynamic drag reduction and its efficiency. *Physics of Fluids*, volume 19(3) (2007).
- [32] Suarez, M. and Schopf, P. A delayed action oscillator for ENSO. *Journal of the Atmospheric Sciences*, volume 45(21):pp. 3283–3287 (1988).
- [33] Thomas Honeyands and Joe Herbertson. Flow dynamics in thin slab caster moulds. *Steel Research International*, volume 66(7):pp. 287–293 (1995).
- [34] Villiermaux, E. and Hopfinger, E. Self-sustained oscillations of a confined jet: a case study for the non-linear delayed saturation model. *Physica D: Nonlinear Phenomena*, volume 72(3):pp. 230–243 (1994).
- [35] Voropayev, S., Nath, C., and Fernando, H. Mixing by turbulent buoyant jets in slender containers. *Physics Letters, Section A: General, Atomic and Solid State Physics*, volume 376(45):pp. 3213–3218 (2012).
- [36] Votyakov, E. V., Zienicke, E., and Kolesnikov, Y. B. Constrained Flow Around a Magnetic Obstacle. *Journal of Fluid Mechanics*, volume 610:pp. 131–156 (2008).
- [37] Weier, T., Gerbeth, G., Mutschke, G., Lielausis, O., and Lammers, G. Control of Flow Separation Using Electromagnetic Forces. *Flow, Turbulence and Combustion*, volume 71(1):pp. 5–17 (2003).

**Table 5.2** The properties of the three magnets contributing to the magnetic field imposed in the numerical simulations.

	Magnet 1	Magnet 2	Magnet 3
$(M_x, M_y, h)$	(0.04, 0.084, 0.04) m	(0.042, 0.08, 0.04) m	(0.04, 0.084, 0.04) m
$(x_c, y_c, z_c)$	(-0.078, -0.15, 0.01) m	(0.0, -0.15, 0.01) m	(0.078, -0.15, 0.01) m
$B_{face}$	-0.55 T	0.65 T	-0.55 T

- [38] Weller, H. G., Tabor, G., Jasak, H., and Fureby, C. A tensorial approach to computational continuum mechanics using object-oriented techniques. *Computers in Physics*, volume 12(6):pp. 620–631 (1998).
- [39] Yu, M., Lin, T., and Hsieh, Y. Influence of acoustic forcing on the near field development of a heated plane jet. *Experimental Thermal and Fluid Science*, volume 25(1-2):pp. 13–22 (2001).
- [40] Zhang, C., Eckert, S., and Gerbeth, G. The Flow Structure of a Bubble-Driven Liquid-Metal Jet in a Horizontal Magnetic Field. *Journal of Fluid Mechanics*, volume 575:pp. 57–82 (2007).
- [41] Zhang, L., Rong, Y.-M., Shen, H.-F., and Huang, T.-Y. Solidification modeling in continuous casting by finite point method. *Journal of Materials Processing Technology*, volume 192-193:pp. 511–517 (2007).

## 5.A Electromagnetic field

The analytical expression for the imposed magnetic field, is based on the algebraic calculations by Votyakov et al.:

$$B_x(x, y, z) = \frac{1}{B_0} \sum_{k=\pm 1} \sum_{j=\pm 1} \sum_{i=\pm 1} (ijk) \operatorname{arctanh} \left[ \frac{y - jM_y}{r(i, j, k)} \right], \quad (5.20)$$

$$B_y(x, y, z) = \frac{1}{B_0} \sum_{k=\pm 1} \sum_{j=\pm 1} \sum_{i=\pm 1} (ijk) \operatorname{arctanh} \left[ \frac{x - iM_x}{r(i, j, k)} \right], \quad (5.21)$$

$$B_z(x, y, z) = -\frac{1}{B_0} \sum_{k=\pm 1} \sum_{j=\pm 1} \sum_{i=\pm 1} (ijk) \operatorname{arctan} \left[ \frac{(x - iM_x)(y - jM_y)}{(z - kh)r(i, j, k)} \right]. \quad (5.22)$$

Here  $r(i, j, k) = [(x - iM_x)^2 + (y - jM_y)^2 + (z - kh)^2]^{1/2}$  and  $B_0$  is such that  $B_z(0, 0, 0) = 1$ . This follows from an integral over the region  $\Omega = \{|x| \leq M_x, |y| \leq M_y, h \leq |z| \leq \infty\}$  of magnetic dipoles, i.e., two magnets of dimensions  $2M_x \times 2M_y$  separated by  $2h$ , connected by a soft core.

In the present work, three magnets are positioned on one side of the cavity. Therefore, the summation over  $k = +1$  can be omitted from above summation, whereas the summation is carried out over three separate magnets, with their origin in  $(x_c, y_c, z_c)$  and certain magnitude. The resulting properties for the magnets are summarized in table 5.2. As the magnets are positioned on one side, the normalization of the magnetic field was handled with respect to the face of the magnet, rather than the origin.





# 6. Dynamics of a bifurcated jet in a confined cavity with a free surface<sup>§</sup>

## 6.1 Introduction

A single fluid jet that is confined in the two directions perpendicular to the flow, may exhibit self-sustained oscillations under specific conditions.<sup>10,15</sup> Those jet oscillations are observed for jet Reynolds numbers ranging from  $Re = 100$ <sup>13</sup> up to  $Re = 170,000$ .<sup>14</sup> For one of the spanwise directions sufficiently wide, as compared to the nozzle diameter (i.e.  $W/d \geq 20$ ), the jet oscillation can be described by three stages, where the formation of recirculation zones at both sides of the jet plays a major role. First, the jet is slightly deflected to, say, the right. This feeds more flow to the recirculation zone on the right, which now becomes stronger, with an increasing pressure deficit in the center of the recirculation. This causes a further jet deflection to the right as it is limited by the geometry. Second the jet deflection reaches a maximum amplitude and the pressure deficit does not decrease any further, which means that the driving force of the jet deflection vanishes. Third, at the right wall, the downward flow will increase, causing the growth of a recirculation zone at the left of the jet and a diminishing pressure deficit at its right. This results in the jet moving towards the left. The process then repeats.<sup>15</sup>

Self-sustained oscillations are also observed for situations in which a bifurcated jet is confined in a thin cavity. A bifurcated jet originates from a nozzle with two ports (as schematically depicted in Figure 6.1), hence resulting in two jets discharging into the cavity in more or less opposite directions.

Such a confined bifurcated jet configuration is relevant in, for example, continuous steel

---

<sup>§</sup>Parts of this chapter published as: Righolt, B. W., Kenjereš, S., Kalter, R., Tummers, M. J., and Kleijn, C. R. Numerical study of turbulent submerged bifurcated jets impingement and interactions with a free surface. In: *8th International Symposium on Turbulence and Shear Flow Phenomena, TSFP Proceedings*. 2013.



casting. Two- or four-port nozzles are commonly used for the injection of hot, liquid steel into the casting mould in order to obtain an optimal distribution of the fluid with respect to the quality of the resulting solidified steel slab. Oscillations as described above are an unwanted side-effect of the fluidic system under consideration.

Numerical simulations, sometimes coupled with water model experiments, are commonly used to study the continuous steel casting process. Simulation studies generally apply various simplifications, focussing on either cooling or solidification of the steel,<sup>11</sup> the movement of the free surface<sup>17,18,23</sup> or the electromagnetic brake.<sup>4,5,19,21</sup> Sometimes the focus is on the pure flow mechanics only.<sup>3</sup> As direct Numerical Simulations (DNS) are not computationally feasible due to the high ( $> 10000$ ) jet Reynolds numbers, such studies rely on RANS, T-RANS and LES for the modelling of turbulence.

From water model experiments, Torres-Alonso et al.<sup>17,18</sup> report dynamic free surface distortions with a duration of 10 s and a frequency of 0.01 Hz. They numerically predict this distortion using a Reynolds Stress Model. The origin of the distortion is found in the interaction between both jets below the nozzle tips. The origin of the large period of the distortion is the high Reynolds stresses at the boundary of the jet and the upper recirculation zones. The frequency of the jet oscillations matches the frequency of the free surface oscillations.

Honeyands and Herbertson<sup>9</sup> and Kalter et al.<sup>10</sup> propose a mechanism for the self-sustained oscillation of bifurcated jets in a thin cavity. Similar to the self-sustained oscillations of a single jet in a cavity, the confinement of the liquid jets in both directions perpendicular to the flow is an essential prerequisite for the oscillation to exist, leading to the necessary formation of recirculation zones in the domain. The pressures in the recirculation zones play a role in the proposed mechanism. Furthermore, the oscillations of the two jets will align in anti-phase, due to the interaction between both sides of the domain.

The goal of the present work is to provide thorough proof for the mechanism of the self-sustained oscillation in a bifurcated jet configuration in a thin cavity, as proposed by Honeyands and Herbertson<sup>9</sup> and Kalter et al.<sup>10</sup> by means of numerical simulations. These simulations can provide detailed pressure fields, which are difficult to obtain experimentally.

## 6.2 Numerical method and validation

### 6.2.1 Description of the set-up

The model geometry, shown in Figure 6.1, consists of a thin cavity, with dimensions  $0.65 \times 0.8 \times 0.035 \text{ m}^3$  ( $= W \times H \times T = \text{width} \times \text{height} \times \text{thickness}$ ). The cavity is filled up to a height  $h = 0.7 \text{ m}$  with water, with  $\rho = 1.0 \times 10^3 \text{ kg/m}^3$  and kinematic viscosity  $\nu = 1.0 \times 10^{-6} \text{ m}^2/\text{s}$ . The water-air interfacial tension is  $\sigma = 0.07 \text{ N/m}$ . The fluid emerges from the nozzle through two vertical openings of inner dimensions  $d^2 = 0.01 \times 0.01 \text{ m}^2$  on opposite sides of the nozzle (see Figure 6.1). The nozzle submergence depth, which is

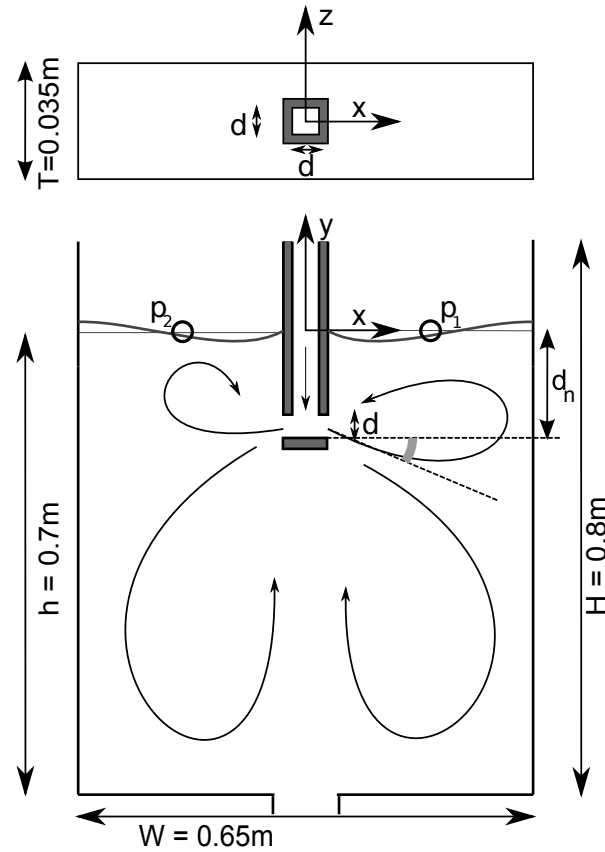


**Figure 6.1** The schematics of the setup considered in this paper is depicted. A top view (top) and side view (bottom) of the cavity of dimension  $W \times H \times T = 0.8 \times 0.65 \times 0.035 \text{ m}^3$  is shown. The nozzle is submerged by  $d_n = 0.125 \text{ m}$  and has inner diameter  $0.01 \text{ m}$  and a wall thickness of  $0.005 \text{ m}$ . The fluid depth  $h = 0.7 \text{ m}$ . Furthermore,  $p_1$  and  $p_2$  indicate two monitoring points at  $x = \pm 0.175 \text{ m}$  and the gray angle indicates the jet angle.

the distance between the equilibrium water-air surface and inner bottom of the nozzle, is  $d_n = 0.125 \text{ m}$ .

The Reynolds number is based on the average velocity,  $v_{in}$  of each of the jets emerging from the nozzle and the nozzle diameter as  $Re_{jet} = v_{in}d/\nu = 12,500$ . The average velocity in the inlet pipe is thus  $2v_{in}$ . A Cartesian coordinate system is defined as depicted in Figure 6.1, where the origin is located in the center of the inlet pipe at the position of the equilibrium free surface, where the  $x$  coordinate is along the width, the  $y$  coordinate along the height and the  $z$  coordinate along the depth of the cavity.

In this work, we solve the incompressible, two-phase (Volume Of Fluid), LES filtered Navier-Stokes equations and the transport equation for the indicator function  $\alpha$ ,<sup>7,16,20</sup>

$$\frac{\partial \rho v_i}{\partial t} + v_j \frac{\partial \rho v_i}{\partial x_j} = \frac{\partial}{\partial x_j} \left[ (\mu + \mu_t) \left( \frac{\partial v_i}{\partial x_j} + \frac{\partial v_j}{\partial x_i} \right) \right] - \frac{\partial p}{\partial x_i} + f_i + \gamma \kappa \frac{\partial \alpha}{\partial x_i}, \quad (6.1)$$

$$\frac{\partial \alpha}{\partial t} + \frac{\partial}{\partial x_j} (\alpha v_j) + \frac{\partial}{\partial x_j} (v_{r,j} \alpha (1 - \alpha)) = 0. \quad (6.2)$$

In these equations,  $\alpha$  has value 1 in cells containing the liquid phase only and 0 for the gas phase, whereas intermediate values of  $\alpha$  indicate the position of the free surface. Furthermore,  $\rho = \alpha \rho_1 + (1 - \alpha) \rho_2$  is the phase averaged density,  $\mu$  the phase averaged dynamic viscosity,  $\mu_t$  the turbulent viscosity,  $v_i$  the velocity,  $p$  the pressure,  $f_i$  the gravitational force,  $\sigma$  the surface tension between both phases and  $\kappa$  the curvature of the interface, which is calculated as  $\kappa = \nabla \alpha / |\nabla \alpha|$ .<sup>2</sup> The third term in the transport equation for  $\alpha$  represents an interface compression, which is intended to maintain the interface as sharp as possible.<sup>1,8</sup>

The turbulent viscosity  $\mu_t$  is obtained from the dynamic Smagorinsky model, a Large Eddy Simulation (LES) model.

$$\frac{\mu_t}{\rho} = \nu_{SGS} = (C\Delta)^2 \mathcal{S}, \quad (6.3)$$

where  $\Delta$  is the local grid size, defined as  $\Delta = (\Delta_x \Delta_y \Delta_z)^{1/3}$ .  $\mathcal{S}$  is the characteristic rate of strain  $\mathcal{S} = (2S_{ij}S_{ij})^{1/2}$  with  $S_{ij} = (\partial v_i / \partial x_j + \partial v_j / \partial x_i) / 2$ .  $C$  is the Smagorinsky constant,  $C = \langle L_{ij} M_{ij} \rangle / 2 \langle M_{ij}^2 \rangle$ , with the resolved stress tensor  $L_{ij} = \widetilde{v_i v_j} - \widetilde{v_i} \widetilde{v_j}$  and  $M_{ij} = 2\Delta^2 \widetilde{\mathcal{S} S_{ij}} - 2(2\Delta)^2 \widetilde{\mathcal{S}} \widetilde{S_{ij}}$ , where  $\widetilde{\cdot}$  indicates the filtering operation.

To reduce computational instabilities due to local small values of  $M_{ij}^2$ , we follow the recommendation by Lilly<sup>12</sup>, and apply local averaging ( $\langle \cdot \rangle$ ), using the approach by Zang et al.<sup>22</sup>, which means averaging over three control volumes in every direction, whereas the total viscosity is clipped at  $\nu + \nu_{SGS} = 0$ .

The orthogonal, rectangular, uniform grid consists of  $520 \times 640 \times 28 \approx 9.4 \times 10^6$  control volumes. For time integration, a second order implicit scheme is used, with a time-step obtained from the lowest of the Courant criterion  $\max(Co = u\Delta t / \Delta x) = 0.6$  or  $\max(Co_\alpha = u\Delta t / \Delta x) = 0.2$  for regions where  $0.01 < \alpha < 0.99$ . The convective and diffusive terms are discretized using a second order central differencing scheme.

As  $y^+$  at the walls might reach local peak values as high as  $y^+ \approx 40$  and local minimum values as low as  $y^+ \approx 0.01$ , we imposed the universal Spalding's law as a boundary condition (see section 2.7 for details). Furthermore, the inflow for the nozzle is a periodic domain of length  $10d$ , which guarantees fully developed inflow conditions. The volumetric flow rate at the outlet was fixed at a value equal to the volumetric flow rate at the inlet in order to maintain the correct liquid level in the domain throughout the simulation.

The frequency of the self-sustained oscillations for the numerical simulation is  $f_{sim} = 0.14$  Hz, which is invariant under refining the mesh in the high-velocity regions by a factor

2 in each direction, resulting in  $13.6 \times 10^6$  control volumes. The numerically obtained frequency is insensitive to  $\pm 10\%$  changes in viscosity and changes only by about 0.01 Hz for 0.01 m changes in the nozzle depth. The frequency obtained from the experiment differs about 35% from the numerically obtained frequency,  $f_{exp} = 0.09$  Hz.<sup>10</sup> Despite this difference, we believe that our numerical simulation reflects the correct physics behind the oscillation mechanism. This belief stems from the good agreement with experiments when looking at the time averaged and instantaneous flow patterns in Figures 6.2 and 6.3. Figure 6.2 shows vectors of the time-averaged velocity in the upper right corner of the domain and contours of the  $z$ -component of the vorticity, demonstrating a reasonable agreement between our experiments and simulations. Furthermore, Figure 6.3 shows snapshots of the instantaneous velocity distributions for both the numerical simulations and the experiments. When the time axis is non-dimensionalized with the oscillation period, this figure shows a good agreement between experiment and simulation during the different stages of the oscillation.

### 6.3 Oscillation mechanism free surface

Hypotheses for the mechanism behind self-sustained oscillations of a bifurcated jet flow in a confined cavity have been proposed by Honeyands and Herbertson<sup>9</sup> and Kalter et al.<sup>10</sup>. They describe the oscillation in four consecutive stages. These stages are depicted in Figure 6.3. In the next sections, we will describe these four stages, and provide detailed proof for the mechanism based on numerical simulations.

#### 6.3.1 Jet splitting

In the first stage ( $t/\mathcal{T} = 0$ ), the jet is oriented towards the right side, as can be seen from Figure 6.3 (top). The jet impinges on the right wall, and splits into an upward flow, feeding a recirculation zone at the upper right, and a downward directed flow. As can be seen from this figure, the upper right recirculation zone is large, and at this point in time, also its center is at its furthest right position. This can also be seen from Figure 6.4, where the  $x$ -coordinate of the center of the recirculation zone is shown as a function of time, for both the numerical simulation and the experiment. This center of the recirculation zone is determined from the local maximum of the function  $\Gamma_1(\vec{x})$  proposed by Graftieaux et al.<sup>6</sup>:

$$\Gamma_1(\vec{x}) = \frac{1}{N} \sum_{i=1}^N \frac{|(\vec{x} - \vec{x}_i) \times \vec{u}(\vec{x}_i)|}{|(\vec{x} - \vec{x}_i)| |\vec{u}(\vec{x}_i)|}, \quad (6.4)$$

where the summation runs over  $N$  points  $\vec{x}_i$  within 4 mm of the point  $\vec{x}$ .

The upper left Figure 6.3 also shows the pressure deficit in the recirculation zone, which pulls the jet further upward. The minimum pressure in each of the four recirculation zones is shown as a function of time in Figure 6.5. From this figure we observe that the pressure deficit at the upper right is in a minimum in this stage of the oscillation around  $t/\mathcal{T} = 0$ .

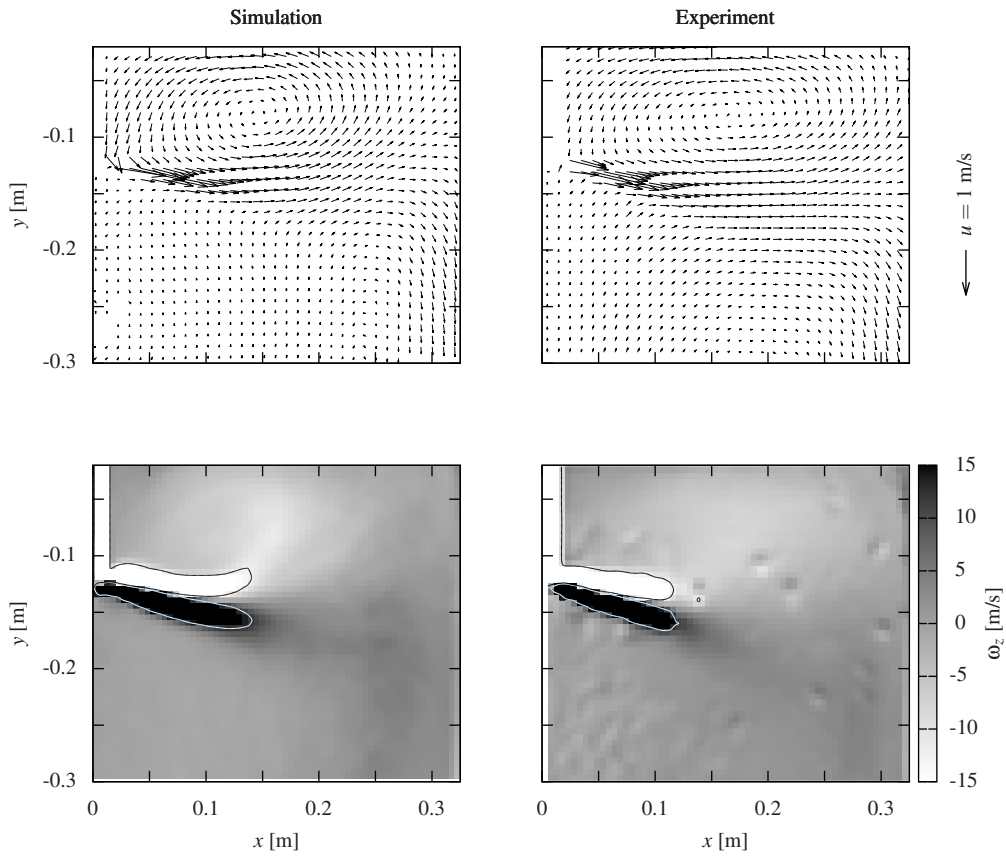


**Figure 6.2** Comparison between the mean velocity from the simulation (left) and the experiment (right) in the  $z = 0$ -plane. (top) vectors of the mean velocity, (bottom) contours of the  $z$ -component of the vorticity,  $\omega_z = \frac{\partial u}{\partial y} - \frac{\partial v}{\partial x}$ .

### 6.3.2 Pressure deficit growth

In the second stage ( $t/\mathcal{T} = 0.2$ ), the jet moves further upward, reducing the space available for the recirculation zone. As a result the velocities and pressure deficit in the recirculation zone further increase. Also, the center of the recirculation zone moves to the left, i.e. towards the nozzle. This horizontal movement of the recirculation zone centre is also shown in Figure 6.4. The development of the pressure deficit as a function of time is shown in Figure 6.5.

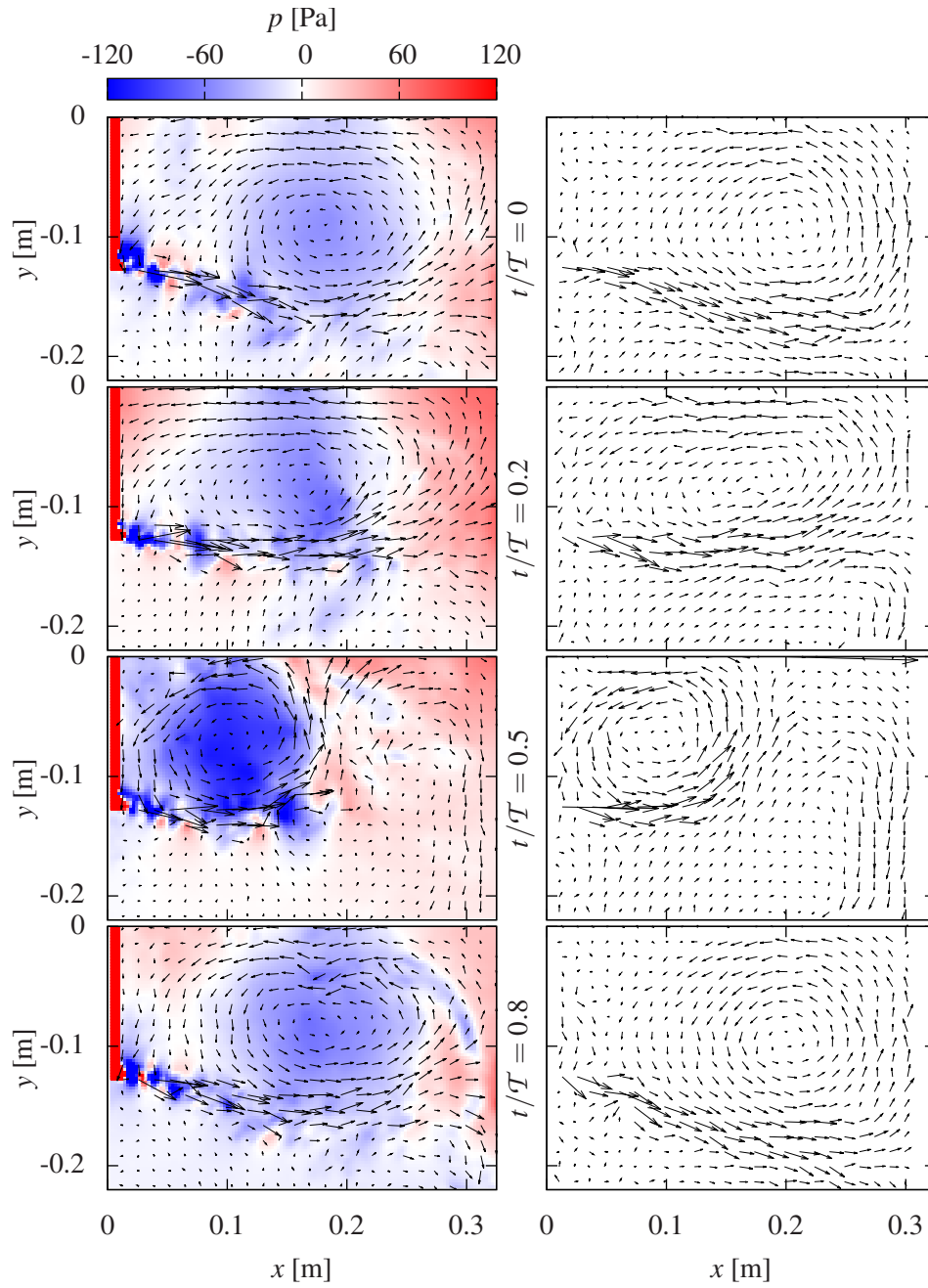


**Figure 6.3** Vector fields of the instantaneous velocity in the  $z = 0$ -plane during the four phases (top to bottom) of the self-sustained oscillation, for the numerical simulation result in conjunction with contours of the pressure (left) and for the experiment, obtained from PIV (right).

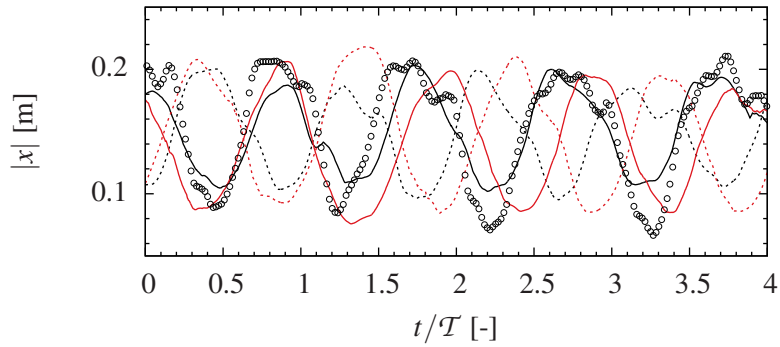


**Figure 6.4** The distance between the nozzle centerline and the center of the recirculation zone in the  $z = 0$ -plane, for the numerical simulation (upper right recirculation zone (solid black), upper left recirculation zone (dashed black)), for the experiment (upper right recirculation zone, symbols) and for the numerical simulation with a fixed top wall (upper right (solid red), upper left (dashed red)).

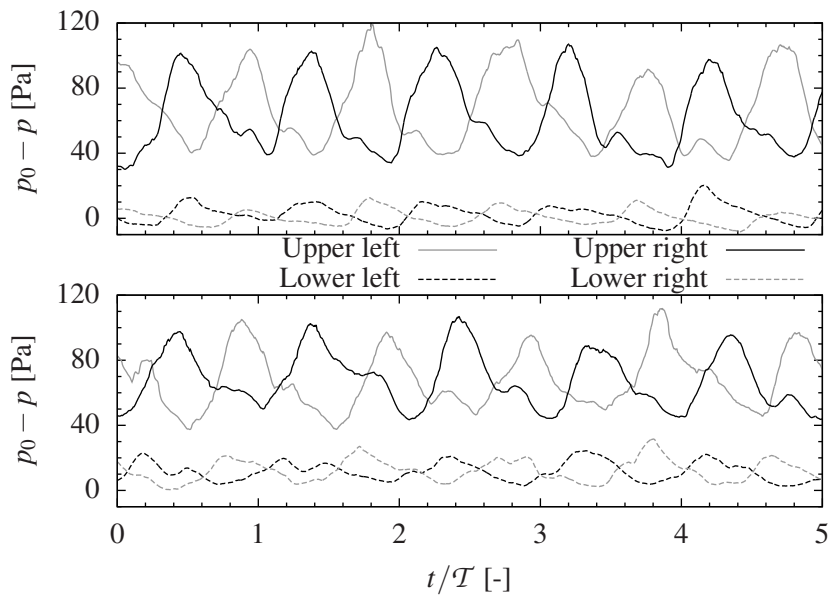


**Figure 6.5** The difference between the ambient pressure  $p_0$  and the minimum pressure in each of the four recirculation zones as a function of time for the free surface (top) and solid wall (bottom). The time axis is in correspondence with the previous figures.

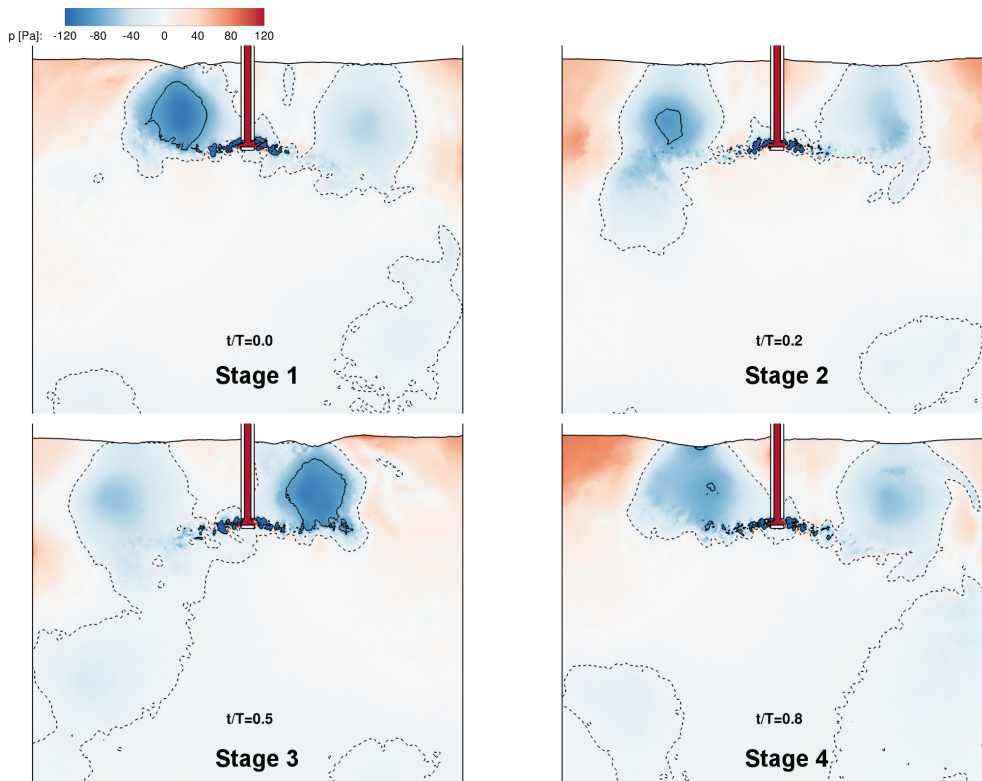


**Figure 6.6** Contours of the pressure  $p$  during four stages of the bifurcated jet oscillation for the full width of the domain. The free surface position is indicated by a solid black line. In the figure, we indicated the iso-contours for  $p = -80$  Pa and  $p = -10$  Pa.

### 6.3.3 Maximum pressure deficit and fluid overshoot

In the third stage ( $t/T = 0.5$ ), the upper right recirculation zone reaches an extreme position closest to the nozzle (see Figures 6.3 (third row) and 6.4), with the pressure deficit reaching a maximum (Figure 6.5).

The pressure deficit in the center of the recirculation zone also affects the free surface. This can be seen from Figure 6.6, which shows the pressure in the  $z = 0$ -plane in conjunction with the position of the free surface. From Figure 6.6 (bottom left), it follows that the pressure deficit in the recirculation zone causes a local minimum of the free surface elevation. In probe location  $p_1$ , the elevation shows a maximum in this stage as follows from Figure 6.7.

Simultaneously, a minimum pressure deficit is reached in the recirculation zone in the upper left (see Figure 6.5 and 6.6), which is in the same state as the upper right recirculation zone



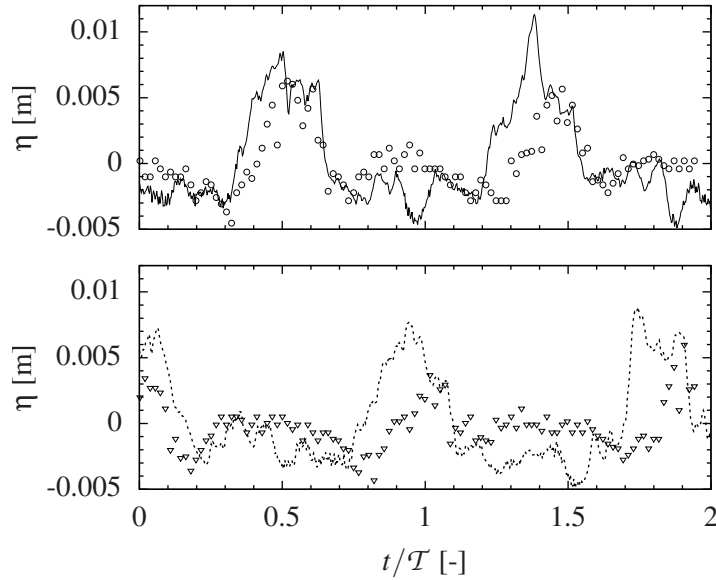


**Figure 6.7** The free surface elevation at the monitoring locations  $p_1$  (top) and  $p_2$  (bottom), as indicated in Figure 6.1 as a function of time for the numerical simulation (lines) and the experiment (symbols). The free surface elevation for the numerical simulation is obtained by averaging the free surface elevation in the  $z$ -direction.

during stage 1. From Figure 6.4, it follows that the system is in an anti-symmetric oscillation, i.e. when the upper left recirculation zone moves towards the nozzle, the upper right recirculation zone moves away from the nozzle and vice versa. This means that both recirculation zones move towards the right (or left) simultaneously. Figure 6.7 demonstrates that the same anti-symmetric oscillation is also visible in the elevation of the free surface on opposite sides of the domain.

It was observed by Kalter et al.<sup>10</sup>, that the overshoot of fluid, from the left side of the cavity to the right, or vice versa, through the gaps between the nozzle and the front and back wall, plays an elementary role in this stage. We identify the mass flow through the gaps between front and back wall in Figure 6.8. The mass flow is defined through the plane  $x = 0$  and  $y \geq -0.15$  m. It follows from this figure that, approximately halfway the period, the sign of the mass flow changes direction when the recirculation zones are in extreme positions. In other words, the cross flow through the gap between nozzle and front and back wall is in the same direction as the movement of the recirculation zones, indicating the strong coupling between both.

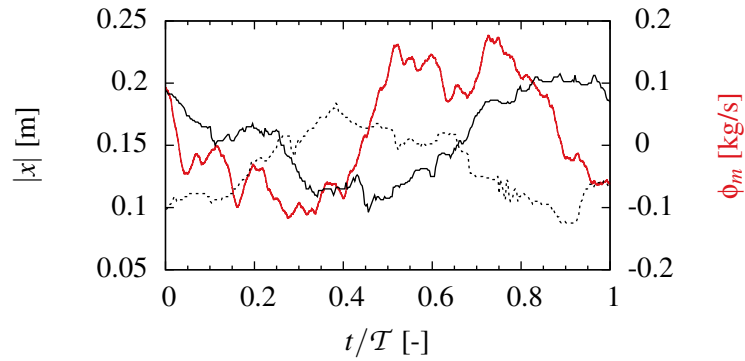


**Figure 6.8** The distance between the nozzle centerline and the center of the recirculation zone in the  $z = 0$ -plane for a single period for the numerical simulation for the upper right recirculation zone (solid black line), the upper left recirculation zone (dashed black line). The red line indicates the mass flow rate (positive from left to right) through the gaps between the nozzle pipe and the front and back wall ( $x = 0, y \geq -0.13$  m).

### 6.3.4 Pressure deficit decrease

In the fourth stage, the upper right recirculation zone collapses rapidly, aided by the liquid overshoot from the left to the right which pushes the recirculation zone away from the nozzle. As a result the pressure deficit in the upper right recirculation zone quickly decreases (see Figure 6.5). The pressure deficit at the upper left as well as at the lower right increases (see Figures 6.5 and 6.6). The jet now moves downwards and the recirculation zone moves away from the nozzle, until it reaches the first stage and the process repeats.

## 6.4 Influence of a wall

It might be questioned whether the free surface is essential in maintaining the self-sustained oscillation of the bifurcated jet flow. In this section we will show that the anti-symmetric oscillation of the bifurcated jet configuration in a thin cavity is also present when a solid wall is placed on top of the domain, thus suppressing the free surface oscillations. Therefore, the free surface is not a requisite for the self-sustained oscillations to exist.

The occurrence of the self-sustained, anti-symmetric oscillation in the presence of a top wall is readily confirmed from Figures 6.4 and 6.9, which show the distance between the nozzle and the centres of the recirculation zones at the upper left and upper right of the domain, and the pressure fields in the full domain respectively. From Figure 6.9 we can see the same four stages as discussed for the case with a free surface. So, in general, the mechanism for the self-sustained oscillation is the same with and without the presence of a free surface.

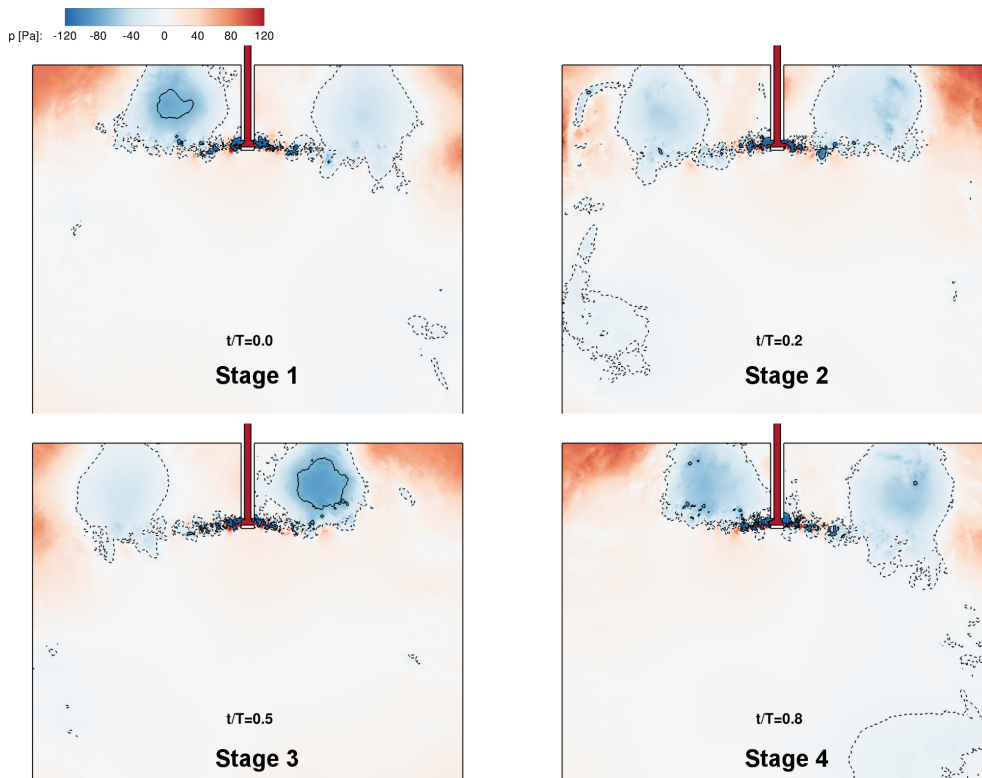


**Figure 6.9** Contours of the pressure  $p$  during the four stages of the bifurcated jet oscillation for a domain without a free surface, but a fixed wall covering the top part of the domain. The iso-contours indicate  $p = -70$  Pa (solid) and  $p = -10$  Pa (dashed).

However, comparing the self-sustained oscillations for the free surface cavity and the fixed wall cavity, differences can be observed. The first difference can be observed from the comparison of Figures 6.6 and 6.9. We observe that, apart from the pressure deficits in the center of the recirculation zone, there are local peaks in the pressure in the upper left and upper right corner of the domain. For the fixed wall case, these peak pressures are higher than for the free surface case, which can be explained by the fact the high pressure elevates the free surface, therefore relieving the pressure a bit. This can be confirmed from Figure 6.6, where the highest elevation is reached near both side walls, especially so when the pressure underneath the free surface is relatively high. At the same time, the pressure minimum in the center of the recirculation zone causes the free surface to lower, accelerate the fluid a bit more, thus causing an even lower pressure minimum. This can be seen from Figure 6.6 (stage 1, left side and stage 3 right side), where the minimum free surface elevation is located directly above the center of the recirculation zone, where the pressure is lowest.

A second difference can be related to the larger pressure gradients in the domain for the fixed wall case and is observed from Figure 6.4, which shows the distances between the nozzle and the center of each recirculation zone. It follows from this figure that the recirculation zone moves significantly closer to the nozzle when a fixed wall is present at the top. The larger pressure gradients in the top of the domain, eventually represented as a force on the recirculation zone, explains this larger amplitude oscillation of the recirculation zone center.

## 6.5 Conclusion

In this chapter we have studied the oscillation mechanism of a bifurcated jet configuration in a confined cavity by means of numerical simulations. The sideways oriented jets form two strong recirculation zones in the upper left and upper right of the domain. The positions and strengths of these recirculation zones oscillate in anti-phase causing an oscillation in the free surface. In this chapter we have shown proof for a mechanism that explains the presence of these self-sustained oscillations from the growing and shrinking pressure deficits in these two recirculation zones. As the jet on one side of the cavity moves upwards, the recirculation zone will move towards the nozzle, which simultaneously causes the pressure deficit inside this recirculation zone to increase, until a maximum pressure deficit is reached and the recirculation zone collapses.

The free surface elevation profiles follow the trend of the pressure differences across the domain, which, for an unbound top of the domain, lowers the overall pressure gradient across the domain, and therefore reduces the amplitude of the oscillation of the recirculation zone.

Although the overall characteristics of the oscillation do not differ much between free surface or fixed wall, one should not conclude that the free surface can be omitted in numerical simulations. Especially when the Reynolds number is increased, severe bubble entrainment will start to occur above the recirculation zone center and free surface oscillation magnitudes will increase.

## Bibliography

- [1] Berberović, E., van Hinsberg, N. P., Jakirlić, S., Roisman, I. V., and Tropea, C. Drop impact onto a liquid layer of finite thickness: Dynamics of the cavity evolution. *Physical Review E*, volume 79(3):p. 036306 (2009).
- [2] Brackbill, J. U., Kothe, D. B., and Zemach, C. A continuum method for modeling surface tension. *Journal of Computational Physics*, volume 100(2):pp. 335–354 (1992).
- [3] Chaudhary, R., Ji, C., Thomas, B. G., and Vanka, S. P. Transient Turbulent Flow in a Liquid-Metal Model of Continuous Casting, Including Comparison of Six Different Methods. *Metallurgical and Materials Transactions B* (2011).
- [4] Cukierski, K. and Thomas, B. G. Flow Control with Local Electromagnetic Braking in Continuous Casting of Steel Slabs. *Metallurgical and Materials Transactions B*, volume 39(1):pp. 94–107 (2007).
- [5] Garcia-Hernandez, S., Morales, R., and Torres-Alonso, E. Effects of EMBr position, mould curvature and

- slide gate on fluid flow of steel in slab mould. *Ironmaking and Steelmaking*, volume 37(5):pp. 360–368 (2010).
- [6] Graftieaux, L., Michard, M., and Grosjean, N. Combining PIV, POD and vortex identification algorithms for the study of unsteady turbulent swirling flows. *Measurement Science and Technology*, volume 12(9):p. 1422 (2001).
- [7] Hirt, C. and Nichols, B. Volume of fluid (VOF) method for the dynamics of free boundaries. *Journal of Computational Physics*, volume 39(1):pp. 201–225 (1981).
- [8] Hoang, D. A., van Steijn, V., Portela, L. M., Kreutzer, M. T., and Kleijn, C. R. Benchmark numerical simulations of segmented two-phase flows in microchannels using the Volume of Fluid method. *Computers & Fluids*, volume 86:pp. 28–36 (2013).
- [9] Honeyands, T. and Herbertson, J. Flow dynamics in thin slab caster moulds. *Steel Research International*, volume 66(7):pp. 287–293 (1995).
- [10] Kalter, R., Tummers, M., Kenjereš, S., Righolt, B., and Kleijn, C. Oscillations of the fluid flow and the free surface in a cavity with a submerged bifurcated nozzle. *International Journal of Heat and Fluid Flow* (2013).
- [11] Kang, K., Ryou, H., and Hur, N. Coupled Turbulent Flow, Heat, and Solute Transport in Continuous Casting Processes with an Electromagnetic Brake. *Numerical Heat Transfer, Part A: Applications: An International Journal of Computation and Methodology*, volume 48(5):p. 461 (2005).
- [12] Lilly, D. K. A proposed modification of the Germano subgrid-scale closure method. *Physics of Fluids A: Fluid Dynamics*, volume 4(3):p. 633 (1992).
- [13] Maurel, A., Ern, P., Zielinska, B. J. A., and Wesfreid, J. E. Experimental study of self-sustained oscillations in a confined jet. *Physical Review E*, volume 54(4):pp. 3643–3651 (1996).
- [14] Molloy, N. A. and Taylor, P. L. Oscillatory Flow of a Jet into a Blind Cavity. *Nature*, volume 224(5225):pp. 1192–1194 (1969).
- [15] Righolt, B. W., Kenjereš, S., Kalter, R., Tummers, M. J., and Kleijn, C. R. Dynamics of an oscillating turbulent jet in a confined cavity. *Physics of Fluids*, volume 27:p. 095107 (2015).
- [16] Rusche, H. *Computational Fluid Dynamics of Dispersed Two-Phase Flows at High Phase Fractions*. PhD thesis, Imperial College (2002).
- [17] Torres-Alonso, E., Morales, R., and García-Hernández, S. Cyclic turbulent instabilities in a thin slab mold. Part II: Mathematical model. *Metallurgical and Materials Transactions B: Process Metallurgy and Materials Processing Science*, volume 41(3):pp. 675–690 (2010).
- [18] Torres-Alonso, E., Morales, R. D., Demedices, L. G., Nájera, A., Palafox-Ramos, J., and Ramirez-Lopez, P. Flow dynamics in thin slab molds driven by sustainable oscillating jets from the feeding SEN. *ISIJ International*, volume 47(5):pp. 679–688 (2007).
- [19] Wang, Y. and Zhang, L. Fluid Flow-Related Transport Phenomena in Steel Slab Continuous Casting Strands under Electromagnetic Brake. *Metallurgical and Materials Transactions B* (2011).
- [20] Weller, H. G. A New Approach to VOF-based Interface Capturing Methods for Incompressible and Compressible Flow. Technical report, OpenCFD (2008).
- [21] Yu, H. and Zhu, M. Numerical simulation of the effects of electromagnetic brake and argon gas injection on the three-dimensional multiphase flow and heat transfer in slab continuous casting mold. *ISIJ International*, volume 48(5):pp. 584–591 (2008).
- [22] Zang, Y., Street, R. L., and Koseff, J. R. A dynamic mixed subgrid-scale model and its application to turbulent recirculating flows. *Physics of Fluids A: Fluid Dynamics*, volume 5(12):pp. 3186–3196 (1993).
- [23] Zhang, H., Shen, H., and Liu, B. Computational modeling of macroscopic transportation in continuous castings. *Materials Science Forum*, volume 508:pp. 543–548 (2006).





# 7. Conclusions and outlook

In this chapter, we discuss the answers to the research questions formulated in chapter 1 and we discuss our main findings in a broader perspective, suggesting further research opportunities.

## 7.1 General conclusions

### 7.1.1 Benchmark MHD free surface flow problem

In chapter 3 we have introduced a benchmark problem, which describes the free surface elevation of a shallow layer of conductive fluid. For low height-to-width aspect ratios, we have analytically derived the shape of the free surface under the influence of electromagnetic, gravitational and surface tension forces. The analytical solution is given in terms of the Reynolds number, the Hartmann number, the Bond number, the capillary number and the cavity aspect ratio. By means of two different numerical free surface modelling techniques we have demonstrated the range of applicability of the analytical solution in terms of the relevant dimensionless parameters. This tractable benchmark problem can be considered as a valuable tool for validating numerical methods for modelling magnetohydrodynamic free surface flows.

### 7.1.2 Mechanism for self-sustained jet oscillations

Our numerical LES simulations described in chapters 4 and 6 have provided more detailed insight in the role of the pressure in the large scale self-sustained oscillations found in thin cavities for several jet configurations. For both single jet and bifurcated jet arrangements, recirculation zones will form next to the turbulent jet. We have shown that deviations in the jet angle can be attributed to the pressure deficit in the center of such a recirculation zone. This pressure deficit induces jet deflection and at the same time increases with increasing jet angle. This is a strong feedback loop, causing the jet to deflect to an extreme position



with maximum pressure deficit in the recirculation zone. In the extreme position of the jet, fluid escapes from the recirculation zone. The fluid escapes to the bottom of the domain for single jet configurations and in a cross flow in bifurcated jet configurations. This leads to a decreasing pressure deficit in the recirculation zone. As the driving force for the jet deflection vanishes, it returns to the central state. In the single jet configuration the jet will deflect towards the opposite side, whereas in the bifurcated jet configuration, the jet on the opposite side will deflect. The process repeats indefinitely.

### 7.1.3 Model description of self-sustained jet oscillations

In chapter 4 we have described the self-sustained oscillation of a single jet in a confined cavity by means of a Delay Differential Equation (DDE)-type model, which contains a term for each of the three consecutive stages of the jet oscillation: (i) pressure deficit driven growth of the oscillation, (ii) amplitude limitation by geometry and (iii) delayed destruction of the recirculation zone:

$$\frac{\partial \theta}{\partial t} = r\theta - \mu\theta^3 - k\theta(t - \tau). \quad (7.1)$$

We have shown that with a proper parametrization for the model parameters  $r$ ,  $\mu$ ,  $k$  and  $\tau$ , this model predicts the jet oscillation characteristics as a function of the Reynolds number and cavity width to nozzle diameter ratio ( $W/d$ ). The model also determines a critical Reynolds number for given  $W/d$ , below which self-sustained oscillations can not exist.

### 7.1.4 Electromagnetic forcing of single jet oscillations

We have demonstrated in chapter 5 that the zero-dimensional model for self-sustained single jet oscillations in a confined cavity (Equation 7.1) does also predict the oscillations in electromagnetically forced flow oscillations, when the effect of the force is incorporated in the model parameters. The effect of an electromagnetic body force on the self-sustained oscillations distinguishes three regimes: an oscillation enhancing regime, an oscillation suppressing regime and a regime where the body force is of minor influence. The regimes are separated by a critical Stuart number,  $N_{crit}$ , that describes the ratio of the electromagnetic force and the inertial terms. For the studied configuration,  $N_{crit} = 0.013$ . When the oscillations are enhanced, the body force causes an increase in pressure difference, and therefore also in the growth rate  $r$ . Furthermore, due to the higher velocities, the delay time  $\tau$  decreases.

## 7.2 Research opportunities

### 7.2.1 Zero-dimensional models

The DDE model that was shown to represent the physics behind self-sustained oscillations of a single jet in a confined cavity, both with and without electromagnetic forcing, offers many further research possibilities.

#### Single jet

The zero dimensional model derived in this thesis for single jet oscillations, can for a specific choice of the parameters  $r$ ,  $\mu$ ,  $k$  and  $\tau$  result in a constant non-zero solution (this can happen for example when  $k$  is small). For the single jet oscillation, this means that the jet deflects towards one side of the cavity, and then stays in this position. We have observed this in numerical simulations for some cavity thicknesses outside the range of cavity thicknesses studied in chapter 4. This suggests that except for the self-sustained oscillation regimes, there may be two stationary regimes, a symmetric and a non-symmetric one.

#### Alternative body forces

In the present work we have focussed on a specific configuration of the Lorentz force due to imposed magnetic fields and injected currents. We believe that the presented zero-dimensional model will generally be useful when an imposed body force (not necessarily electromagnetic) is in the same direction as the fluid jet. For these situations, namely, the motivation behind the growing term in the model equation remains valid. When the working fluid in the thin cavity is a liquid metal, an external magnetic field only, which leads to induced currents, will be sufficient to suppress jet oscillations. As the electromagnetic force in such a situation would also mainly be in the direction of the main jet, the model is expected to remain useful.

### 7.2.2 Damping of oscillations

In this thesis we have outlined a method for benchmarking any free surface MHD flow solver. The analytically solved benchmark problem can be extended with, for example, temperature<sup>1</sup> or a Marangoni force.<sup>7</sup> For larger deformations, it may be possible to obtain at least a partial solution for the free surface deformation.<sup>6</sup>

In the benchmark problem, we have looked at steady state solutions of the deformed free surface state of a shallow layer of conductive liquid. In the two-dimensional numerical simulations, we have observed interesting phenomena during the transient phase towards the steady state solution. For some conditions, the free surface monotonously moves to this state, while

under other conditions the steady state is reached in a damped oscillating manner. The distinction between various damping modes can most likely be attributed to the balance between viscous and magnetic forces, which is the Hartmann number. For the damping of jet oscillations, we have only distinguished between oscillating and non-oscillating flows, however, investigation of the transient phase towards the damping may give more insight in optimizing the damping configurations.

### 7.2.3 Towards improved continuous steel casting

In this section we describe how the main findings and methodologies discussed in this thesis can be applied for improving the continuous steel casting process.

#### Critical damping

Above, we observed that at a specific Hartmann number, critical damping of free surface oscillation in the shallow cavity may occur. This is a situation with injected electrical currents and an imposed magnetic field. This has a relevance in electromagnetic braking in liquids, as it suggests that critical damping of an oscillation can occur. In other words, there is an optimal magnetic field strength for damping of the oscillations. Increasing the magnetic field strength above this optimum may therefore be less effective as an electromagnetic brake.

This insight may also be applied to the damping of the jet oscillations in single and bifurcated jet geometries. In this thesis we did not distinguish between the several damped modes. It is worth to investigate if the observation of critical damping also exists in terms of the Stuart number (ratio of magnetic and inertial forces) for oscillating jets in thin cavities.

#### Zero-dimensional modelling

The zero-dimensional model describes the time evaluation of the single variable,  $\theta$ , representing the angle of a single jet in a thin cavity. Realistic steel casting applications, however, are multi-jet configurations. It is possible to devise a coupled system with two oscillators, representing both jets in a bifurcated jet configuration. Such a system may look like

$$\frac{\partial \theta_1}{\partial t} = r\theta_1 - \mu\theta_1^3 - k(\theta_1(t - \delta) - \theta_2(t - \delta)), \quad (7.2)$$

$$\frac{\partial \theta_2}{\partial t} = r\theta_2 - \mu\theta_2^3 - k(\theta_2(t - \delta) - \theta_1(t - \delta)). \quad (7.3)$$

Here,  $\theta_1$  and  $\theta_2$  can represent the angles of both jets with respect to an axis. The first and second term on the right side of the equation have a similar representation as for the single jet, i.e. pressure driven oscillation growth and amplitude limitation by the geometry. The final term represents the coupling of both jets with a delay time, which represents the pressure drop by the overflow between both sides of the mould. Among the possible solutions of this set

of model equations, one solution is the anti-symmetric oscillation of  $\theta_1$  and  $\theta_2$ . This is what we observed in the bifurcated jet geometries studied in this thesis. We may anticipate that a similar stability criterion as for the single jet model exists. For the steel casting application, however, lowering the fluid velocity or increasing the width of the mould are not the most viable options for the suppression of large scale self-sustained oscillations.

Besides introducing electromagnetic forces, there is an additional route that is worth to investigate with respect to suppressing of oscillations in a dual-jet model. These coupled oscillators are a well-studied phenomenon,<sup>3-5</sup> and popular in, for example, electrical systems. Interesting phenomena in these coupled oscillators are *amplitude death* (AD)<sup>4,5</sup> and *oscillation death* (OD).<sup>2</sup> For both AD and OD the oscillations cease, for AD to the same ground state (typically zero), and for OD to dissimilar states (typically non-zero). Delayed feedback may be one reason for AD, but in typical steel casting applications, this does not seem to occur. From these extensive studies on coupled oscillators, other routes that may lead to the ceasing of oscillations are worth to investigate. One relevant opportunity is to investigate whether asymmetries in a continuous caster design may influence the (ceasing of the) oscillation in a beneficial way. Such a simplified model may provide substantial additional insight into the self-sustained oscillation of bifurcated jets.

### Three-dimensional simulations

In this thesis we have developed two numerical methods for three-dimensional free surface flows subject to electromagnetic forcing. These numerical models have been demonstrated only with imposed electrical currents, via the boundary conditions for the electric potential. The methods, however, can also be applied for pure one-way coupled magnetohydrodynamics, where only currents induced by the external magnetic field occur. These same numerical methods can therefore be used for investigations of electromagnetic braking configurations in continuous steel casting.

## Bibliography

- [1] Cormack, D. E., Leal, L. G., and Imberger, J. Natural Convection in a Shallow Cavity with Differentially Heated End Walls. Part 1. Asymptotic Theory. *Journal of Fluid Mechanics*, volume 65(02):pp. 209–229 (1974).
- [2] Koseska, A., Volkov, E., and Kurths, J. Transition from Amplitude to Oscillation Death via Turing Bifurcation. *Physical Review Letters*, volume 111(2):p. 024103 (2013).
- [3] Lakshmanan, M. and Senthilkumar, D. V. *Dynamics of Nonlinear Time-Delay Systems*. Springer, Berlin, Heidelberg (2010).
- [4] Ramana Reddy, D. V., Sen, A., and Johnston, G. L. Time Delay Induced Death in Coupled Limit Cycle Oscillators. *Physical Review Letters*, volume 80(23):pp. 5109–5112 (1998).
- [5] Ramana Reddy, D. V., Sen, A., and Johnston, G. L. Experimental Evidence of Time-Delay-Induced Death in Coupled Limit-Cycle Oscillators. *Physical Review Letters*, volume 85(16):pp. 3381–3384 (2000).

- 
- [6] Sen, A. K. Thermocapillary convection in a rectangular cavity with a deformable interface. *Physics of Fluids*, volume 29(11):pp. 3881–3883 (1986).
  - [7] Sen, A. K. and Davis, S. H. Steady thermocapillary flows in two-dimensional slots. *Journal of Fluid Mechanics*, volume 121:p. 163 (1982).





# List of Publications

- [1] Righolt, B. W., Kenjereš, S., Kalter, R., Tummers, M. J., and Kleijn, C. R. Analytical solutions of one-way coupled magnetohydrodynamic free surface flow. *Applied Mathematical Modelling*, 40:2577–2592, 2015.
- [2] Righolt, B. W., Kenjereš, S., Kalter, R., Tummers, M. J., and Kleijn, C. R. Dynamics of an oscillating turbulent jet in a confined cavity. *Physics of Fluids*, 27:095107, 2015. doi: 10.1063/1.4930926.
- [3] Righolt, B. W., Kenjereš, S., Kalter, R., Tummers, M. J., and Kleijn, C. R. Electromagnetic control of an oscillating turbulent jet in a confined cavity. *submitted*, 2016.
- [4] Righolt, B. W., Kenjereš, S., Kalter, R., Tummers, M. J., and Kleijn, C. R. Numerical study of turbulent submerged bifurcated jets impingement and interactions with a free surface. In: *8th International Symposium on Turbulence and Shear Flow Phenomena*, TSFP Proceedings. 2013.
- [5] Kalter, R., Tummers, M. J., Kenjereš, S., Righolt, B. W., and Kleijn, C. R. Oscillations of the fluid flow and the free surface in a cavity with a submerged bifurcated nozzle. *International Journal of Heat and Fluid Flow*, 2013. ISSN 0142-727X. doi: 10.1016/j.ijheatfluidflow.2013.07.007.
- [6] Kalter, R., Tummers, M. J., Kenjereš, S., Righolt, B. W., and Kleijn, C. R. Electromagnetic flow control of a bifurcated jet in a rectangular cavity. *International Journal of Heat and Fluid Flow*, 47, 2014. ISSN 0142-727X. doi: 10.1016/j.ijheatfluidflow.2014.03.006.
- [7] Kalter, R., Tummers, M. J., Kenjereš, S., Righolt, B. W., and Kleijn, C. R. Effects of electromagnetic forcing on self-sustained jet oscillations. *Physics of Fluids*, 26(6):065101, 2014. ISSN 1070-6631, 1089-7666. doi: 10.1063/1.4880897.
- [8] Kalter, R., Tummers, M. J., Wefers Bettink, J. B., Righolt, B. W., Kenjereš, S., and Kleijn, C. R. Aspect Ratio Effects on Fluid Flow Fluctuations in Rectangular Cavities. *Metall and Materi Trans B*, pages 1–8, 2014. ISSN 1073-5615, 1543-1916. doi: 10.1007/s11663-014-0119-7.
- [9] Kidess, A., Kenjereš, S., Righolt, B., and Kleijn, C. Marangoni driven turbulence in high energy surface melting processes. *International Journal of Thermal Sciences*, 104:412–422, 2016.
- [10] Kenjereš, S. and Righolt, B. Simulations of magnetic capturing of drug carriers in the brain vascular system. *International Journal of Heat and Fluid Flow*, 2012. ISSN 0142-727X. doi: 10.1016/j.ijheatfluidflow.2012.03.008.
- [11] Kenjereš, S., Righolt, B. W., Mulder, A. d., and Janssen, J. Simulations of Magnetic Drug Capturing in the Patient Specific Brain Vascular System under Pulsating Flow Conditions. In: Long, M., editor, *World Congress on Medical Physics and Biomedical Engineering May 26-31, 2012, Beijing, China*, number 39 in IFMBE Proceedings, pages 2154–2157. Springer Berlin Heidelberg, 2013. ISBN 978-3-642-29304-7, 978-3-642-29305-4.



- [12] Kenjereš, S. and Righolt, B. W. Simulation of Magnetic Capturing Efficiency of Drug Carriers in the Brain Vascular System. In: *7th International Symposium on Turbulence and Shear Flow Phenomena*, volume 2. 2011.
- [13] Kenjereš, S., Righolt, B., de Mulder, A., and Janssen, J. Simulations of Magnetic Drug Capturing in the Patient Specific Brain Vascular System under Pulsating Flow Conditions. In: *World Congress on Medical Physics and Biomedical Engineering May 26-31, 2012, Beijing, China*, pages 2154–2157. Springer Berlin Heidelberg, 2013.

# Acknowledgements

The completion of this thesis has occupied me for a significant part in the last few years. This journey will be a chapter of my life that I will never forget. Many people have accompanied me on this journey, which made travelling lot easier. I would like to thank everybody who contributed to this thesis in some way.

First, I want to thank my promoter and supervisor. Chris, you have put great trust in me, by asking me for this position in an early stage of my masters thesis. Your valuable insights, remarks and input that lead to this thesis are highly appreciated. You gave me the opportunity to pursue some interesting ideas, which lead to a thesis that looks completely different from what I expected in the start. Your valuable lessons will help me in the next chapters of my life.

Saša, your enthusiasm as co-promotor and my daily supervisor is contagious. You encouraged me when I needed it the most and your constructive comments gave me some very useful pushes ahead. I profited a lot from your knowledge on multiple numerical techniques.

Rudi, as a colleague on the same project, you never refused to perform additional measurements when I thought I needed them. Our many hours of discussing the fundamentals of steel casting taught me to properly separate numerics from physics. Also, I enjoyed our joint trips to Sweden and Germany a lot. Mark, after being the supervisor of my bachelor thesis, you also took part in this project as supervisor for Rudi. Your critical contributions to our regular progress meetings helped me on many occasions.

Supervising students is part of the job of a PhD candidate. I enjoyed this part of the work, and want to thank both students for their contribution. Ivar, your work gave much more insight in the MMIT method. Jasper, you started with the numerically study on single jets oscillations. From both of your contributions I later profited in my further research.

During the intensive period of a PhD project, colleagues become good friends. They contribute both scientifically and socially. Anton, at the very beginning of my journey to becoming an OpenFOAM expert, until the end, you were always happy to answer my OpenFOAM or programming related questions. I am also thankful that we shared the experience in struggling through the finalization of our theses. Michiel, I will never forget our endless discussions in

front of the whiteboard, from which we mutually benefited in advancing our modelling skills. Laurens, you can be annoying at times, but I enjoyed to have you as a roommate. Dries, Koen, we already met during the first year of our studies in 2005. Thank you for all the fun moments in the past few years. I would also like to thank my other roommates: Davide, Farzad, Miloš, Vincent, Patrick, Hrushikesh, Duong, Wenjie, Cees and Ozgur, thanks for many fruitful discussions and enjoyable moments.

I would like to thank the support staff at our university and elsewhere, as their work is essential for performing research. First of all the support from our secretaries: Anita and Fiona, and earlier Amanda and Angela. I would also like to thank the support staff of the university and at SurfSARA for their solutions to all my technical questions. Furthermore, I would like to thank the people in the OpenFOAM community, as their sharing of knowledge and contributions helped me in many ways

Furthermore many thanks to all colleagues and students for making my time at the Multi-Scale Physics department, and later Transport Phenomena, such a good time. Naming them all would lead to a long list, where I inevitably will forget some of you. If you read this, you belong to this list. I would, however, like to address some of you: Annekatrien, I appreciate the results of your baking skills over the years, and I am glad I could resist the peer pressure of you (and Dries) to bake something myself. Anand, you only joined the department right before I left, but I enjoyed our visits to De Kuip and Augsburg.

I want to thank my friends outside of the university for their patience with my stories about the project, which they may or may not have appreciated. The moments we spend together helped me to clear my mind from the research and regain some energy.

Finally, I would like to thank my family. Christiaan, as my older brother, who recently obtained his PhD, your independent advise is highly appreciated, and I have good memories on our shared rides when you still spent time in the Netherlands. My parents, your unconditional love and support for my choices, during this chapter, all earlier chapters, and many more to come, is very valuable to me.

# Curriculum Vitae

Bernhard Righolt was born on May 31st 1987 in Leidschendam. He went to CSG Johannes Calvijn in 1999, to obtain is Gymnasium diploma in 2005. He then went to Delft, to obtain his BSc degree in Applied Physics in 2008 and his MSc degree in Applied Physics in 2010. In the same year he started working as a PhD student in the Department of Multi-Scale Physics, later Chemical Engineering. In 2014 he started working as a technological consultant with ALTEN Technology.